Chapter I.8

Off-shell Higgs Production and Higgs Interference

F. Caola, Y. Gao, N. Kauer, L. Soffi, J. Wang (Eds.); A. Ballestrero, C. Becot, F. Bernlochner, H. Brun, A. Calandri, F. Campanario, F. Cerutti, D. de Florian, R. Di Nardo, L. Fayard, N. Fidanza, N. Greiner, A. V. Gritsan, G. Heinrich, B. Hespel, S. Höche, F. Krauss, Y. Li, S. Liebler, E. Maina, B. Mansoulié, C. O'Brien, S. Pozzorini, M. Rauch, J. Roskes, U. Sarica, M. Schulze, F. Siegert, P. Vanlaer, E. Vryonidou, G. Weiglein, M. Xiao, S. Yuen

I.8.1 Introduction

The Higgs boson measurements in the resonant region (on-peak) are broadly consistent with Standard Model expectations. The observed Higgs boson cross-sections are primarily measured via decays into two electroweak bosons (WW, ZZ and $\gamma\gamma$). However, the measured on-peak cross-sections are affected by an intrinsic scaling ambiguity between the Higgs couplings and the total Higgs width: $\sigma_{i\to H\to f} \sim g_i^2 g_f^2/\Gamma_H$. Disentangling this ambiguity would make it possible to constrain or even measure the total Higgs boson width at the LHC, which would be highly desirable. The total width of the SM Higgs boson is about 4 MeV, and hence much smaller than the experimental resolution of the Higgs boson mass measurements in the two high-resolution channels $H \to 4\ell$ and $H \to \gamma\gamma$, which is of the order of 1 GeV. For this reason, a direct measurement of the Higgs boson width is not feasible at the LHC.

A novel method has recently been proposed to constrain the Higgs boson width using events away from the on-peak region in the decays into ZZ and WW [495–497]. The off-shell cross-section of $gg \to H^* \to VV$ contributes $\mathcal{O}(15\%)$ due to two threshold effects, near $2M_V$ from the Higgs decay and $2m_t$ from the $gg \to H$ production. The electroweak diboson continuum $gg \to VV$ plays an important role in this off-shell region, mainly due to the large destructive interference with the $gg \to H^* \to VV$ signal. At leading order, $gg \to VV$ proceeds through a box diagram, which makes higher order calculations difficult. In this off-shell region, where $M_{VV} \gg M_H$, the cross-section dependence on the total Higgs width is negligible, providing a unique opportunity to measure the absolute Higgs boson couplings. The off-shell Higgs boson couplings can then be correlated with the on-shell cross-sections to provide a novel indirect constraint on the total Higgs boson width. It has been pointed out [498, 499] that BSM physics that alters the relation between Higgs cross-sections in the on-peak and off-shell regions could invalidate the method as applied in [496, 497]. Using future LHC data to constrain New Physics affecting the off-shell Higgs couplings is therefore important [500, 501].

The method has been promptly adopted by the CMS and ATLAS collaborations. The analyses [502–504] present constraints on the off-shell Higgs boson event yields normalized to the Standard Model prediction (signal strength) in the $ZZ\to 4\ell$, $ZZ\to 2\ell 2\nu$ and $WW\to \ell\nu\ell\nu$ channels. In the ATLAS analysis [503], using the CLs method, the observed 95% confidence level (CL) upper limit on the off-shell signal strength is in the range 5.1–8.6, with an expected range of 6.7–11.0. This range is determined by varying the unknown [I.48] $gg\to ZZ$ and $gg\to WW$ background K-factor from higher-order QCD corrections between half and twice the value of the evaluated signal K-factor. Under the assumption that the Higgs boson couplings are independent of the energy scale of the Higgs production, a combination of the off-shell constraint with the on-shell Higgs peak measurement yields an observed (expected) 95% CL upper limit on the Higgs total width normalized to the one predicted by the Standard Model, i.e. $\Gamma_{\mathrm{H}}/\Gamma_{\mathrm{SM}}$, in the range of 4.5–7.5 (6.5–11.2) employing the same variation of the background K-factor. Assuming that the unknown gg$\to VV$ background K-factor is equal to the signal K-factor, this translates

[I.48] cf. Section I.8.4

into an observed (expected) 95% CL upper limit on the Higgs boson total width of 22.7 (33.0) MeV.

In the CMS analysis of the ZZ and WW channels combined [504], an observed (expected) upper limit on the off-shell Higgs boson event yield normalised to the Standard Model prediction of 2.4 (6.2) is obtained at the 95% CL for the gluon fusion process and of 19.3 (34.4) for the VBF process. The observed and expected constraints on the Higgs boson total width are 13 MeV and 26 MeV, respectively, at the 95% CL. Concerning the $gg \to VV$ background K-factor, the central values and uncertainties are assumed to be equal to those of the signal K-factor, with an additional 10% uncertainty.

In addition to the off-shell $H^* \to VV$ channels, the $H \to \gamma\gamma$ channel also provides a very clean signature for probing Higgs properties, including its mass. However, there is also a large continuum background $gg \to \gamma\gamma$ to its detection in this channel. It is important to study how much the coherent interference between the Higgs signal and the background could affect distributions in diphoton observables, and possibly use it to constrain Higgs properties. An interesting study [505, 506] showed that this interference can lead to a shift in the Higgs boson mass, which has a strong dependence on the p_T of the diphoton system and the total Higgs boson width. This provides another way to constrain the Higgs boson width.

I.8.2 Overview

This chapter contains selected studies and benchmark results for off-shell Higgs production and Higgs interference. In Section I.8.3, theoretical and experimental studies of the SM Higgs signal in the off-shell/high-mass region for the gluon-fusion and VBF $\mathrm{H} \to \mathrm{VV}$ channels ($\mathrm{V} = \mathrm{W}, \mathrm{Z}$) including the interference with the background are presented. More specifically, Section I.8.3.1 details the used input parameters and gives our recommendations for the QCD scale and the order of the gluon PDF and illustrates the corresponding cross section dependence. Benchmark cross sections and distributions are collected in Section I.8.3.2 for the Standard Model, including recommended experimental selections for use in $\mathrm{gg} \to \mathrm{VV}$ calculations, and for the Higgs Singlet Model in Section I.8.3.3. Multi-jet merging and parton shower effects are discussed in Sections I.8.3.4 and I.8.3.5. Interference effects for heavy Higgs bosons or Higgs-like resonances in SM extensions are illustrated in Sections I.8.3.6 and I.8.3.7. In Section I.8.4, the status of NLO $\mathrm{gg} \to \mathrm{VV}$ calculations is reviewed, and $\mathrm{gg} \to 4\ell$ benchmark results and our recommendation for the treatment of the $\mathrm{gg}(\to \mathrm{H}) \to \mathrm{ZZ}$ interference K-factor are given. In Section I.8.5, the interference in the $\mathrm{H} \to \gamma\gamma$ channel is discussed. A theory overview is given and Monte Carlo interference implementations and related experimental studies are described.

I.8.3 $H \to VV$ modes ($V = W, Z$)

I.8.3.1 Input parameters and recommendations for the QCD scale and the order of the gluon PDF

The SM input parameters for Higgs physics given in Ref. [140] are adopted with the G_μ scheme: $M_\mathrm{W} = 80.35797$ GeV, $M_\mathrm{Z} = 91.15348$ GeV, $\Gamma_\mathrm{W} = 2.08430$ GeV, $\Gamma_\mathrm{Z} = 2.49427$ GeV, $m_\mathrm{t} = 172.5$ GeV, $m_\mathrm{b}(m_\mathrm{b}) = 4.18$ GeV and $G_F = 1.1663787 \cdot 10^{-5}$ GeV^{-2}. The CKM matrix is approximated by the identity matrix. Finite top and bottom quark mass effects are included. Lepton and light quark masses are neglected. Results are given for pp collisions at $\sqrt{s} = 13$ TeV unless otherwise noted. The PDF set `PDF4LHC15_nlo_100` [29] is used by default. All PDF sets are used with the default α_s of the set. A fixed-width Breit-Wigner propagator $D(p) \sim (p^2 - M^2 + iM\Gamma)^{-1}$ is employed for W, Z and Higgs bosons, where M and Γ are determined by the complex pole of the amplitude due to unstable particle propagation.[I.49] The SM Higgs mass is set to 125 GeV. The SM Higgs width parameter is calculated using HDECAY v6.50 [65]. For $M_\mathrm{H} = 125$ GeV one obtains $\Gamma_\mathrm{H} = 4.097 \cdot 10^{-3}$ GeV.

[I.49] In agreement with HDECAY, the W and Z masses and widths have been changed from physical on-shell masses to the pole values, see Eq. (7) in Ref. [140]. The relative deviation is at the $3 \cdot 10^{-4}$ level.

For off-shell and high-mass $\mathrm{H} \to \mathrm{VV}$ cross-section and interference calculations, we recommend and employ the QCD scale $\mu_R = \mu_F = M_{\mathrm{VV}}/2$ unless otherwise noted. Next, we elucidate the choice of the PDF order for the $\mathrm{gg} \to \mathrm{VV}$ continuum background and the corresponding Higgs-continuum interference. Combining any n-order PDF fit with a m-order parton-level calculation is theoretically consistent as long as $n \geq m$. Deviations are expected to be of higher order if the same $\alpha_\mathrm{s}(M_\mathrm{Z})$ is used. But, using a LO gluon PDF with $\alpha_\mathrm{s}(M_\mathrm{Z})$ obtained in the LO fit is not recommended: The gluon PDF is mostly determined by DIS data, especially in the SM Higgs region. At LO, DIS does not have a gluon channel. It only enters at NLO, with a large K-factor. A LO fit cannot properly account for this $\mathcal{O}(50\%)$ contribution, but incorrectly adjusts the gluon evolution to compensate, which results in an overestimated value of $\alpha_\mathrm{s}(M_\mathrm{Z})$ of approximately 0.13. We therefore recommend using a NLO PDF set when computing the $\mathrm{gg}\ (\to \mathrm{H}) \to \mathrm{VV}$ interference and the gg continuum background at LO as well as NLO. For consistency, we also use the NLO PDF set for the corresponding signal process.[I.50]

The variation induced by different PDF and QCD scale choices is illustrated in Tables 77, 78, 79 and 80 using the process $\mathrm{gg}\ (\to \mathrm{H}) \to \ell\bar{\ell}\ell'\bar{\ell}'$. The Higgs signal ($S$), gg background ($B$) and the signal-background interference (I) are displayed at LO for four Higgs invariant mass regions:

- *off-shell* (OFS): $M_{\mathrm{VV}} > 140$ GeV
- *off-shell high-mass (interference)* (HM1): $220 < M_{\mathrm{VV}} < 300$ GeV
- *off-shell high-mass (signal enriched)* (HM2): $M_{\mathrm{VV}} > 300$ GeV
- *resonance* (RES): $110 < M_{\mathrm{VV}} < 140$ GeV

Motivated by the Higgs width constraints of Refs. [502, 503], the off-shell high-mass region is divided into the interference-sensitive (HM1) and signal-enriched (HM2) regions. Two sets of selection cuts are considered:

- *minimal cuts* (MIN): $M_{\ell\bar{\ell}} > 10$ GeV, $M_{\ell'\bar{\ell}'} > 10$ GeV
- *CMS* $\mathrm{H} \to 4\ell$ *cuts* (CMS): $p_{\mathrm{T}1} > 20$ GeV, $p_{\mathrm{T}2} > 10$ GeV, $p_{\mathrm{T}3,4} > 5$ GeV, $|\eta_\mathrm{e}| < 2.5$, $|\eta_\mu| < 2.4$, $M_{\mathrm{e\bar{e}}} > 4$ GeV, $M_{\mu\bar{\mu}} > 4$ GeV

The PDF4LHC15 [29] NLO and NNLO sets ($\alpha_\mathrm{s}(M_\mathrm{Z}) = 0.118$) and the CT14 [30] LO sets with $\alpha_\mathrm{s}(M_\mathrm{Z}) = 0.130$ and $\alpha_\mathrm{s}(M_\mathrm{Z}) = 0.118$ (and 1- and 2-loop evolution, respectively) are compared in Tables 77 and 78. As expected, the deviations for PDF sets with $\alpha_\mathrm{s}(M_\mathrm{Z}) = 0.118$ are of order 10% or less while the LO set with $\alpha_\mathrm{s}(M_\mathrm{Z}) = 0.130$ yields results that differ by up to 30%. The deviation between the NLO and NNLO sets is at the percent level. Furthermore, different choices for the QCD scale $\mu = \mu_R = \mu_F$ are compared in Tables 79 and 80. As central scale choices, the dynamic scale $\mu_0 = M_{2\ell2\ell}/2$ and the fixed scales $M_\mathrm{H}/2$ and M_Z are considered. The LO scale variation is estimated for μ_0 using the scales $\mu_0/2$ and $2\mu_0$. The results illustrate that using a fixed scale appropriate for resonant signal or background will significantly overestimate the signal, background and interference cross sections in the far off-shell and high-mass regions. With the recommended central scale $M_{2\ell2\ell}/2$, a factor-two scale variation yields a LO scale uncertainty of $20\%-25\%$ for the off-shell signal and signal plus background interference. The results of these comparisons were calculated using GG2VV [495].

I.8.3.2 Off-shell and interference benchmark cross sections and distributions: Standard Model

Gluon-fusion SM benchmark results were computed with GG2VV [495] (see also Refs. [507–510]) and MADGRAPH5_AMC@NLO (MG5_AMC) [48,511] (see also Ref. [510]). The GG2VV and MG5_AMC results were found to be in good agreement. Benchmark cross sections for $\mathrm{gg}\ (\to \mathrm{H}) \to \mathrm{VV} \to 4$ leptons processes in pp collisions at $\sqrt{s} = 13$ TeV in the SM are given in Table 81. Results for the Higgs signal, the signal including signal-background interference as well as the interfering background without Higgs contribution are displayed for minimal cuts $M_{\ell\bar{\ell}} > 10$ GeV, $M_{\ell'\bar{\ell}'} > 10$ GeV. The cross sections are calculated at loop-induced leading order. The recommended next-to-leading order K-factor is discussed in Section I.8.4. Similarly, in Table 82 benchmark cross sections for $\mathrm{gg}\ (\to \mathrm{H}) \to \mathrm{VV} \to$

[I.50] We note that the LO and NLO VBF results have also been obtained with the NLO PDF set.

Table 77: PDF dependence of off-shell $\mathrm{gg}\ (\to \mathrm{H}) \to \ell\bar{\ell}\ell'\bar{\ell}'$ cross sections at LO in fb for one lepton flavour combination. MIN cuts are applied. R is the ratio of NNLO, LO result to NLO result. The bottom rows show the ratio of OFS, HM1, HM2 to RES result for S and $S+I$. The recommended QCD scale $\mu_R = \mu_F = M_{2\ell 2\ell}/2$ is used. The MC error is given in brackets. See main text for other details.

		PDF set order						
Reg.	Amp.	**NLO**	NNLO	R	LO(0.118)	R	LO(0.130)	R
OFS	S	0.1266(1)	0.1255(1)	0.991(2)	0.1255(1)	0.992(2)	0.1414(2)	1.116(2)
	$S+I$	−0.1313(2)	−0.1298(2)	0.988(2)	−0.1307(2)	0.995(2)	−0.149(1)	1.138(8)
	B	2.988(4)	2.945(5)	0.986(2)	2.960(4)	0.991(2)	3.448(5)	1.154(3)
HM1	S	0.01933(4)	0.01906(4)	0.986(3)	0.01899(4)	0.982(3)	0.02210(5)	1.143(4)
	$S+I$	−0.04550(8)	−0.04475(8)	0.984(3)	−0.04486(7)	0.986(3)	−0.0516(6)	1.13(2)
	B	1.182(3)	1.165(3)	0.985(3)	1.166(3)	0.986(3)	1.354(3)	1.145(4)
HM2	S	0.0981(1)	0.0974(1)	0.993(2)	0.0973(1)	0.992(2)	0.1084(2)	1.105(2)
	$S+I$	−0.0465(1)	−0.04622(9)	0.994(3)	−0.04637(9)	0.997(3)	−0.0522(6)	1.12(2)
	B	0.611(2)	0.605(2)	0.990(4)	0.598(2)	0.980(4)	0.676(2)	1.107(5)
RES	S	0.800(1)	0.780(1)	0.976(2)	0.843(1)	1.054(2)	1.021(2)	1.276(3)
	$S+I$	0.803(2)	0.784(2)	0.976(4)	0.845(4)	1.052(6)	1.023(3)	1.274(5)
	B	0.1092(2)	0.1063(2)	0.974(2)	0.1150(2)	1.053(3)	0.1389(2)	1.272(3)
OFS/	S	0.1583(3)	0.1609(3)		0.1490(3)		0.1385(3)	
RES	$S+I$	−0.1635(4)	−0.1655(5)		−0.1547(7)		−0.146(2)	
HM1/	S	0.02418(6)	0.02443(6)		0.02253(6)		0.02165(5)	
RES	$S+I$	−0.0566(2)	−0.0571(2)		−0.0531(3)		−0.0504(6)	
HM2/	S	0.1227(2)	0.1249(3)		0.1155(2)		0.1062(2)	
RES	$S+I$	−0.0579(2)	−0.0589(2)		−0.0549(3)		−0.0510(6)	

semileptonic final states in pp collisions at $\sqrt{s} = 13$ TeV in the SM are given. As above, the signal amplitude is calculated at loop-induced leading order. But, for the semileptonic decay modes, the $\mathcal{O}(g_s^2 e^2)$ tree-level as well as the important loop-induced $\mathcal{O}(g_s^2 e^4)$ amplitude contributions to the interfering background are taken into account [510]. The following minimal cuts are applied: $M_{\ell\bar{\ell}} > 10$ GeV, $M_{\mathrm{q\bar{q}}} > 10$ GeV, $p_{\mathrm{T}j} > 25$ GeV. Higgs invariant mass distributions corresponding to the cross sections given in Tables 81 and 82 are displayed in Figures 127, 128 and 129.

The following experimental Higgs off-shell search selections are recommended for use in $\mathrm{gg} \to \mathrm{VV}$ calculations:
Jets: ATLAS: $p_{\mathrm{T}j} > 25$ GeV for $|\eta_j| < 2.4$, $p_{\mathrm{T}j} > 30$ GeV for $2.4 < |\eta_j| < 4.5$
Jets: CMS: $p_{\mathrm{T}j} > 30$ GeV for $|\eta_j| < 4.7$
$\mathrm{H} \to \mathrm{ZZ} \to 4\ell$ channel: ATLAS:
$p_{\mathrm{T}\ell,1} > 20$ GeV, $p_{\mathrm{T}\ell,2} > 15$ GeV, $p_{\mathrm{T}\ell,3} > 10$ GeV, $p_{\mathrm{Te},4} > 7$ GeV, $p_{\mathrm{T\mu},4} > 6$ GeV, $|\eta_{\mathrm{e}}| < 2.47$, $|\eta_{\mu}| < 2.7$, $M_{4\ell} > 220$ GeV
$\mathrm{H} \to \mathrm{ZZ} \to 4\ell$ channel: CMS:
$p_{\mathrm{T}\ell,1} > 20$ GeV, $p_{\mathrm{T}\ell,2} > 10$ GeV, $p_{\mathrm{Te},3,4} > 7$ GeV, $p_{\mathrm{T\mu},3,4} > 5$ GeV, $|\eta_{\mathrm{e}}| < 2.5$, $|\eta_{\mu}| < 2.4$, $M_{4\ell} > 220$ GeV
$\mathrm{H} \to \mathrm{ZZ} \to 2\ell 2\nu$ channel: ATLAS:
$p_{\mathrm{T}\ell} > 20$ GeV (electron, muon), $|\eta_{\mathrm{e}}| < 2.47$, $|\eta_{\mu}| < 2.5$, $E_{T,miss} > 180$ GeV, $\Delta\phi_{\ell\ell} < 1.4$, $M_{\mathrm{T,ZZ}} > 380$ GeV

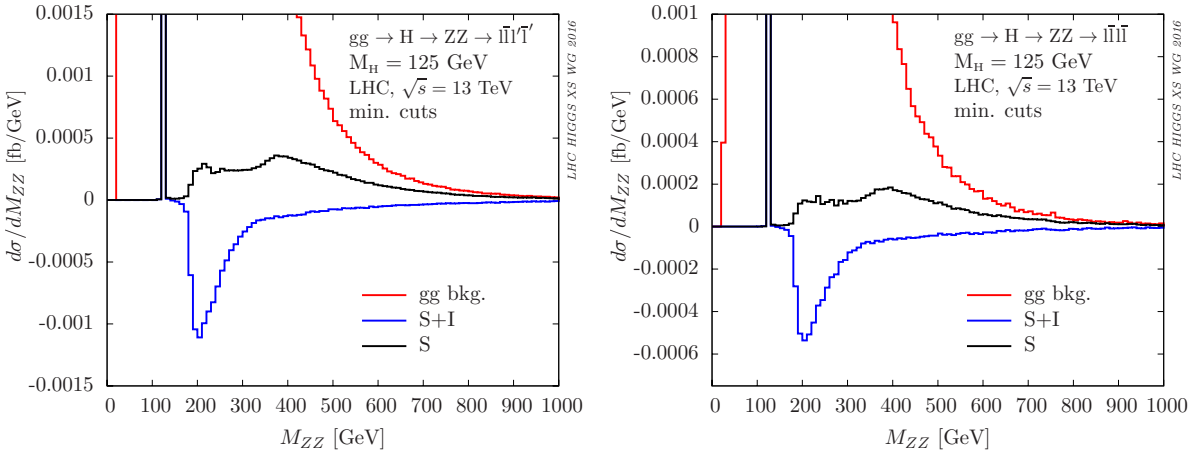

Figure 127: Invariant mass distributions for gg ($\to$ H) $\to$ ZZ $\to \ell\bar{\ell}\ell'\bar{\ell}'$ and gg ($\to$ H) $\to$ ZZ $\to \ell\bar{\ell}\ell\bar{\ell}$. Other details as in Table 81.

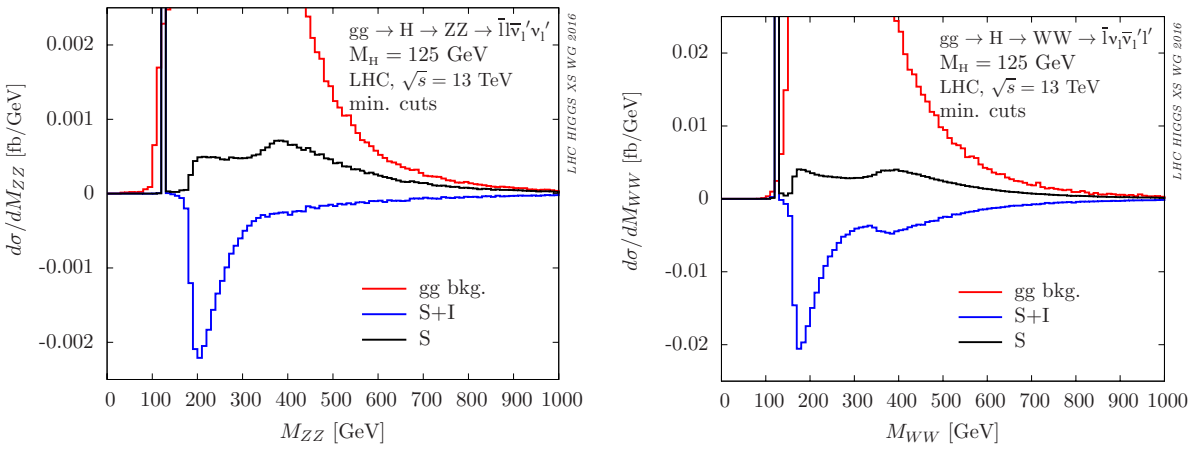

Figure 128: Invariant mass distributions for gg ($\to$ H) $\to$ ZZ $\to \ell\bar{\ell}\nu_{\ell'}\bar{\nu}_{\ell'}$ and gg ($\to$ H) $\to$ WW $\to \bar{\ell}\nu_l\bar{\nu}_{\ell'}\ell'$. Other details as in Table 81.

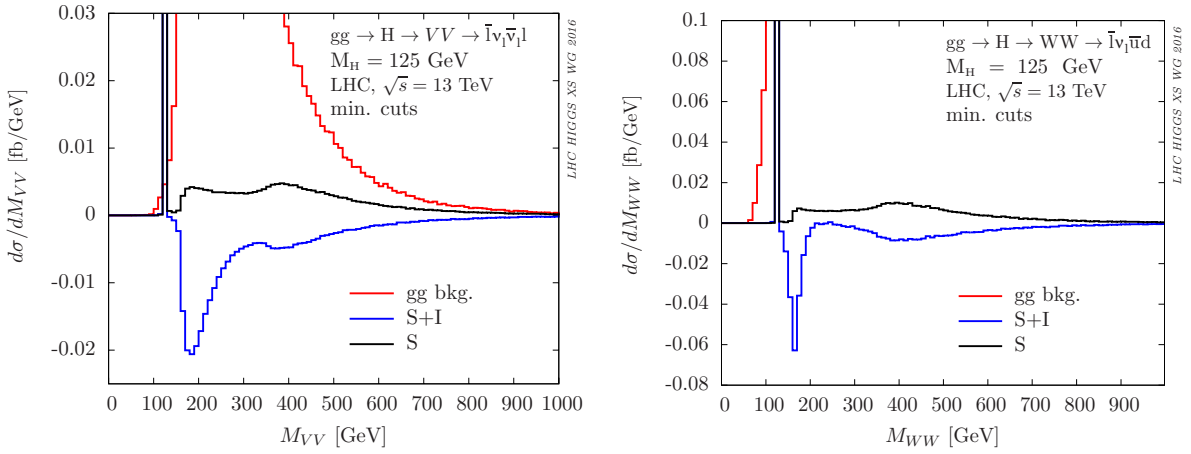

Figure 129: Invariant mass distributions for gg ($\to$ H) $\to$ WW/ZZ $\to \bar{\ell}\nu_l\bar{\nu}_l\ell$ and gg ($\to$ H) $\to$ WW $\to \bar{\ell}\nu_l\bar{u}d$. Other details as in Tables 81 and 82.

Table 78: PDF dependence of off-shell gg ($\to$ H) $\to$ $e^-e^+\mu^-\mu^+$ cross sections at LO in fb. CMS cuts are applied. Other details as in Table 77.

		PDF set order						
Reg.	Amp.	**NLO**	NNLO	R	LO(0.118)	R	LO(0.130)	R
OFS	S	0.0952(3)	0.09396(8)	0.986(3)	0.09034(7)	0.949(3)	0.10191(8)	1.070(3)
	$S+I$	−0.0893(3)	−0.0883(1)	0.989(3)	−0.08436(9)	0.944(3)	−0.0973(1)	1.089(4)
	B	1.869(3)	1.841(3)	0.985(2)	1.736(2)	0.928(2)	2.033(3)	1.088(2)
HM1	S	0.01303(9)	0.01278(3)	0.981(7)	0.01200(3)	0.921(7)	0.01402(3)	1.076(8)
	$S+I$	−0.0298(2)	−0.02942(6)	0.986(6)	−0.02759(5)	0.925(5)	−0.03227(6)	1.082(6)
	B	0.738(2)	0.727(2)	0.986(3)	0.679(2)	0.920(3)	0.795(2)	1.079(4)
HM2	S	0.0761(3)	0.07531(8)	0.990(4)	0.07271(7)	0.956(3)	0.08123(8)	1.067(4)
	$S+I$	−0.0349(2)	−0.03471(7)	0.994(6)	−0.03376(6)	0.967(6)	−0.03757(7)	1.076(7)
	B	0.382(2)	0.377(2)	0.987(5)	0.353(1)	0.925(5)	0.403(2)	1.055(5)
RES	S	0.4392(7)	0.4284(7)	0.975(3)	0.4343(7)	0.989(3)	0.5267(8)	1.199(3)
	$S+I$	0.439(2)	0.428(2)	0.975(4)	0.433(2)	0.988(4)	0.527(2)	1.200(5)
	B	0.06294(8)	0.06155(8)	0.978(2)	0.06243(9)	0.992(2)	0.0755(1)	1.200(3)
OFS/ RES	S	0.2169(7)	0.2193(4)		0.2080(4)		0.1935(4)	
	$S+I$	−0.2036(8)	−0.2065(6)		−0.1946(6)		−0.1847(6)	
HM1/ RES	S	0.0297(2)	0.02984(8)		0.02762(8)		0.02662(7)	
	$S+I$	−0.0680(4)	−0.0688(3)		−0.0637(3)		−0.0613(2)	
HM2/ RES	S	0.1733(6)	0.1758(4)		0.1674(4)		0.1542(3)	
	$S+I$	−0.0796(5)	−0.0811(3)		−0.0779(3)		−0.0714(3)	

ATLAS transverse mass definition (recommended for $M_{\rm VV} > 2M_{\rm Z}$):

$$M_{\rm T,ZZ} = \sqrt{\left(M_{{\rm T},\ell\ell} + M_{{\rm T},miss}\right)^2 - \left(\mathbf{p}_{T,\ell\ell} + \mathbf{p}_{T,miss}\right)^2}\,, \text{ where } \quad M_{{\rm T},X} = \sqrt{p^2_{{\rm T},X} + M^2_Z} \qquad \text{(I.8.1)}$$

H $\to$ ZZ $\to$ 2ℓ2ν channel: CMS:
$p_{{\rm T}\ell} > 20$ GeV (electron, muon), $E_{T,miss} > 80$ GeV
$M_{\rm T,ZZ}$ used by CMS: Eq. (I.8.1) with M_Z replaced by $M_{\ell\ell}$
H $\to$ WW $\to$ 2ℓ2ν channel: ATLAS:
$p_{{\rm T}\ell,1} > 22$ GeV, $p_{{\rm T}\ell,2} > 10$ GeV, $|\eta_{\rm e}| < 2.47$, $|\eta_\mu| < 2.5$, $M_{\ell\ell} > 10$ GeV, $p_{{\rm T},miss} > 20$ GeV, $M_{\rm T,WW} > 200$ GeV
ATLAS transverse mass definition (recommended):

$$M_{\rm T,WW} = \sqrt{\left(M_{{\rm T},\ell\ell} + p_{{\rm T},miss}\right)^2 - \left(\mathbf{p}_{T,\ell\ell} + \mathbf{p}_{T,miss}\right)^2}\,, \text{ where } \quad M_{{\rm T},\ell\ell} = \sqrt{p^2_{{\rm T},\ell\ell} + M^2_{\ell\ell}} \qquad \text{(I.8.2)}$$

Vector-boson-fusion SM benchmark results were computed with PHANTOM [512] (see also Ref. [513]) and VBFNLO [271, 514] (see also Refs. [515–519]). Good agreement was achieved for all fully-leptonic Higgs decay modes. For VBF, two selection cut sets are applied which have the following selection in common:

- $p_{{\rm T}j} > 20$ GeV, $|\eta_j| < 5.0$, $M_{jj} > 60$ GeV for all jets, anti-$k_{\rm T}$ jet clustering with $R = 0.4$
- $p_{{\rm T}\ell} > 20$ GeV, $|\eta_\ell| < 2.5$, $M_{\ell\bar{\ell}} > 20$ GeV (same flavour only), $E_{\rm T}^{\rm miss} > 40$ GeV
- tagging jets: j_1, j_2, ordered by decreasing $|\eta_j|$

Exception: for the *resonance* (RES) region (see Section I.8.3.1) $M_{\ell\bar{\ell}} > 10$ GeV is applied instead of $M_{\ell\bar{\ell}} > 20$ GeV. With this common selection, we define:

- *loose VBF cuts*: common selection and $M_{j_1j_2} > 130$ GeV
- *tight VBF cuts*: common selection and $M_{j_1j_2} > 600$ GeV, $\Delta y_{j_1j_2} > 3.6$, $y_{j_1} y_{j_2} < 0$ (opposite hemispheres)

Table 79: QCD scale $\mu = \mu_R = \mu_F$ dependence and symmetric scale uncertainty of off-shell $\mathrm{gg}\ (\to \mathrm{H}) \to \ell\bar{\ell}\ell'\bar{\ell}'$ cross sections at LO in fb for one lepton-flavour combination. MIN cuts are applied. R is the ratio of the result to the cross section with the recommended scale choice $\mu = M_{2\ell 2\ell}/2$. As recommended, the NLO PDF set is used. Other details as in Table 77.

		Dynamic scale			Fixed scales			
Reg.	Amp.	$\boldsymbol{M_{2\ell 2\ell}/2}$	$\Delta(M_{2\ell 2\ell})$ $\Delta(M_{2\ell 2\ell}/4)$ symmetr. Δ	R R R	$M_{\mathrm{H}}/2$	R	M_{Z}	R
OFS	S		$-0.0258(2)$	$-0.204(2)$				
	S	$0.1266(1)$	$0.0349(2)$	$0.276(2)$	$0.2038(2)$	$1.610(2)$	$0.1760(2)$	$1.390(2)$
	S		$\pm 0.0303(2)$	$\pm 0.240(1)$				
	$S+I$		$0.0251(2)$	$0.182(2)$				
	$S+I$	$-0.1313(2)$	$-0.0328(2)$	$-0.250(2)$	$-0.1831(2)$	$1.394(2)$	$-0.1604(2)$	$1.221(2)$
	$S+I$		$\pm 0.0290(2)$	$\pm 0.221(1)$				
	B		$-0.545(5)$	$-0.182(2)$				
	B	$2.988(4)$	$0.699(7)$	$0.234(3)$	$3.751(4)$	$1.255(3)$	$3.327(4)$	$1.114(2)$
	B		$\pm 0.6225(4)$	$\pm 0.209(2)$				
HM1	S		$-0.00355(4)$	$-0.184(3)$				
	S	$0.01928(3)$	$0.00455(6)$	$0.236(3)$	$0.02406(6)$	$1.248(4)$	$0.02150(5)$	$1.115(3)$
	S		$\pm 0.00405(4)$	$\pm 0.210(2)$				
	$S+I$		$0.0085(1)$	$0.187(3)$				
	$S+I$	$-0.04553(8)$	$-0.0106(2)$	$-0.233(3)$	$-0.0561(1)$	$1.233(3)$	$-0.05002(9)$	$1.099(3)$
	$S+I$		$\pm 0.0096(1)$	$\pm 0.2095(2)$				
	B		$-0.223(4)$	$-0.188(3)$				
	B	$1.186(3)$	$0.273(5)$	$0.230(4)$	$1.462(3)$	$1.232(4)$	$1.302(3)$	$1.098(4)$
	B		$\pm 0.248(2)$	$\pm 0.209(3)$				
HM2	S		$-0.0207(2)$	$-0.211(2)$				
	S	$0.0982(2)$	$0.0284(2)$	$0.289(2)$	$0.1693(2)$	$1.724(3)$	$0.1451(2)$	$1.478(3)$
	S		$\pm 0.0246(2)$	$\pm 0.250(2)$				
	$S+I$		$0.0099(2)$	$0.212(3)$				
	$S+I$	$-0.04651(8)$	$-0.0136(2)$	$-0.293(3)$	$-0.0818(2)$	$1.760(5)$	$-0.0700(2)$	$1.505(4)$
	$S+I$		$\pm 0.0118(1)$	$\pm 0.253(2)$				
	B		$-0.123(2)$	$-0.201(3)$				
	B	$0.610(1)$	$0.167(3)$	$0.275(5)$	$0.929(3)$	$1.524(5)$	$0.807(2)$	$1.323(4)$
	B		$\pm 0.145(2)$	$\pm 0.238(3)$				
RES	S		$-0.115(2)$	$-0.143(2)$				
	S	$0.800(1)$	$0.131(2)$	$0.164(2)$	$0.801(2)$	$1.001(2)$	$0.737(1)$	$0.921(2)$
	S		$\pm 0.123(2)$	$\pm 0.154(2)$				
	$S+I$		$-0.116(3)$	$-0.145(2)$				
	$S+I$	$0.803(2)$	$0.130(3)$	$0.162(3)$	$0.803(2)$	$1.000(3)$	$0.739(2)$	$0.920(3)$
	$S+I$		$\pm 0.123(2)$	$\pm 0.153(2)$				
	B		$-0.0158(3)$	$-0.145(3)$				
	B	$0.1092(2)$	$0.0176(3)$	$0.162(3)$	$0.1089(2)$	$0.998(2)$	$0.1002(2)$	$0.917(2)$
	B		$\pm 0.0167(2)$	$\pm 0.153(2)$				
OFS/ RES	S	$0.1583(3)$			$0.2545(5)$		$0.2389(4)$	
	$S+I$	$-0.1635(4)$			$-0.2279(5)$		$-0.2172(5)$	
HM1/ RES	S	$0.02411(5)$			$0.03005(8)$		$0.02918(8)$	
	$S+I$	$-0.0567(2)$			$-0.0699(2)$		$-0.0677(2)$	
HM2/ RES	S	$0.1228(3)$			$0.2114(4)$		$0.1970(4)$	
	$S+I$	$-0.0579(2)$			$-0.1019(3)$		$-0.0948(3)$	

Table 80: QCD scale $\mu = \mu_R = \mu_F$ dependence and symmetric scale uncertainty of off-shell $\mathrm{gg}\ (\to \mathrm{H}) \to \ell\bar{\ell}\ell'\bar{\ell}'$ cross sections at LO in fb for one lepton-flavour combination. CMS cuts are applied. Other details as in Table 79.

		Dynamic scale			Fixed scales			
Reg.	Amp.	$M_{2\ell 2\ell}/2$	$\Delta(M_{2\ell 2\ell})$ $\Delta(M_{2\ell 2\ell}/4)$ symmetr. Δ	R R R	$M_{\mathrm{H}}/2$	R	M_{Z}	R
	S		$-0.0196(3)$	$-0.206(4)$				
	S	$0.0952(3)$	$0.0257(4)$	$0.270(4)$	$0.1545(4)$	$1.622(6)$	$0.1338(4)$	$1.405(5)$
	S		$\pm 0.0227(3)$	$\pm 0.238(3)$				
	$S+I$		$0.0164(4)$	$0.184(4)$				
OFS	$S+I$	$-0.0893(3)$	$-0.0223(4)$	$-0.250(5)$	$-0.1282(4)$	$1.435(6)$	$-0.1119(3)$	$1.253(5)$
	$S+I$		$\pm 0.0194(3)$	$\pm 0.217(3)$				
	B		$-0.331(4)$	$-0.177(2)$				
	B	$1.869(3)$	$0.430(4)$	$0.230(2)$	$2.341(3)$	$1.252(3)$	$2.084(3)$	$1.115(2)$
	B		$\pm 0.381(3)$	$\pm 0.204(2)$				
	S		$-0.00235(3)$	$-0.181(2)$				
	S	$0.01302(2)$	$0.00303(3)$	$0.233(3)$	$0.0163(2)$	$1.25(1)$	$0.0145(1)$	$1.115(8)$
	S		$\pm 0.00269(2)$	$\pm 0.207(2)$				
	$S+I$		$0.00536(6)$	$0.179(2)$				
HM1	$S+I$	$-0.02986(5)$	$-0.00682(7)$	$-0.228(3)$	$-0.0370(2)$	$1.241(7)$	$-0.0326(2)$	$1.092(6)$
	$S+I$		$\pm 0.00609(5)$	$\pm 0.204(2)$				
	B		$-0.132(2)$	$-0.178(2)$				
	B	$0.739(1)$	$0.168(2)$	$0.227(3)$	$0.908(2)$	$1.229(3)$	$0.811(2)$	$1.097(3)$
	B		$\pm 0.150(1)$	$\pm 0.203(2)$				
	S		$-0.0160(2)$	$-0.210(2)$				
	S	$0.0761(1)$	$0.0218(2)$	$0.286(3)$	$0.1315(4)$	$1.727(6)$	$0.1131(4)$	$1.485(5)$
	S		$\pm 0.0189(1)$	$\pm 0.248(2)$				
	$S+I$		$0.00740(7)$	$0.211(2)$				
HM2	$S+I$	$-0.03505(6)$	$-0.01006(9)$	$-0.287(3)$	$-0.0630(3)$	$1.798(9)$	$-0.0537(3)$	$1.533(8)$
	$S+I$		$\pm 0.0088(1)$	$\pm 0.249(2)$				
	B		$-0.0768(8)$	$-0.201(2)$				
	B	$0.3822(6)$	$0.1019(9)$	$0.267(3)$	$0.582(2)$	$1.522(5)$	$0.506(2)$	$1.324(4)$
	B		$\pm 0.090(1)$	$\pm 0.234(2)$				
	S		$-0.0603(9)$	$-0.137(2)$				
	S	$0.4392(7)$	$0.066(1)$	$0.151(3)$	$0.4389(7)$	$0.999(3)$	$0.4044(6)$	$0.921(2)$
	S		$\pm 0.064(2)$	$\pm 0.145(2)$				
	$S+I$		$-0.060(2)$	$-0.136(4)$				
RES	$S+I$	$0.439(2)$	$0.067(2)$	$0.154(5)$	$0.438(2)$	$0.999(4)$	$0.406(2)$	$0.925(4)$
	$S+I$		$\pm 0.064(2)$	$\pm 0.145(3)$				
	B		$-0.0086(2)$	$-0.136(2)$				
	B	$0.06294(8)$	$0.0097(2)$	$0.155(2)$	$0.06302(9)$	$1.001(2)$	$0.05816(8)$	$0.924(2)$
	B		$\pm 0.0092(1)$	$\pm 0.146(2)$				
OFS/	S	$0.2169(7)$			$0.352(1)$		$0.331(1)$	
RES	$S+I$	$-0.2036(8)$			$-0.292(2)$		$-0.276(2)$	
HM1/	S	$0.02964(6)$			$0.0371(3)$		$0.0359(3)$	
RES	$S+I$	$-0.0681(3)$			$-0.0845(5)$		$-0.0804(5)$	
HM2/	S	$0.1734(4)$			$0.300(1)$		$0.280(1)$	
RES	$S+I$	$-0.0799(3)$			$-0.1437(8)$		$-0.1325(7)$	

Table 81: Cross sections (fb) for $gg\ (\to H) \to VV \to 4$ leptons processes in pp collisions at $\sqrt{s} = 13$ TeV in the SM. Results for the Higgs signal (S), the signal including signal-background interference (S+I) as well as the interfering background without Higgs contribution (gg bkg.) are given. Minimal cuts are applied: $M_{\ell\bar{\ell}} > 10$ GeV, $M_{\ell'\bar{\ell}'} > 10$ GeV. Cross sections are given at loop-induced leading order and for a single lepton flavour (ℓ) or single different-flavour combination (ℓ,ℓ'). γ^* contributions are included in ZZ. The integration error is displayed in brackets.

final state	S	S+I	gg bkg.
$\ell\bar{\ell}\ell'\bar{\ell}'$	0.9284(7)	0.6707(8)	4.264(2)
$\ell\bar{\ell}\ell\bar{\ell}$	0.4739(8)	0.3467(8)	1.723(3)
$\ell\bar{\ell}\nu_{\ell'}\bar{\nu}_{\ell'}$	1.896(2)	1.386(2)	5.730(5)
$\bar{\ell}\nu_l\bar{\nu}_{\ell'}\ell'$	37.95(4)	33.60(4)	45.31(4)
$\bar{\ell}\nu_l\bar{\nu}_l\ell$	36.01(3)	31.19(3)	50.52(4)

Table 82: Cross sections (fb) for $gg\ (\to H) \to VV \to$ semileptonic final states in pp collisions at $\sqrt{s} = 13$ TeV in the SM. Results for the Higgs signal (S), the signal including signal-background interference (S+I) as well as the interfering background without Higgs contribution (gg bkg.) are given. The signal amplitude is calculated at loop-induced leading order. For the semileptonic decay modes, the $\mathcal{O}(g_s^2e^2)$ tree-level as well as the important loop-induced $\mathcal{O}(g_s^2e^4)$ amplitude contributions to the interfering background are taken into account [510]. Minimal cuts are applied: $M_{\ell\bar{\ell}} > 10$ GeV, $M_{q\bar{q}} > 10$ GeV, $p_{Tj} > 25$ GeV. Cross sections are given for a single lepton flavour. Other details as in Table 81.

final state	S	S+I	gg bkg.
$\ell\bar{\ell}d\bar{d}$	1.711(3)	0.96(1)	$1.575(6)\cdot10^3$
$\ell\bar{\ell}u\bar{u}$	1.334(3)	0.750(5)	$2.30(5)\cdot10^3$
$\ell\bar{\nu}_l u\bar{d}$	38.66(5)	30.58(8)	$1.111(3)\cdot10^4$
$\bar{\ell}\nu_l\bar{u}d$	38.68(5)	30.59(8)	$1.112(3)\cdot10^4$

Benchmark cross sections for $qq'(\to qq'H) \to qq'Z(\gamma^*)Z(\gamma^*) \to qq'\ell\bar{\ell}\ell'\bar{\ell}'$ and $qq'(\to qq'H) \to qq'WW \to qq'\bar{\ell}\nu_l\bar{\nu}_{\ell'}\ell'$ in pp collisions at $\sqrt{s} = 13$ TeV in the SM with tight and loose VBF cuts are given in Tables 83, 84, 85 and 86. Leading order and next-to-leading order results for the Higgs signal, the signal including signal-background interference as well as the interfering background without Higgs contribution are displayed. Corresponding Higgs invariant mass (for ZZ) and transverse mass (for WW) distributions are shown in Figures 130 and 131, respectively, for loose and tight VBF cuts.

The full set of SM benchmark cross sections and distributions is available at https://twiki.cern.ch/twiki/bin/view/LHCPhysics/LHCHXSWGOFFSHELL.

I.8.3.3 Off-shell and interference benchmark cross sections and distributions: 1-Higgs Singlet Model

The simplest extension of the SM Higgs sector is given by the addition of a singlet field which is neutral under the SM gauge groups. We adopt the definition of the 1-Higgs Singlet Model (1HSM), a.k.a. EW Singlet Model, which is given in Section 13.3 of Ref. [21]. Here, interference benchmark cross sections and distributions in the 1HSM are presented. We employ basis (335) of Ref. [21] and specify four

Table 83: Cross sections for $\mathrm{qq}'(\to \mathrm{qq}'\,\mathrm{H}) \to \mathrm{qq}'\,\mathrm{Z}(\gamma^*)\mathrm{Z}(\gamma^*) \to \mathrm{qq}'\,\ell\bar{\ell}\ell'\bar{\ell}'$ in pp collisions at $\sqrt{s} = 13$ TeV in the SM. Leading order (LO) and next-to-leading order (NLO) results for the Higgs signal (S), the signal including signal-background interference (S+I) as well as the interfering background without Higgs contribution (B) are given. Tight VBF cuts are applied (see main text). Cross sections are given for a single lepton flavour combination. The integration error is displayed in brackets.

σ[fb]		110 GeV $< M_{\mathrm{ZZ}} <$ 140 GeV	$M_{\mathrm{ZZ}} >$ 140 GeV	220 GeV $< M_{\mathrm{ZZ}} <$ 300 GeV	$M_{\mathrm{ZZ}} >$ 300 GeV
S	LO	$6.88(2)\cdot10^{-3}$	$1.2501(9)\cdot10^{-2}$	$1.316(3)\cdot10^{-3}$	$1.0644(9)\cdot10^{-2}$
S+I	LO	$6.92(4)\cdot10^{-3}$	$-1.398(6)\cdot10^{-2}$	$-1.85(3)\cdot10^{-3}$	$-1.126(5)\cdot10^{-2}$
B	LO	$1.0(2)\cdot10^{-4}$	$6.554(4)\cdot10^{-2}$	$1.672(2)\cdot10^{-2}$	$4.126(3)\cdot10^{-2}$
S	NLO	$5.67(4)\cdot10^{-3}$	$1.371(3)\cdot10^{-2}$	$1.234(8)\cdot10^{-3}$	$1.198(3)\cdot10^{-2}$
S+I	NLO	$5.2(6)\cdot10^{-3}$	$-1.55(2)\cdot10^{-2}$	$-1.75(6)\cdot10^{-3}$	$-1.288(9)\cdot10^{-2}$
B	NLO	$5(2)\cdot10^{-5}$	$6.749(9)\cdot10^{-2}$	$1.627(5)\cdot10^{-2}$	$4.400(7)\cdot10^{-2}$

Table 84: Cross sections for $\mathrm{qq}'(\to \mathrm{qq}'\,\mathrm{H}) \to \mathrm{qq}'\,\mathrm{WW} \to \mathrm{qq}'\,\bar{\ell}\nu_{\mathrm{l}}\bar{\nu}_{\ell'}\ell'$ in pp collisions at $\sqrt{s} = 13$ TeV in the SM. Tight VBF cuts are applied (see main text). Cross sections are given for a single lepton flavour combination, but taking into account both charge assignments, e.g. $(\ell, \ell') = (\mathrm{e}, \mu)$ or (μ, e). Other details as in Table 83.

σ[fb]		110 GeV $< M_{\mathrm{WW}} <$ 140 GeV	$M_{\mathrm{WW}} >$ 140 GeV	220 GeV $< M_{\mathrm{WW}} <$ 300 GeV	$M_{\mathrm{WW}} >$ 300 GeV
S	LO	1.7411(9)	$2.370(6)\cdot10^{-1}$	$3.08(2)\cdot10^{-2}$	$1.783(5)\cdot10^{-1}$
S+I	LO	1.740(3)	$-3.00(4)\cdot10^{-1}$	$-4.9(2)\cdot10^{-2}$	$-0.197(3)$
B	LO	$8(2)\cdot10^{-4}$	3.387(2)	0.8642(6)	1.856(2)
S	NLO	1.453(4)	$2.51(2)\cdot10^{-1}$	$2.96(6)\cdot10^{-2}$	$1.95(2)\cdot10^{-1}$
S+I	NLO	1.45(1)	$-3.0(2)\cdot10^{-1}$	$-3(2)\cdot10^{-2}$	$-0.234(9)$
B	NLO	$6.7(7)\cdot10^{-4}$	3.381(6)	0.825(4)	1.933(4)

Table 85: Cross sections for $\mathrm{qq}'(\to \mathrm{qq}'\,\mathrm{H}) \to \mathrm{qq}'\,\mathrm{Z}(\gamma^*)\mathrm{Z}(\gamma^*) \to \mathrm{qq}'\,\ell\bar{\ell}\ell'\bar{\ell}'$ in pp collisions at $\sqrt{s} = 13$ TeV in the SM. Loose VBF cuts are applied (see main text). Other details as in Table 83.

σ[fb]		110 GeV $< M_{\mathrm{ZZ}} <$ 140 GeV	$M_{\mathrm{ZZ}} >$ 140 GeV	220 GeV $< M_{\mathrm{ZZ}} <$ 300 GeV	$M_{\mathrm{ZZ}} >$ 300 GeV
S	LO	$1.202(2)\cdot10^{-2}$	$1.662(2)\cdot10^{-2}$	$2.153(5)\cdot10^{-3}$	$1.351(2)\cdot10^{-2}$
S+I	LO	$1.197(7)\cdot10^{-2}$	$-1.95(2)\cdot10^{-2}$	$-3.34(5)\cdot10^{-3}$	$-1.441(8)\cdot10^{-2}$
B	LO	$2.2(2)\cdot10^{-4}$	$1.3535(7)\cdot10^{-1}$	$3.821(3)\cdot10^{-2}$	$7.909(5)\cdot10^{-2}$
S	NLO	$1.035(4)\cdot10^{-2}$	$1.781(3)\cdot10^{-2}$	$1.993(9)\cdot10^{-3}$	$1.495(3)\cdot10^{-2}$
S+I	NLO	$1.02(2)\cdot10^{-2}$	$-2.04(2)\cdot10^{-2}$	$-3.1(1)\cdot10^{-3}$	$-1.58(2)\cdot10^{-2}$
B	NLO	$2.0(4)\cdot10^{-4}$	$1.346(2)\cdot10^{-1}$	$3.651(5)\cdot10^{-2}$	$8.108(9)\cdot10^{-2}$

benchmark points:

1. $M_{\mathrm{h2}} = 400$ GeV, $\sin\theta = 0.2$,
2. $M_{\mathrm{h2}} = 600$ GeV, $\sin\theta = 0.2$,
3. $M_{\mathrm{h2}} = 600$ GeV, $\sin\theta = 0.4$,
4. $M_{\mathrm{h2}} = 900$ GeV, $\sin\theta = 0.2$,

where $M_{\mathrm{h1}} = 125$ GeV and $\mu_1 = \lambda_2 = \lambda_1 = 0$ for all points. The corresponding Higgs widths are given in Table 87. They have been calculated using FeynRules [520].

Table 86: Cross sections for $qq'(\to qq'H) \to qq'WW \to qq'\bar{\ell}\nu_l\bar{\nu}_{\ell'}\ell'$ in pp collisions at $\sqrt{s} = 13$ TeV in the SM. Loose VBF cuts are applied (see main text). Other details as in Table 84.

σ[fb]		110 GeV $< M_{WW} <$ 140 GeV	$M_{WW} >$ 140 GeV	220 GeV $< M_{WW} <$ 300 GeV	$M_{WW} >$ 300 GeV
S	LO	3.271(2)	$3.325(9)\cdot10^{-1}$	$5.10(3)\cdot10^{-2}$	$2.301(8)\cdot10^{-1}$
S+I	LO	3.278(6)	$-4.79(9)\cdot10^{-1}$	$-9.7(3)\cdot10^{-2}$	$-2.61(7)\cdot10^{-1}$
B	LO	$1.8(3)\cdot10^{-3}$	7.449(5)	2.004(2)	3.830(3)
S	NLO	2.836(7)	$3.46(3)\cdot10^{-1}$	$4.75(7)\cdot10^{-2}$	$2.50(3)\cdot10^{-1}$
S+I	NLO	2.85(5)	$-4.4(2)\cdot10^{-1}$	$-7.6(9)\cdot10^{-2}$	$-2.7(2)\cdot10^{-1}$
B	NLO	$1.8(2)\cdot10^{-3}$	7.402(9)	1.928(4)	3.949(7)

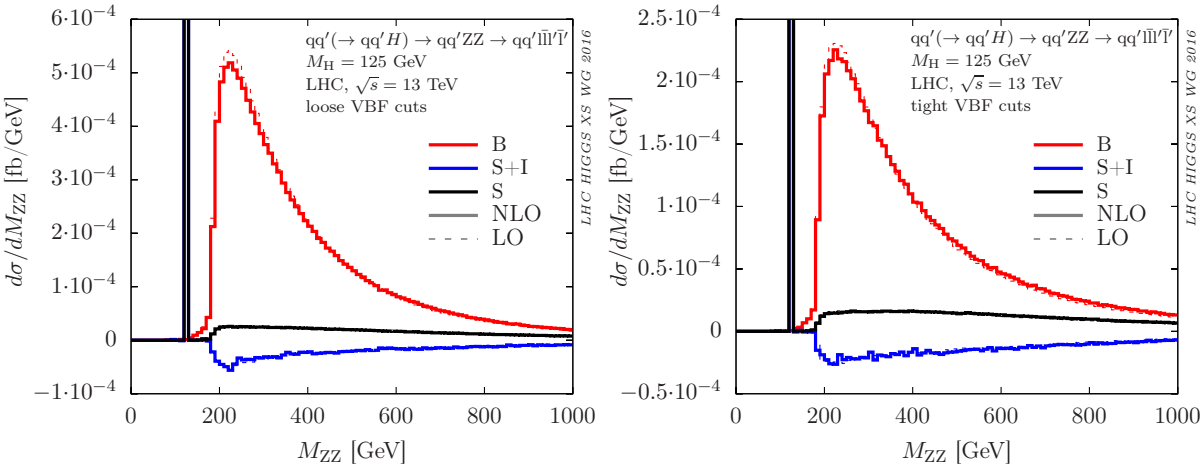

Figure 130: Invariant mass distributions for $qq'(\to qq'H) \to qq'Z(\gamma^*)Z(\gamma^*) \to qq'\ell\bar{\ell}\ell'\bar{\ell}'$ in pp collisions at $\sqrt{s} = 13$ TeV in the SM. Loose and tight VBF cuts are applied in the left and right graphs, respectively. Leading order (dashed) and next-to-leading order (solid) results for the Higgs signal (S), the signal including signal-background interference (S+I) as well as the interfering background without Higgs contribution (B) are given. Cross sections are given for a single lepton flavour combination.

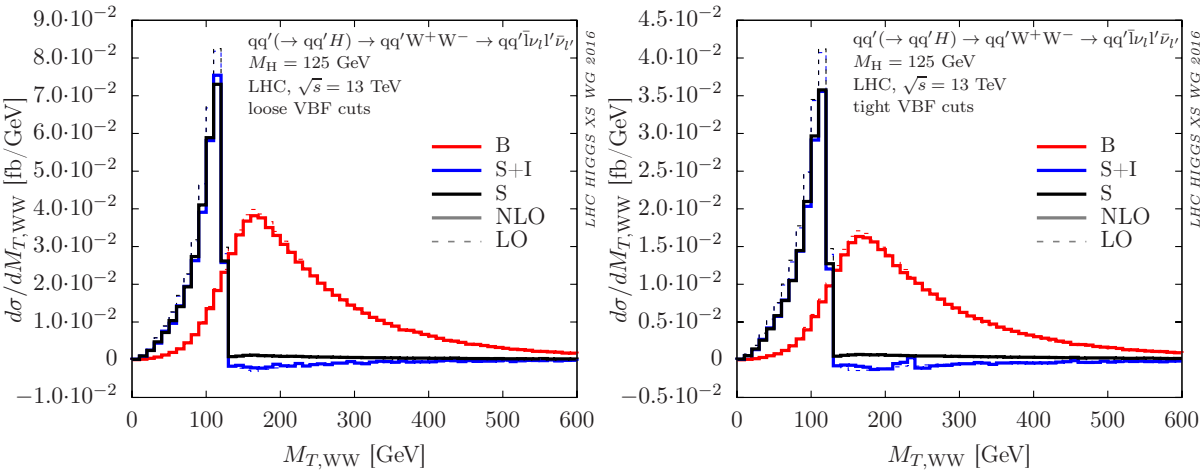

Figure 131: Transverse mass $M_{T,WW}$ (see Eq. (I.8.2)) distributions for $qq'(\to qq'H) \to qq'WW \to qq'\bar{\ell}\nu_l\bar{\nu}_{\ell'}\ell'$ in pp collisions at $\sqrt{s} = 13$ TeV in the SM. Cross sections are given for a single lepton flavour combination, but taking into account both charge assignments, e.g. $(\ell, \ell') = (e, \mu)$ or (μ, e). Other details as in Figure 130.

Table 87: Widths of the physical Higgs bosons h_1 and h_2 in the 1-Higgs-Singlet Extension of the SM with mixing angles $\sin\theta = 0.2$ and $\sin\theta = 0.4$ as well as $\mu_1 = \lambda_1 = \lambda_2 = 0$.

		h_1	h_2		
$\sin\theta$	M [GeV]	125	400	600	900
0.2	Γ [GeV]	$4.34901 \cdot 10^{-3}$	1.52206	5.95419	19.8529
0.4	Γ [GeV]	$3.80539 \cdot 10^{-3}$		22.5016	

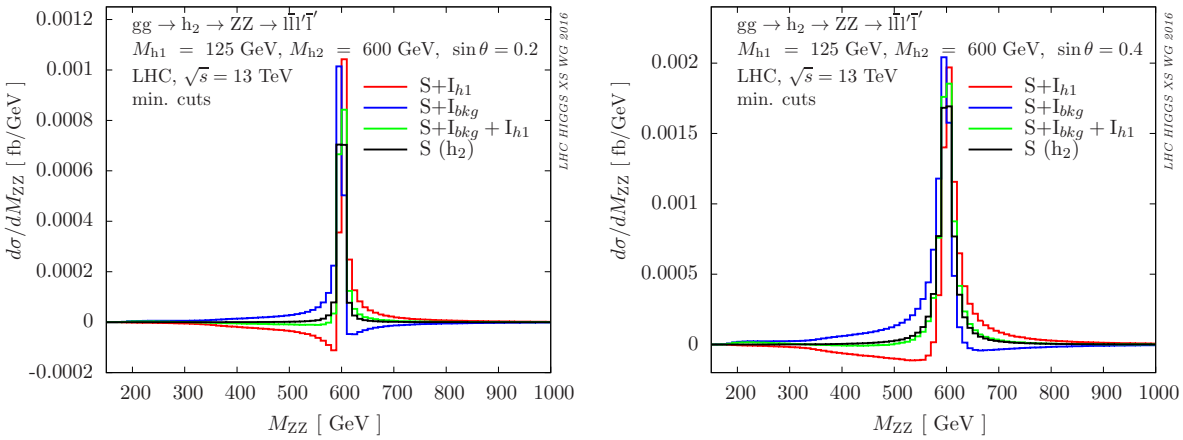

Figure 132: Invariant mass distributions for $gg\ (\to \{h_1, h_2\}) \to Z(\gamma^*)Z(\gamma^*) \to \ell\bar{\ell}\ell'\bar{\ell}'$, other details as in Table 88.

Gluon-fusion 1HSM benchmark results were computed with GG2VV [495] (see also Ref. [521]). More specifically, cross sections for $gg\ (\to \{h_1, h_2\}) \to Z(\gamma^*)Z(\gamma^*) \to \ell\bar{\ell}\ell'\bar{\ell}'$ for the 13 TeV LHC are given in Tables 88 and 89. The corresponding distributions are shown in Figures 132 and 133, respectively. Results for the heavy Higgs signal and its interference with the light Higgs and continuum background and the combined interference are given in Table 88 and Figure 132. In Table 88, the ratio $R_i = (S+I_i)/S$ is used to illustrate the relative change of the heavy Higgs signal due to interference with the light Higgs and continuum background amplitude contributions. Heavy-Higgs-light-Higgs interference effects and the coherent sum of all interfering contributions is shown in Table 89 and Figure 133.

Vector-boson-fusion 1HSM benchmark results were computed with PHANTOM [512] (see also Refs. [513, 522]) and VBFNLO [271, 514] (see also Refs. [515–519]). Good agreement was achieved for all fully-leptonic Higgs decay modes. Cross sections for $qq'(\to qq'\{h_1, h_2\}) \to qq' Z(\gamma^*)Z(\gamma^*) \to qq'\ell\bar{\ell}\ell'\bar{\ell}'$ and $qq'(\to qq'\{h_1, h_2\}) \to qq' WW \to qq'\ell\bar{\nu}_l\bar{\ell}'\nu_{\ell'}$ for the 13 TeV LHC are given in Tables 90 and 92 and Tables 91 and 93 for tight and loose VBF cuts (see Section I.8.3.2), respectively. More specifically, the sum of the light and heavy Higgs contributions including light-heavy interference, the interfering background without Higgs contributions and the sum of the Higgs signal and its interference with the background are given. VBF Higgs invariant mass distributions in the 1HSM are shown in Figure 134.

The full set of 1HSM benchmark cross sections and distributions is available at https://twiki.cern.ch/twiki/bin/view/LHCPhysics/LHCHXSWGOFFSHELL.

Table 88: Cross sections (fb) for $gg\ (\to \{h_1, h_2\}) \to Z(\gamma^*)Z(\gamma^*) \to \ell\bar{\ell}\ell'\bar{\ell}'$ in pp collisions at $\sqrt{s} = 13$ TeV at loop-induced leading order in the 1-Higgs-Singlet Extension of the SM (1HSM) with $M_{h1} = 125$ GeV, $M_{h2} = 400, 600, 900$ GeV and mixing angle $\sin\theta = 0.2$ or 0.4 as indicated. Results for the heavy Higgs (h_2) signal (S) and its interference with the light Higgs (I_{h1}) and the continuum background (I_{bkg}) and the full interference (I_{full}) are given. The ratio $R_i = (S + I_i)/S$ illustrates the relative change of the heavy Higgs signal due to interference with the light Higgs and continuum background amplitude contributions. Cross sections are given for a single lepton flavour combination. Minimal cuts are applied: $M_{\ell\bar{\ell}} > 4$ GeV, $M_{\ell'\bar{\ell}'} > 4$ GeV, $p_{TZ} > 1$ GeV. The integration error is displayed in brackets.

			interference			ratio		
$\sin\theta$	M_{h2} [GeV]	$S(h_2)$	I_{h1}	I_{bkg}	I_{full}	R_{h1}	R_{bkg}	R_{full}
0.2	400	0.07412(6)	0.00682(6)	-0.00171(2)	0.00511(6)	1.092(2)	0.977(1)	1.069(2)
0.2	600	0.01710(2)	-0.00369(3)	0.00384(3)	0.00015(4)	0.784(2)	1.225(2)	1.009(3)
0.2	900	0.002219(2)	-0.003369(9)	0.003058(8)	-0.00031(2)	-0.518(4)	2.378(4)	0.860(6)
0.4	600	0.07065(6)	-0.01191(6)	0.01465(6)	-0.00274(9)	0.831(2)	1.207(2)	1.039(2)

Table 89: Cross sections (fb) for $gg\ (\to \{h_1, h_2\}) \to Z(\gamma^*)Z(\gamma^*) \to \ell\bar{\ell}\ell'\bar{\ell}'$ in pp collisions at $\sqrt{s} = 13$ TeV in the 1HSM with $M_{h1} = 125$ GeV, $M_{h2} = 400, 600, 900$ GeV and mixing angle $\sin\theta = 0.2$ or 0.4 as indicated. Results for the heavy Higgs (h_2) signal (S), light Higgs background (h_1) and continuum background (gg bkg.) are given. Where more than one contribution is included, all interferences are taken into account. Other details as in Table 88.

$\sin\theta$	M_{h2} [GeV]	$S(h_2)$	h_1	gg bkg.	$S + h_1 + I_{h1}$	all
0.2	400	0.07412(6)	0.854(2)	21.18(7)	0.934(2)	21.86(7)
0.2	600	0.01710(2)	0.854(2)	21.18(7)	0.867(2)	21.80(7)
0.2	900	0.002219(2)	0.854(2)	21.18(7)	0.852(2)	21.79(7)
0.4	600	0.07065(6)	0.734(2)	21.18(7)	0.793(2)	21.77(7)

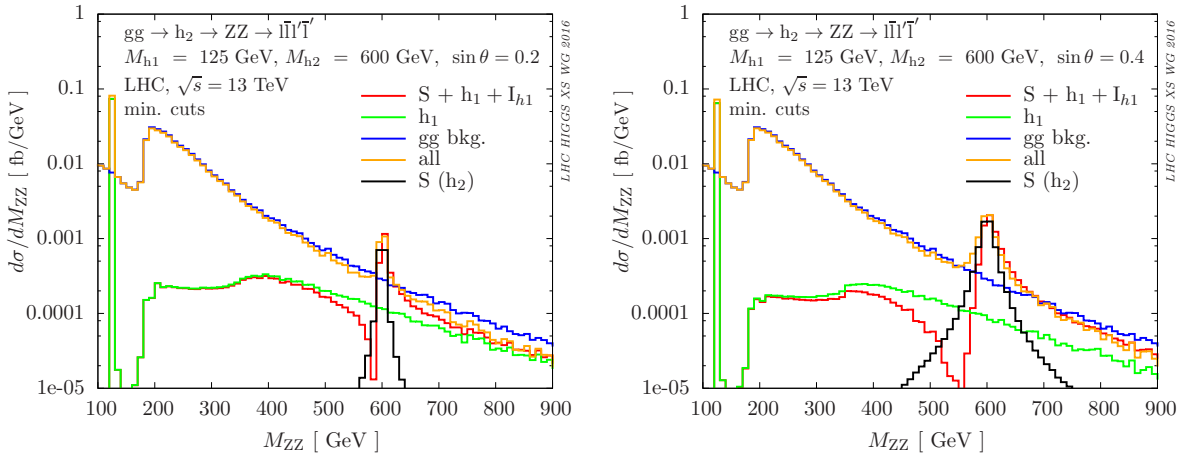

Figure 133: Invariant mass distributions for $gg\ (\to \{h_1, h_2\}) \to Z(\gamma^*)Z(\gamma^*) \to \ell\bar{\ell}\ell'\bar{\ell}'$, other details as in Table 89.

Table 90: Cross sections for $\mathrm{qq}'(\to \mathrm{qq}'\{\mathrm{h}_1, \mathrm{h}_2\}) \to \mathrm{qq}'\,\mathrm{Z}(\gamma^*)\mathrm{Z}(\gamma^*) \to \mathrm{qq}'\,\ell\bar{\ell}\ell'\bar{\ell}'$ in pp collisions at $\sqrt{s} = 13$ TeV in the 1-Higgs-Singlet Extension of the SM (1HSM). Tight VBF cuts (see Section I.8.3.2) are applied. Results are given for the first, second, third and fourth 1HSM benchmark points with $M_{\mathrm{h1}} = 125$ GeV, $\mu_1 = \lambda_2 = \lambda_1 = 0$ and $(M_{\mathrm{h2}}[\mathrm{GeV}], \sin\theta) = (400, 0.2), (600, 0.2), (600, 0.4), (900, 0.2)$, respectively. The sum of the light and heavy Higgs contributions including light-heavy interference (S), the interfering background without Higgs contributions (B) and the sum of the Higgs signal and its interference with the background (S+I) are given. Cross sections are given at leading order and for a single lepton flavour combination. The integration error is displayed in brackets.

σ[fb]	1HSM point	$M_{\mathrm{ZZ}} > 140$ GeV	220 GeV $< M_{\mathrm{ZZ}} <$ 300 GeV	$M_{\mathrm{ZZ}} > 300$ GeV
S	1	$1.686(2)\cdot10^{-2}$	$1.185(4)\cdot10^{-3}$	$1.514(2)\cdot10^{-2}$
S+I	1	$-9.69(3)\cdot10^{-3}$	$-1.85(2)\cdot10^{-3}$	$-6.90(2)\cdot10^{-3}$
B	1	$6.725(2)\cdot10^{-2}$	$1.750(1)\cdot10^{-2}$	$4.148(2)\cdot10^{-2}$
S	2	$1.436(1)\cdot10^{-2}$	$1.232(4)\cdot10^{-3}$	$1.259(1)\cdot10^{-2}$
S+I	2	$-1.180(3)\cdot10^{-2}$	$-1.88(2)\cdot10^{-3}$	$-9.00(2)\cdot10^{-3}$
B	2	$6.725(2)\cdot10^{-2}$	$1.750(1)\cdot10^{-2}$	$4.148(2)\cdot10^{-2}$
S	3	$2.025(2)\cdot10^{-2}$	$8.90(4)\cdot10^{-4}$	$1.895(2)\cdot10^{-2}$
S+I	3	$-4.34(3)\cdot10^{-3}$	$-1.74(2)\cdot10^{-3}$	$-1.72(3)\cdot10^{-3}$
B	3	$6.725(2)\cdot10^{-2}$	$1.750(1)\cdot10^{-2}$	$4.148(2)\cdot10^{-2}$
S	4	$1.263(1)\cdot10^{-2}$	$1.238(4)\cdot10^{-3}$	$1.085(1)\cdot10^{-2}$
S+I	4	$-1.309(3)\cdot10^{-2}$	$-1.86(2)\cdot10^{-3}$	$-1.029(2)\cdot10^{-2}$
B	4	$6.725(2)\cdot10^{-2}$	$1.750(1)\cdot10^{-2}$	$4.148(2)\cdot10^{-2}$

I.8.3.4 Multijet merging effects in $gg \to \ell\bar{\nu}_\ell\bar{\ell}'\nu_{\ell'}$ using SHERPA

I.8.3.4.1 Set-up

In this section, results for the loop–induced process $gg \to \ell\bar{\nu}_\ell\bar{\ell}'\nu_{\ell'}$ obtained with the SHERPA event generation framework [225] will be presented, with the goal to highlight the effect of multijet merging [238] on some critical observables. This is accomplished by directly comparing the results where the leading order processes depicted in Figure 135 have been supplemented with the parton shower (labelled LOOP2+PS) with a sample where an additional jet has been produced, *i.e.* the quark-loop induced processes $gg \to \ell\bar{\nu}_\ell\bar{\ell}'\nu_{\ell'}g$ and $qg \to \ell\bar{\nu}_\ell\bar{\ell}'\nu_{\ell'}q$ (labelled MEPS@LOOP2) as shown in Figure 136. In addition, these two samples are further subdivided into those including a Higgs boson of $m_H = 125$ GeV and those where the Higgs boson has been decoupled with $m_H \to \infty$. Here, the matrix elements are provided from the OPENLOOPS +COLLIER package [243, 244] are being used. For parton showering, the implementation of [351] is employed, with a starting scale

$$\mu_Q^2 = p^2_{\perp,\ell\bar{\nu}_\ell\bar{\ell}'\nu_{\ell'}} + m^2_{\ell\bar{\nu}_\ell\bar{\ell}'\nu_{\ell'}}\,. \tag{I.8.3}$$

A similar analysis, although for centre-of-mass energies of 8 TeV has already been presented in [347]. Here, in addition, the effect of including a Higgs boson with mass $m_H = 125$ GeV is investigated, which was not the case in the previous analysis. Results without the Higgs boson are obtained by effectively decoupling it, pushing its mass to very high values in the calculation, $m_H \to \infty$.

Table 91: Cross sections for $\mathrm{qq}'(\to \mathrm{qq}'\{\mathrm{h}_1,\mathrm{h}_2\}) \to \mathrm{qq}'\,\mathrm{WW} \to \mathrm{qq}'\,\ell\overline{\nu}_\mathrm{l}\overline{\ell}'\nu_{\ell'}$ in pp collisions at $\sqrt{s} = 13$ TeV in the 1-Higgs-Singlet Extension of the SM. Tight VBF cuts are applied. Cross sections are given for a single lepton flavour combination, but taking into account both charge assignments, e.g. $(\ell,\ell') = (\mathrm{e},\mu)$ or (μ,e). Other details as in Table 90.

σ[fb]	1HSM point	$M_{\mathrm{WW}} > 140$ GeV	220 GeV $< M_{\mathrm{WW}} <$ 300 GeV	$M_{\mathrm{WW}} > 300$ GeV
S	1	$3.283(3)\cdot10^{-1}$	$2.68(1)\cdot10^{-2}$	$2.758(3)\cdot10^{-1}$
S+I	1	$-1.98(2)\cdot10^{-1}$	$-4.9(1)\cdot10^{-2}$	$-9.8(1)\cdot10^{-2}$
B	1	3.382(2)	$8.63(1)\cdot10^{-1}$	1.854(1)
S	2	$2.727(3)\cdot10^{-1}$	$2.80(1)\cdot10^{-2}$	$2.189(2)\cdot10^{-1}$
S+I	2	$-2.48(2)\cdot10^{-1}$	$-4.9(1)\cdot10^{-2}$	$-1.48(1)\cdot10^{-1}$
B	2	3.382(2)	0.863(1)	1.854(1)
S	3	$3.937(4)\cdot10^{-1}$	$2.01(1)\cdot10^{-2}$	$3.541(4)\cdot10^{-1}$
S+I	3	$-8.4(2)\cdot10^{-2}$	$-4.6(1)\cdot10^{-2}$	$9(1)\cdot10^{-3}$
B	3	3.382(2)	0.863(1)	1.854(1)
S	4	$2.377(2)\cdot10^{-1}$	$2.81(1)\cdot10^{-2}$	$1.836(2)\cdot10^{-1}$
S+I	4	$-2.75(1)\cdot10^{-1}$	$-4.88(1)\cdot10^{-2}$	$-1.74(1)\cdot10^{-1}$
B	4	3.382(2)	0.863(1)	1.854(1)

Table 92: Cross sections for $\mathrm{qq}'(\to \mathrm{qq}'\{\mathrm{h}_1,\mathrm{h}_2\}) \to \mathrm{qq}'\,\mathrm{Z}(\gamma^*)\mathrm{Z}(\gamma^*) \to \mathrm{qq}'\,\ell\overline{\ell}\ell'\overline{\ell}'$ in pp collisions at $\sqrt{s} = 13$ TeV in the 1-Higgs-Singlet Extension of the SM. Loose VBF cuts are applied. Other details as in Table 90.

σ[fb]	1HSM point	$M_{\mathrm{ZZ}} > 140$ GeV	220 GeV $< M_{\mathrm{ZZ}} <$ 300 GeV	$M_{\mathrm{ZZ}} > 300$ GeV
S	1	$2.272(2)\cdot10^{-2}$	$1.94(1)\cdot10^{-3}$	$1.983(2)\cdot10^{-2}$
S+I	1	$-1.34(1)\cdot10^{-2}$	$-3.33(4)\cdot10^{-3}$	$-8.17(5)\cdot10^{-3}$
B	1	$1.3950(5)\cdot10^{-1}$	$4.005(3)\cdot10^{-2}$	$7.964(4)\cdot10^{-2}$
S	2	$1.889(2)\cdot10^{-2}$	$2.00(1)\cdot10^{-3}$	$1.592(2)\cdot10^{-2}$
S+I	2	$-1.68(1)\cdot10^{-2}$	$-3.40(4)\cdot10^{-3}$	$-1.154(5)\cdot10^{-2}$
B	2	$1.3950(5)\cdot10^{-1}$	$4.005(3)\cdot10^{-2}$	$7.964(4)\cdot10^{-2}$
S	3	$2.590(3)\cdot10^{-2}$	$1.45(1)\cdot10^{-3}$	$2.372(2)\cdot10^{-2}$
S+I	3	$-6.9(1)\cdot10^{-3}$	$-3.12(4)\cdot10^{-3}$	$-2.1(1)\cdot10^{-3}$
B	3	$1.3950(5)\cdot10^{-1}$	$4.005(3)\cdot10^{-2}$	$7.964(4)\cdot10^{-2}$
S	4	$1.658(2)\cdot10^{-2}$	$2.02(1)\cdot10^{-3}$	$1.359(2)\cdot10^{-2}$
S+I	4	$-1.85(1)\cdot10^{-2}$	$-3.36(4)\cdot10^{-3}$	$-1.329(5)\cdot10^{-2}$
B	4	$1.3950(5)\cdot10^{-1}$	$4.005(3)\cdot10^{-2}$	$7.964(4)\cdot10^{-2}$

Table 93: Cross sections for $\mathrm{qq}'(\to \mathrm{qq}'\{\mathrm{h}_1, \mathrm{h}_2\}) \to \mathrm{qq}'\,\mathrm{WW} \to \mathrm{qq}'\,\ell\overline{\nu}_\ell\overline{\ell}'\nu_{\ell'}$ in pp collisions at $\sqrt{s} = 13$ TeV in the 1-Higgs-Singlet Extension of the SM. Loose VBF cuts are applied. Other details as in Table 91.

σ[fb]	1HSM point	$M_{\mathrm{WW}} > 140$ GeV	220 GeV $< M_{\mathrm{WW}} <$ 300 GeV	$M_{\mathrm{WW}} > 300$ GeV
S	1	$4.600(5)\cdot10^{-1}$	$4.46(1)\cdot10^{-2}$	$3.692(4)\cdot10^{-1}$
S+I	1	$-3.25(4)\cdot10^{-1}$	$-9.3(2)\cdot10^{-2}$	$-1.23(3)\cdot10^{-1}$
B	1	7.424(3)	2.001(1)	3.815(2)
S	2	$3.733(3)\cdot10^{-1}$	$4.59(1)\cdot10^{-2}$	$2.805(3)\cdot10^{-1}$
S+I	2	$-4.05(4)\cdot10^{-1}$	$-9.2(2)\cdot10^{-2}$	$-2.00(3)\cdot10^{-1}$
B	2	7.424(3)	2.001(1)	3.815(2)
S	3	$5.17(1)\cdot10^{-1}$	$3.33(1)\cdot10^{-2}$	$4.482(5)\cdot10^{-1}$
S+I	3	$-1.88(4)\cdot10^{-1}$	$-8.5(2)\cdot10^{-2}$	$+1(3)\cdot10^{-3}$
B	3	7.424(3)	2.001(1)	3.815(2)
S	4	$3.274(3)\cdot10^{-1}$	$4.65(1)\cdot10^{-2}$	$2.339(3)\cdot10^{-1}$
S+I	4	$-4.43(4)\cdot10^{-1}$	$-9.6(2)\cdot10^{-2}$	$-2.38(3)\cdot10^{-1}$
B	4	7.424(3)	2.001(1)	3.815(2)

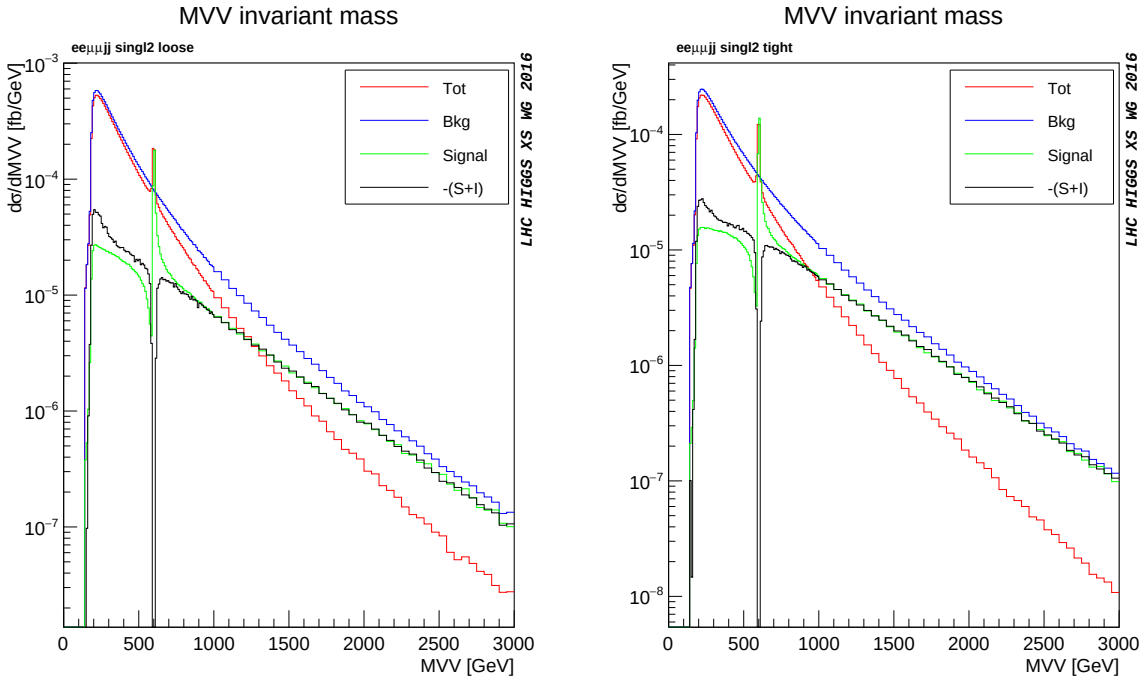

Figure 134: Invariant mass distributions for $\mathrm{qq}'(\to \mathrm{qq}'\{\mathrm{h}_1, \mathrm{h}_2\}) \to \mathrm{qq}'\,\mathrm{Z}(\gamma^*)\mathrm{Z}(\gamma^*) \to \mathrm{qq}'\,\ell\overline{\ell}\ell'\overline{\ell}'$ in pp collisions at $\sqrt{s} = 13$ TeV. Loose and tight VBF cuts are applied in the left and right graphs, respectively. Results for the second 1HSM benchmark point ($M_{\mathrm{h1}} = 125$ GeV, $M_{\mathrm{h2}} = 600$ GeV, $\sin\theta = 0.2$) are shown: the sum of the light and heavy Higgs contributions including light-heavy interference (Signal), the interfering background without Higgs contributions (Bkg), the sum of Signal and Bkg including interference (Tot), and the negative of the sum of Signal and its interference with Bkg (-(S+I)). Other details as in Table 90.

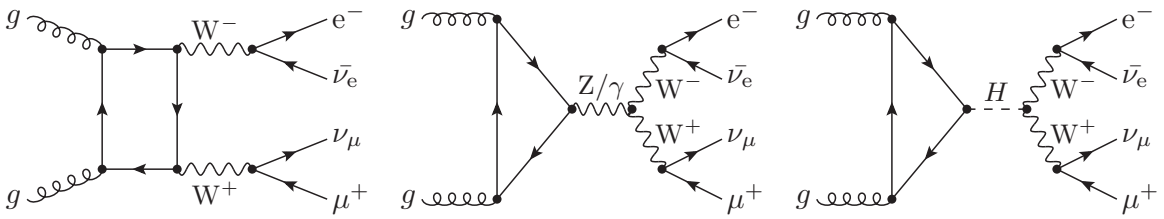

Figure 135: Leading order Feynman diagrams contributing to $gg \to \ell\bar{\nu}_\ell\bar{\ell}'\nu_{\ell'}$.

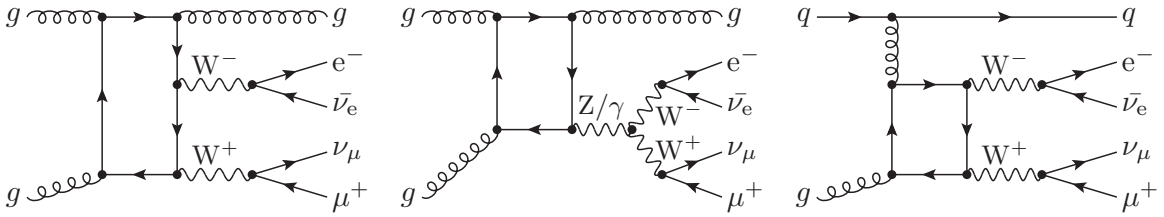

Figure 136: Leading order Feynman diagrams contributing to the background production of final states $\ell\bar{\nu}_\ell\bar{\ell}'\nu_{\ell'}$+jet through a quark loop.

I.8.3.4.2 Results

In this investigation the following cuts have been applied:

$$\begin{aligned} p_{\perp,\ell} &\geq 25\,\text{GeV}\,, & |\eta_\ell| &\leq 2.5 \\ p_{\perp,j} &\geq 30\,\text{GeV}\,, & |\eta_j| &\leq 5\,, \end{aligned}$$

where jets are defined by the anti-k_T algorithm with $R = 0.4$. In addition a cut on the missing transverse momentum has been applied,

$$\not{E}_T \geq 25\,\text{GeV}\,, \tag{I.8.4}$$

which of course is practically given by the combined neutrino momenta.

In Figure 137 inclusive and exclusive jet multiplicities as obtained from the samples described above are displayed. They clearly show that especially for jet multiplicities $N_{\text{jet}} \geq 1$ the impact of multijet merging is sizable and important. Furthermore, there is a visible difference in the overall rate of about a factor of 2 between the results with and without the Higgs boson. This becomes even more visible when considering cross sections after the application of a jet veto, cf. the right panel of Figure 138. Multijet merging leads to jets that are visibly harder – the LOOP2+PS results fall of very quickly with respect to the merged result, see the left panel of Figure 137. However, since the bulk of the inclusive cross section is related to jet transverse momenta below about 30 GeV, the jet-vetoed cross section saturates relatively quickly and is thus correspondingly independent of the hard tails in transverse momentum. This ultimately leads to effects of the order of about 10% or so from multijet merging. At the same time, in the linear plot of the jet-vetoed cross section the rate difference due to the inclusion of the Higgs boson becomes visible. As expected, these differences manifest themselves in the usual kinematic regions stemming from spin effects in the decay of the W bosons, illustrated in Figure 139. Clearly, the presence of a Higgs boson pushes the leptons closer in phase space. Since the overall rate is dominated by the 0-jet bin, the differences between merged and LO samples are again relatively small, of the order of 10% or below.

To summarise: the application of multijet merging to loop–induced processes $gg \to VV^{(*)}$ leads to visibly harder jet spectra and significantly larger jet multiplicities, irrespective of whether this process is mediated by a Higgs boson or not. It is clearly the overall scale of the process and the fact that the

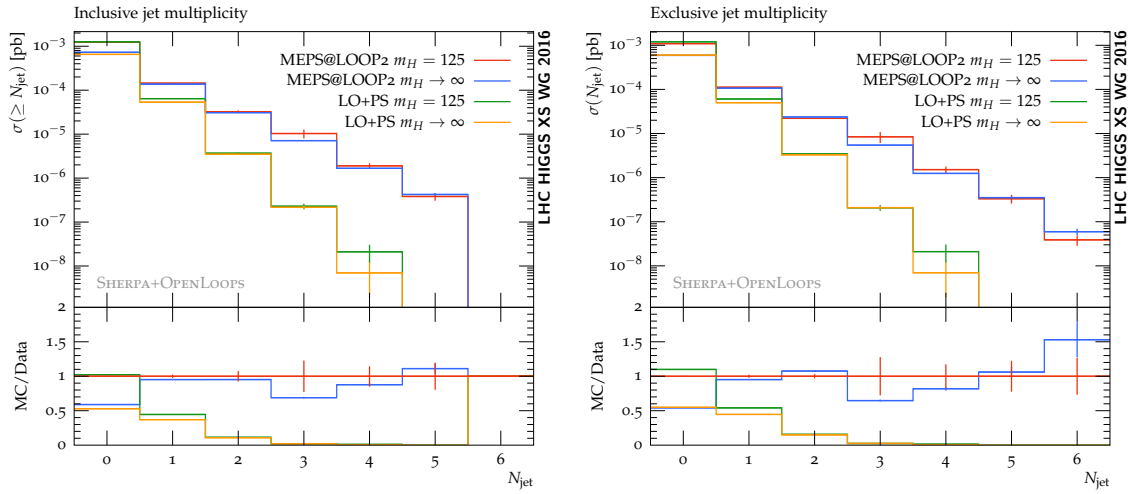

Figure 137: Inclusive (left) and exclusive (right) jet cross sections with and without multijet merging and with ($m_H = 125$ GeV) and without ($m_H \to \infty$) including a Higgs boson, including multijet merging or merely relying on the parton shower to simulate all QCD emissions.

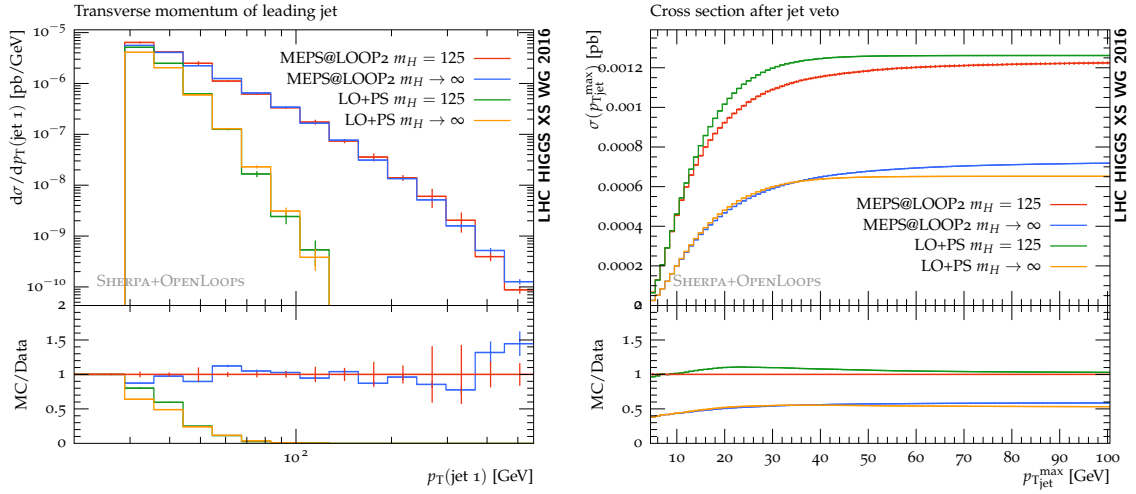

Figure 138: Differential cross section in dependence of the transverse momentum of the leading jet (left) and the cross section after application of a jet veto in dependence of the transverse momentum cut on jets (right).

initial states are identical that is responsible here. The effect on jet-vetoed cross sections in the 0-jet bin is small, 10% or below, since these cross sections essentially appear after integration over the jet-cross section up to the veto scale. Clearly, though, this would be different when asking for exactly one jet and vetoing further jets. The impact of the merging is small on the lepton correlations in the regions that are important for the definition of signal and background regions.

I.8.3.5 Study of higher-order QCD corrections in the gg→H→VV process

I.8.3.5.1 Introduction

The analysis [503] employed to extract the off-shell signal strength in the high mass ($m_{4\ell}$ >220 GeV) ZZ→4ℓ, ZZ→2ℓ2ν and WW→ $\ell\nu\ell\nu$ final states, is based on two Monte Carlo simulations for gg-initiated processes, namely gg2VV [509] and MCFM [497]. The dominant gg-initiated processes used

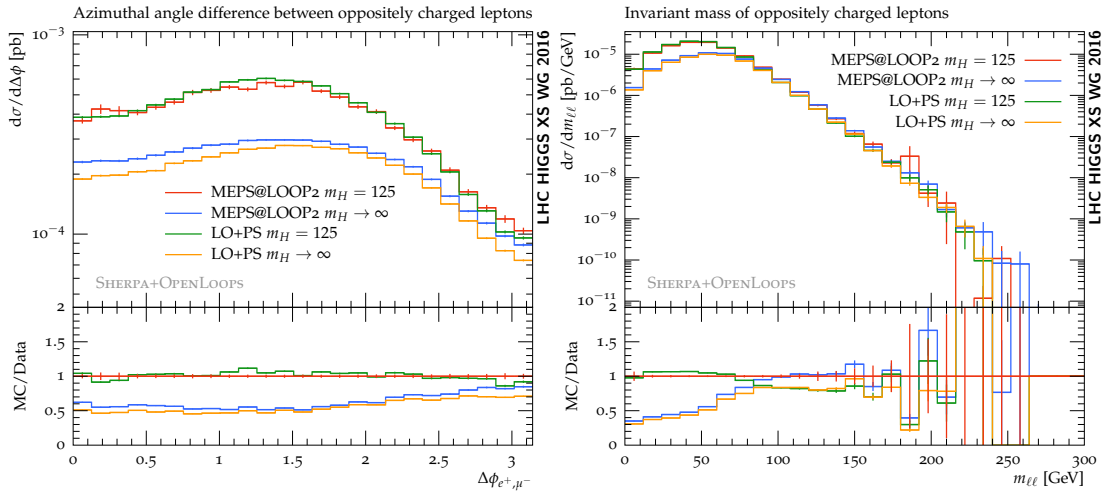

Figure 139: Differential cross section in dependence of the transverse separation of the two leptons (left) and of their invariant mass (right).

in the analysis [503] are listed below:

1. gg→ H → ZZ, the signal (S) comprising both the on-shell peak at m_{H} =125.5 GeV and the off-shell region where the Higgs boson acts as a propagator;
2. gg→ ZZ, the continuum background (B);
3. gg→ (H^*) → ZZ, the signal, continuum background and interference contribution, labelled as SBI in what follows.

However, only Lowest-Order (LO) in QCD Monte Carlo simulations are available, namely gg2VV and MCFM with Pythia8 [313] showering. For this reason, mass-dependent K-factors to higher order accuracy are needed to achieve a better precision.

– For the signal process, higher order QCD corrections are computed: LO to Next-to-Next-to-Leading-Order (NNLO) K-factors are calculated as a function of the diboson invariant mass m_{ZZ}.
– For the background process, the full K-factor from LO to NNLO accuracy is currently not available.

Different approaches exploited in order to take into account the absence of higher order QCD corrections in gg→ (H^*) →VV final states (it is to note that Next-to-Leading Order, NLO, gg→ZZ QCD calculation has been recently performed [523]) and the systematic uncertainties associated to these processes will be detailed in the following Sections.

I.8.3.5.2 Parton Shower Scheme Dependence

Given that no higher order matrix element calculations are available for the gg-initiated processes, the only way to simulate QCD radiation is through the parton shower. However, as the generation is done at LO in QCD, there is no clear prescription to evaluate the systematic uncertainties on the QCD scale. According to the maximum jet p_{T} scale emission characterizing the parton showers, two different configurations [524] are exploited, the *power shower* (the emission is allowed up to the kinematical limit) and the *wimpy shower* (the shower is started at the value of the factorization or the renormalization scale). Pythia8 is tuned as default with the power shower option. The comparison is carried out involving the following parton shower schemes at generator level:

– Pythia8 power shower including a matrix element correction on the first jet emission such that information coming from the exact matrix element calculation is exploited for the hardest jet in the shower [313];

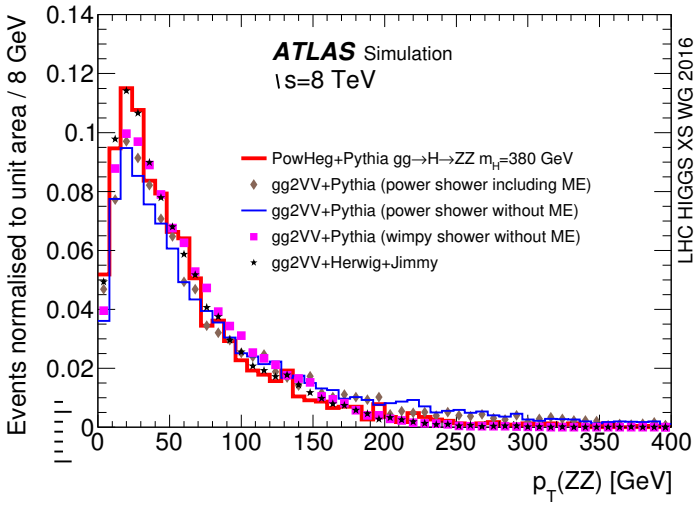

Figure 140: Distribution of p_{T}(ZZ) comparing the NLO generator Powheg showered with Pythia8, the LO generator gg2VV + Pythia (power or wimpy shower), the LO generator gg2VV showered with Jimmy+Herwig. All samples are restricted to the range (345< $m_{4\ell}$ <415) GeV.

– Pythia8 power shower without a matrix element correction;
– Pythia8 wimpy shower without a matrix element correction;
– Herwig6.5 [333] in combination with Jimmy.

The items above are finally compared to high-mass Powheg-Box [76] NLO gg→ H → ZZ event sample with a Higgs boson mass generated with m_{H}=380 GeV, chosen around the most sensitive off-shell invariant mass region for the analysis. The normalized p_{T}(ZZ) distributions, detailed in Figure 140 as reported in Ref. [524] for the sample above in the text are plotted in the same high ZZ mass range (345< $m_{4\ell}$ <415) GeV in order to ensure a compatible mass of the hard interaction system. As the default samples are generated with the LO gg→ (H^*) →ZZ matrix element with Pythia8 using the power shower parton shower option and this sample shows the largest deviation from Powheg, the full difference of the order of 10% is taken as a systematic uncertainty in the ATLAS analysis as in [503].

I.8.3.5.3 Higher order QCD corrections to the transverse momentum and the rapidity of the ZZ system

Higher order QCD corrections for the gg→ ZZ processes are studied using the Sherpa+OpenLoops [225, 243] generator that contains the LO gg→ZZ+1-jet matrix element and merges this with the LO gg→ZZ+ 0-jet matrix element. For the gg→ H → ZZ signal contribution with m_{H}=380 GeV (on-shell signal), the Powheg generator reweighted (as a function of p_{T}) to the HRes2.1 prediction [219] to reach NNLO+NNLL accuracy is also used. Figures 141, 142 and 143 include validation distributions of various comparisons of the variables of interest, namely the transverse momentum, p_{T}(ZZ), and the rapidity, Y(ZZ), of the ZZ system in both on-shell and off-shell mass regions using Powheg+Pythia8, Sherpa+OpenLoops and gg2VV+Pythia8 generators using kinematic variables computed at truth level. The list of cuts applied in the generation level can be found below (p_{T}^{ℓ} is the transverse momentum of each lepton in the final state, $|\eta^{\ell}|$ represents its rapidity [I.51] while m_{Z1} is the Z boson mass closest to the

[I.51] ATLAS uses a right-handed coordinate system with its origin at the nominal interaction point (IP) in the centre of the detector, and the z-axis along the beam line. The x-axis points from the IP to the centre of the LHC ring, and the y-axis points upwards. Cylindrical coordinates (r, ϕ) are used in the transverse plane, ϕ being the azimuthal angle around the beam line. Observables labelled *transverse* are projected into the x-y plane. The pseudorapidity is defined in terms of the polar angle θ as η=-ln tan($\frac{\theta}{2}$).

Z peak, being m_{Z2} the mass of the second lepton pair):

- $m_{4\ell}$ >100 GeV;
- p_T^{ℓ} >3 GeV;
- $|\eta^{\ell}|$ <2.8;
- $m_{Z1,Z2}$ > 4 GeV.

Additional selection criteria are applied on the final state quadruplet (the leptons in the quadruplet are ordered in transverse momentum and denoted with the superscript ℓ in what follows) in the Monte Carlo samples in such a way to mimic the standard selection reported in Ref. [503], namely:

- $p_T^{\ell 1}$ >20 GeV, $p_T^{\ell 2}$ >15 GeV, $p_T^{\ell 3}$ >10 GeV, $p_T^{\ell 4}$ >5 (6) GeV for muons (electrons);
- $|\eta^{\ell}|$ <2.5;
- (50< m_{Z1} <106) GeV;
- if $m_{4\ell}$ <140 GeV → m_{Z2} >12 GeV, if 140< $m_{4\ell}$ <190 GeV → m_{Z2} >0.76·($m_{4\ell}$-140)+12 GeV, if $m_{4\ell}$ >190 GeV → m_{Z2} >50 GeV.

The errors bars in Figures 141, 142 and 143 indicate the statistical uncertainty related to the finite Monte Carlo statistics only. The systematic uncertainties, when applicable, are drawn as shaded boxes, extracted from scale variations on Sherpa+OpenLoops and HRes2.1 as described in the following Section I.8.3.5.4. The systematic uncertainties from the HRes2.1 are applicable here as the Powheg generator is directly reweighted to the HRes2.1 prediction. The results and the distributions reported in the following figures refer to Monte Carlo samples generated at a collision energy $\sqrt{s}$=8 TeV.

As highlighted in Figure 141 (a) for what concerns the on-shell and Figure 141 (b) for the off-shell, the lack of higher QCD calculations in gg2VV results in different p_T spectra (order of 20% in the relevant kinematic region) compared to the higher order Powheg and Sherpa+OpenLoops Monte Carlo. In the high mass region, the off-shell (generated with m_H=125.5 GeV) and on-shell (produced with m_H=380 GeV) Higgs productions with gg2VV match fairly well as shown in Figure 141 (b).
Figure 142 (a) shows that the differences in p_T between Sherpa and gg2VV in the off-shell high mass region are not fully covered by the uncertainties assigned to Sherpa. Since the Sherpa generator has a better treatment of the first hard jet emission, in the H →ZZ→4ℓ analysis, gg2VV is reweighted to the Sherpa prediction in the ATLAS analysis [503]. As for the rapidity distribution reported in Figure 142 (b), no significant difference between gg2VV and Sherpa is present in the high mass region; hence, the reweighting procedure on Y is not necessary.
Figures 142 (c) and (d) stress the fact that the ZZ-transverse momentum and the rapidity of the signal process gg→ (H^*) → ZZ differ from the gg→ ZZ background process and the SBI unlike the gg2VV generator as noted in Figures 143 (a) and (b). This is caused by the presence of the additional matrix element correction to the first jet emission included in Sherpa that generates a different treatment of signal and background components. This statement has been explicitly validated by removing the 1-jet matrix element computation in Sherpa: full compatibility is found between signal and background once the 1-jet ME treatment is removed in Sherpa.

In the analysis deployed by ATLAS [503], the LO gg2VV generator, whose p_T and y distributions are displayed in Figure 143, is reweighted to Sherpa+OpenLoops in the p_T of the VV system to achieve a better description of the p_T spectrum: the impact of the reweighting on the acceptance is calculated to be below 1% for the signal and at the level of 4-6% for the background. In the ZZ→4ℓ channel, the reweighting procedure is only used to account for the acceptance effects, as the matrix-element discriminant employed to disentangle signal and background components is insensitive to the p_T of the ZZ system. For the ZZ→2ℓ2ν channel, the reweighting is applied in both the transverse mass shape and acceptance as the m_T holds dependence on the transverse momentum of the ZZ system.

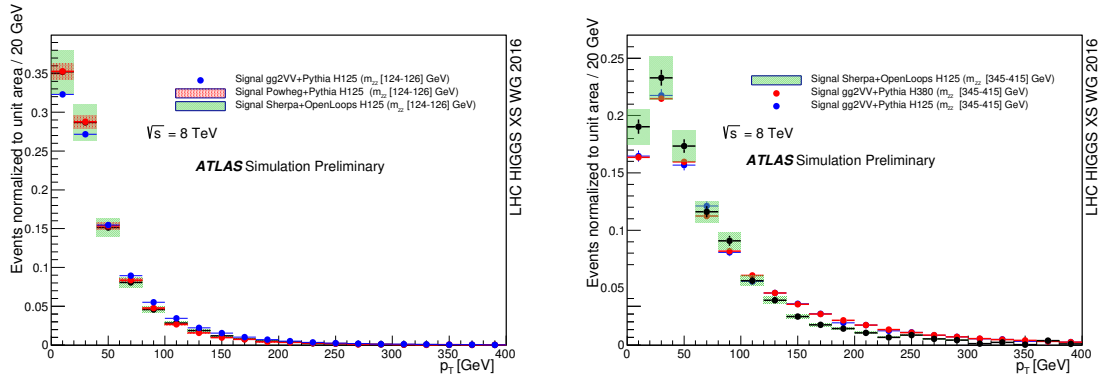

(a) (b)

Figure 141: Comparison of the on-shell gg$\to (H^*) \to$ ZZ signal process in p_{T} (a) generated with m_{H}=125.5 GeV in the mass range $m_{\mathrm{ZZ}} \in$ [124,126] GeV for Powheg, Sherpa and gg2VV. Comparison of the gg$\to (H^*) \to$ ZZ off-shell signal process in p_{T} (b) with m_{H}=125.5 GeV produced with gg2VV and Sherpa and gg$\to (H^*) \to$ ZZ signal process with m_{H}=380 GeV using gg2VV (on-shell) in the region $m_{\mathrm{ZZ}} \in$ [345,415] GeV.

Table 94: Scale variations considered in the evaluation of the theoretical uncertainties related to the p_{T}(ZZ) and Y(ZZ) for the $gg \to H \to$ZZ and $q\bar{q} \to$ZZ processes. The scale variations on Sherpa signal detailed in the second row are also applied on the Sherpa gg$\to$ZZ continuum background as stated in the text. The merging scale for Sherpa has not been modified for this study.

Process	MC	Nominal Scales	Scale variations	# Variations
$gg \to H \to ZZ$	HRes	$\mu_{\mathrm{R}} = \mu_{\mathrm{F}} = \frac{m_{\mathrm{ZZ}}}{2}$	$(\frac{1}{2}\mu_{\mathrm{R/F}}, 2\mu_{\mathrm{R/F}})$, $\frac{1}{2} \leq \mu_{\mathrm{F}}/\mu_{\mathrm{R}} \geq 2$	6
		$\mu_{\mathrm{Q}} = m_{\mathrm{ZZ}}/2$, $\mu_{\mathrm{B}} = m_{\mathrm{b}}$	$(\frac{1}{2}\mu_{\mathrm{Q}}, 2\mu_{\mathrm{Q}})$, $(\frac{1}{4}\mu_{\mathrm{B}}, 4\mu_{\mathrm{B}})$	8
$gg \to H \to ZZ$	Sherpa	$\mu_{\mathrm{R}} = \mu_{\mathrm{F}} = \frac{m_{\mathrm{ZZ}}}{2}$	$(\frac{1}{2}\mu_{\mathrm{R/F}}, 2\mu_{\mathrm{R/F}})$, $\frac{1}{2} \leq \mu_{\mathrm{F}}/\mu_{\mathrm{R}} \geq 2$	6
		$\mu_{\mathrm{Q}} = m_{\mathrm{ZZ}}/2$, $\mu_{\mathrm{B}} = m_{\mathrm{b}}$	$(\frac{1}{\sqrt{2}}\mu_{\mathrm{Q}}, \sqrt{2}\mu_{\mathrm{Q}})$	2
$q\bar{q} \to ZZ$	Powheg	$\mu_{\mathrm{R}} = \mu_{\mathrm{F}} = m_{\mathrm{ZZ}}$	$(\frac{1}{2}\mu_{\mathrm{R/F}}, 2\mu_{\mathrm{R/F}})$	6

I.8.3.5.4 Scale variations on the gg-initiated samples

In order to evaluate the systematic effects on the uncertainties on p_{T} and η in the ZZ frame, the procedure is applied by varying the renormalisation scale (μ_{R}), the factorization scale (μ_{F}), the resummation scale (μ_{Q}) and the resummation scale related to the bottom quark mass (μ_{B}).

The impact of the PDF uncertainties is also evaluated: the nominal PDF set, CT10 [525], applied on the Powheg signal sample at m_{H}=125.5 GeV are compared with MSTW2008 [24] and with NNPDF2.3 [25] in bins of ZZ-transverse momentum and rapidity. Its impact is found to be below 3%.

The Monte Carlo simulations employed for these studies and the full scheme of scale variations applied to these samples are listed in Table 94. Assuming that the resummation scales (μ_{Q} and μ_{B}) variations are independent of the normalization and factorization scales (μ_{R} and μ_{F}), we fix the vector pair (μ_{R}, μ_{F}) while varying μ_{Q} or μ_{B}. Similarly we fix the resummation scales, μ_{Q} and μ_{B}, while varying μ_{R} and μ_{F}. Following the usual prescriptions, the nominal scale of the process is set to $m_{\mathrm{ZZ}}/2$ while the nominal value for the resummation scale related to the bottom mass is set to m_{b} and the Powheg nominal values for renormalisation and factorization scales are set to m_{ZZ}.

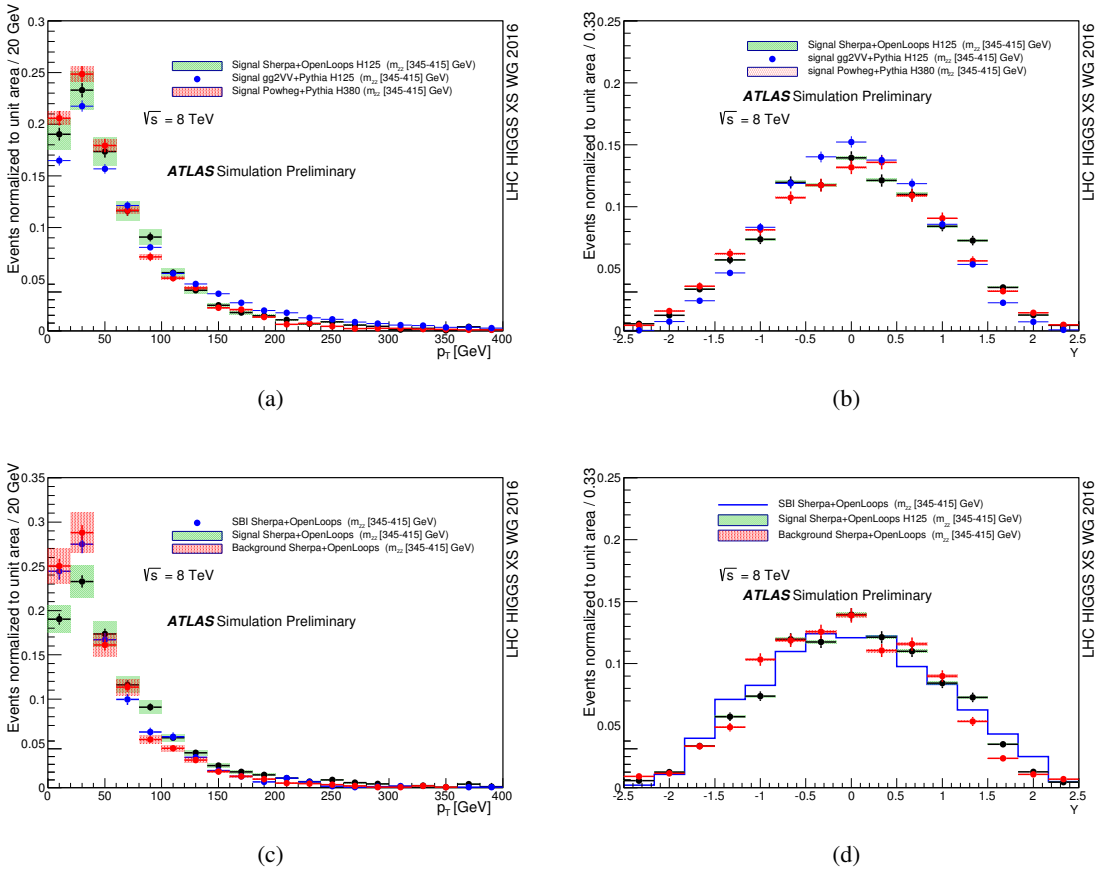

Figure 142: Comparison of the gg$\rightarrow (H^*) \rightarrow$ ZZ off-shell signal process in p_{T} (a) and rapidity (b) generated with m_{H}=125.5 GeV produced with gg2VV and Sherpa and gg$\rightarrow (H^*) \rightarrow$ ZZ signal process with m_{H}=380 GeV using Powheg (on-shell) in the region $m_{\mathrm{ZZ}} \in$ [345,415] GeV. Off-shell comparison in p_{T} (c) and rapidity (d) of the gg$\rightarrow (H^*) \rightarrow$ ZZ signal sample generated with m_{H}=125.5 GeV, the gg$\rightarrow$ ZZ background and the SBI contribution using Sherpa in the mass range $m_{\mathrm{ZZ}} \in$ [345,415] GeV.

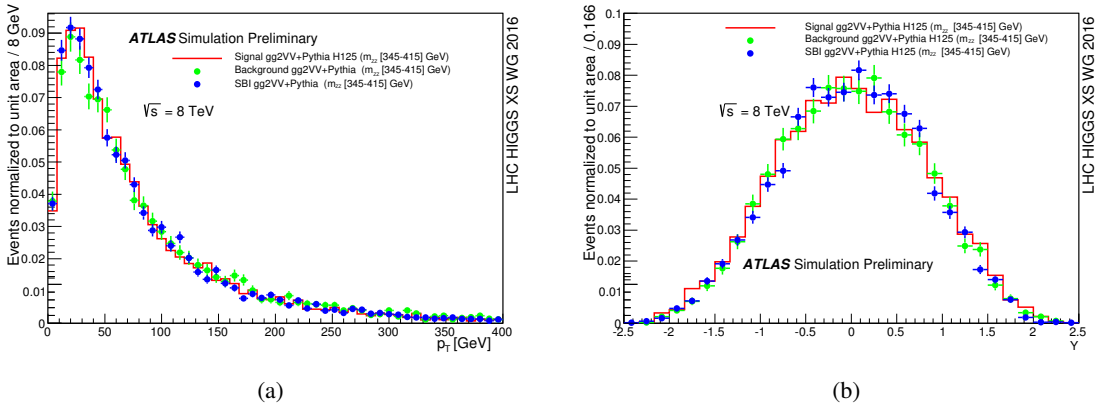

Figure 143: Comparison in p_{T} (a) and rapidity (b) of the three gg2VV contributions (signal generated with m_{H}=125.5 GeV, background and SBI) in the mass region $m_{\mathrm{ZZ}} \in$ [345,415] GeV.

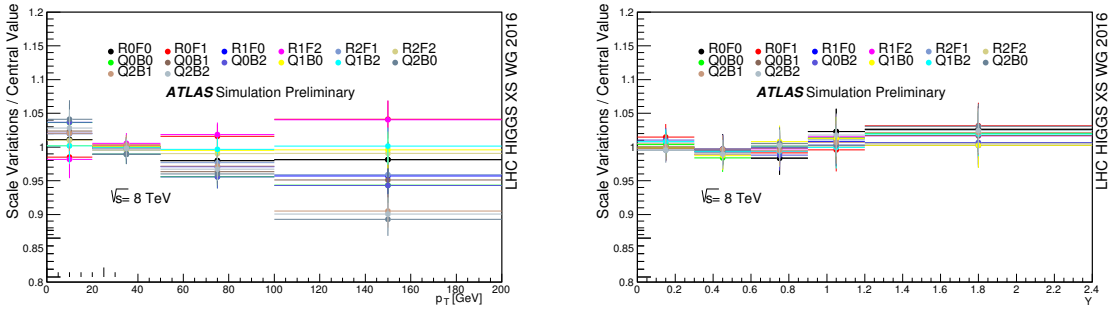

(a) (b)

Figure 144: Relative change of the p_{T} and Y spectra due to the QCD scale variations produced with HRes2.1 signal generated at m_{H}=380 GeV: ratio of the up or down variations p_{T} or rapidity with respect to the nominal distribution. Q labels the resummation scale, B the resummation scale related to the bottom quark mass, R the renormalisation scale, F the factorization scale. The numbers coupled with each variation characterize the nominal value (1), the down variation (0) and the up variation (2).

Figure 144 shows the shape-only variations on p_{T}(ZZ) and Y(ZZ) for a high mass m_{H}=380 GeV gg$\to$ H $\to$ ZZ signal process, produced by QCD scale variations evaluated with the HRes2.1 Monte Carlo generator. The scale variations on the rapidity in Figure 144 (b) can be neglected since they are much smaller than those of the transverse momentum, Figure 144 (a). Figure 145 shows the variation of the signal process (a) and the background processes on p_{T}(ZZ) created with the Sherpa+OpenLoops Monte Carlo sample. The envelope of these independent variations on p_{T}(ZZ) is calculated as the maximal up and down contribution for each p_{T} bin for the HRes2.1 case as well as for Sherpa signal and background. Since the contribution of the resummation scale is dominant, a first envelope encompassing renormalisation and factorization scales summed it in quadrature with the envelope extracted from the resummation scale provides enough accuracy for this study. Note that the Sherpa variations enclose the variations of HRes2.1 because Sherpa does not contain the full NLO calculations, hence its variations are larger than the typical scales of HRes2.1.The systematic uncertainties reported in Ref. [503] associated with the Sherpa-based reweighting in p_{T} of the VV system are assessed by varying the relevant scales in Sherpa: the larger in value between the scale variations in Sherpa and 50% of the difference between Sherpa and gg2VV+Pythia is assigned as the systematic uncertainty. This conservative approach is chosen to consider potential uncertainties not accounted for by the scale variations. The impact of the PDF uncertainties is found to be negligible.

I.8.3.6 Higgs boson off-shell simulation with the MCFM and JHU generator frameworks

The JHU Generator and MELA framework [526–528] is designed for the study of anomalous couplings of a resonance to vector bosons and fermions in various decay and production processes on LHC, and is applicable to either the already discovered boson $H(125)$ or a new resonance $X(m_X)$. In addition to stand-alone generation, the framework is also integrated with the MCFM Monte Carlo package [283, 497, 529] for modeling of the background processes and allows simulation of anomalous couplings in off-shell $H(125)^*$ boson production including interference with continuum diboson production. The simulation of an additional broad resonance X is also included, allowing for the study of a new Higgs-like resonance with arbitrary couplings interfering with the SM processes. The MELA framework allows various likelihood functions either for construction of kinematic discriminants or re-weighting of MC simulation.

The formalism in the JHUGen / MELA framework follows the convention for the tensor structure

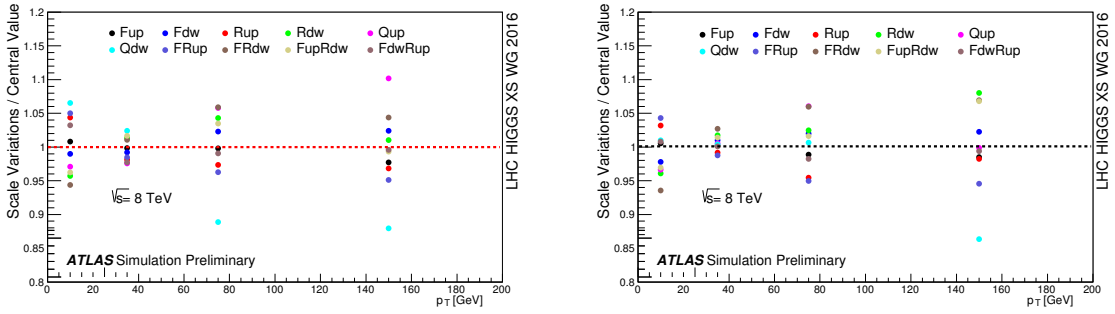

(a) (b)

Figure 145: Relative uncertainties on the p_{T} spectrum for the Sherpa+OpenLoops signal (a) and background (b) samples induced by the QCD scale variations: ratio of the up or down variations with respect to the nominal distribution. Q labels the resummation scale, R the renormalisation scale, F the factorization scale.

of HVV couplings

$$A(\mathrm{H}VV) \propto \left[a_1 - e^{i\phi_{\Lambda Q}}\frac{(q_{V1}+q_{V2})^2}{(\Lambda_Q)^2} - e^{i\phi_{\Lambda 1}}\frac{\left(q_{V1}^2+q_{V2}^2\right)}{(\Lambda_1)^2}\right] m_V^2 \epsilon_{V1}^* \epsilon_{V2}^* + a_2 f_{\mu\nu}^{*(1)} f^{*(2),\mu\nu} + a_3 f_{\mu\nu}^{*(1)} \tilde{f}^{*(2),\mu\nu}, \tag{I.8.5}$$

where $f^{(i)\mu\nu} = \epsilon_{Vi}^{\mu} q_{Vi}^{\nu} - \epsilon_{Vi}^{\nu} q_{Vi}^{\mu}$ is the field strength tensor of a gauge boson with momentum q_{Vi} and polarization vector ϵ_{Vi}, $\tilde{f}_{\mu\nu}^{(i)} = \frac{1}{2}\epsilon_{\mu\nu\rho\sigma} f^{(i),\rho\sigma}$ is the dual field strength tensor. Spin-one and spin-two resonance couplings, higher-order terms in q^2 expansion, and terms asymmetric in q_{V1}^2 and q_{V2}^2 are supported by the generator but are not shown here, see Refs. [526–528] and generator manual for details. The above q^2 expansion is equivalent to the effective Lagrangian notation with operators up to dimension five [530, 531]

$$\begin{aligned}
L(\mathrm{H}VV) \propto \quad & a_1 \frac{m_Z^2}{2} \mathrm{H} Z^{\mu} Z_{\mu} - \frac{\kappa_1}{(\Lambda_1)^2} m_Z^2 \mathrm{H} Z^{\mu} \Box Z_{\mu} - \frac{\kappa_3}{2\,(\Lambda_Q)^2} m_Z^2 \Box \mathrm{H} Z^{\mu} Z_{\mu} \\
& - \frac{1}{2} a_2 \mathrm{H} Z^{\mu\nu} Z_{\mu\nu} - \frac{1}{2} a_3 \mathrm{H} Z^{\mu\nu} \tilde{Z}_{\mu\nu} \\
& + a_1^{\mathrm{WW}} m_{\mathrm{W}}^2 \mathrm{H} \mathrm{W}^{+\mu} \mathrm{W}_{\mu}^{-} - \frac{1}{\left(\Lambda_1^{\mathrm{WW}}\right)^2} m_{\mathrm{W}}^2 \mathrm{H} \left(\kappa_1^{\mathrm{WW}} \mathrm{W}_{\mu}^{-} \Box \mathrm{W}^{+\mu} + \kappa_2^{\mathrm{WW}} \mathrm{W}_{\mu}^{+} \Box \mathrm{W}^{-\mu}\right) \\
& - \frac{\kappa_3^{\mathrm{WW}}}{(\Lambda_Q)^2} m_{\mathrm{W}}^2 \Box \mathrm{H} \mathrm{W}^{+\mu} \mathrm{W}_{\mu}^{-} - a_2^{\mathrm{WW}} \mathrm{H} \mathrm{W}^{+\mu\nu} \mathrm{W}_{\mu\nu}^{-} - a_3^{\mathrm{WW}} \mathrm{H} \mathrm{W}^{+\mu\nu} \tilde{\mathrm{W}}_{\mu\nu}^{-} \\
& + \frac{\kappa_2^{Z\gamma}}{\left(\Lambda_1^{Z\gamma}\right)^2} m_Z^2 \mathrm{H} Z_{\mu} \partial_{\nu} F^{\mu\nu} - a_2^{Z\gamma} \mathrm{H} F^{\mu\nu} Z_{\mu\nu} - a_3^{Z\gamma} \mathrm{H} F^{\mu\nu} \tilde{Z}_{\mu\nu} \\
& - \frac{1}{2} a_2^{\gamma\gamma} \mathrm{H} F^{\mu\nu} F_{\mu\nu} - \frac{1}{2} a_3^{\gamma\gamma} \mathrm{H} F^{\mu\nu} \tilde{F}_{\mu\nu} - \frac{1}{2} a_2^{\mathrm{gg}} \mathrm{H} G_a^{\mu\nu} G_{\mu\nu}^a - \frac{1}{2} a_3^{\mathrm{gg}} \mathrm{H} G_a^{\mu\nu} \tilde{G}_{\mu\nu}^a,
\end{aligned} \tag{I.8.6}$$

where $V_{\mu\nu} = \partial_{\mu} V_{\nu} - \partial_{\nu} V_{\mu}$, $G_{\mu\nu}^a = \partial_{\mu} A_{\nu}^a - \partial_{\nu} A_{\mu}^a + g f^{abc} A_{\mu}^b A_{\nu}^c$, $\tilde{V}^{\mu\nu} = 1/2 \epsilon^{\mu\nu\alpha\beta} V_{\alpha\beta}$, Z is the Z field, W is the W field, F is the γ field, and G is the g field.

Both on-shell H production and off-shell H^* production are considered. There are no kinematic constraints on either q_{Vi}^2 or $(q_{V1}+q_{V2})^2$, other than the relevant parton luminosities. Since the scale of validity of the nonrenormalizable higher-dimensional operators is *a priori* unknown, effective cut-off scales $\Lambda_{V1,i}, \Lambda_{V2,i}, \Lambda_{H,i}$ are introduced for each term in Eq. (I.8.5) with the form factor scaling the

anomalous contribution g_i^{BSM} as

$$g_i = g_i^{\mathrm{SM}} \times \delta_{i1} + g_i^{\mathrm{BSM}} \times \frac{\Lambda_{V1,i}^2 \Lambda_{V2,i}^2 \Lambda_{H,i}^2}{(\Lambda_{V1,i}^2 + |q_{V1}^2|)(\Lambda_{V2,i}^2 + |q_{V2}^2|)(\Lambda_{H,i}^2 + |(q_{V1} + q_{V2})^2|)} \,. \tag{I.8.7}$$

The $gg \to ZZ/Z\gamma^*/\gamma^*\gamma^* \to 4f$ process is generated at LO in QCD. In simulation shown in Figure 146, the QCD factorization and renormalization scales are chosen to be running as $m_{4\ell}/2$ and NNPDF30 parton structure functions are adopted. In order to include higher-order QCD corrections, LO, NLO, and NNLO signal cross section calculation is performed using the MCFM and HNNLO programs [168, 220, 532] for a wide range of masses using narrow width approximation. The ratio between the NNLO and LO, or between the NLO and LO, values is used as a weight (k-factor). The NNLO k-factors are applied to simulation as shown in Figure 146. While this calculation is directly applicable for signal, it is approximate for background. However, the NLO calculation is available [523, 533] for background for the mass range $2m_Z < m_{4\ell} < 2m_t$. There is a good agreement between the NLO k-factors calculated for signal and background, and any differences set the scale of systematic uncertainties from this procedure.

Two applications of off-shell $H(125)$ simulation are shown in Figure 146. In one case, anomalous HVV couplings introduce distinct kinematics in the mass range $m_{4\ell} > 2m_Z$. In the other case, a hypothetical $X(m_X)$ resonance interferes with both $H(125)$ off-shell tail and the $gg \to 4\ell$ background. In all cases, most general HVV and XVV couplings discussed above are possible. Anomalous coupling parameterization in terms effective fractions of events follows LHC convention [530, 531] and is equivalent to parameterization in Eq. (I.8.5) with $f_{ai} = |a_i|^2\sigma_i/\Sigma_j|a_j|^2\sigma_j$.

I.8.3.7 Interference contributions to gluon-initiated heavy Higgs production in the 2HDM using GoSam

I.8.3.7.1 GoSam

GoSam [223, 224] is a package for the automated calculation of one-loop (and tree-level) amplitudes. It can be used either in standalone mode or as a *One Loop Provider* (OLP) in combination with a Monte Carlo program, where the interface is automated, based on the standards defined in Refs. [356, 357]. GoSam is not a library of pre-computed processes, but calculates the amplitude for the process specified by the user in a *run card* on the fly. In the OLP version, the information for the code generation is taken from the order file generated by the Monte Carlo program. The amplitudes are evaluated using D-dimensional reduction at integrand level [355, 534, 535], which is available through the reduction procedures and libraries Samurai [536, 537] or Ninja [538, 539]. Alternatively, tensorial reconstruction [540] is also available, based on the library `golem95C` [541–543]. The scalar master integrals can be taken from OneLoop [544] or QcdLoop [545].

The GoSam package comes with the built-in model files `sm`, `smdiag`, `smehc`, `sm_complex`, `smdiag_complex`, where the latter two should be used if complex masses and couplings are present in the amplitude. Complex masses, stemming from the consistent inclusion of decay widths for unstable particles at NLO [370], are particularly important for the inclusion of electroweak corrections, which also can be calculated with GoSam [546]. The model files `smehc` contain the effective Higgs-gluon couplings. It has been used for example in the calculation of the NLO corrections to H+3 jet production in gluon fusion [226, 547] and in the calculation of HH+2 jet production in both the gluon fusion and the vector boson fusion channel [444].

Other models can be imported easily, using the `UFO` (Universal FeynRules Output) [548, 549] format. This feature has been exploited for example in Refs. [550, 551].

Therefore, GoSam comprises all the features which are needed to calculate interference effects, both within and beyond the Standard Model. An example for interference effects within the 2-Higgs-Doublet Model will be given below.

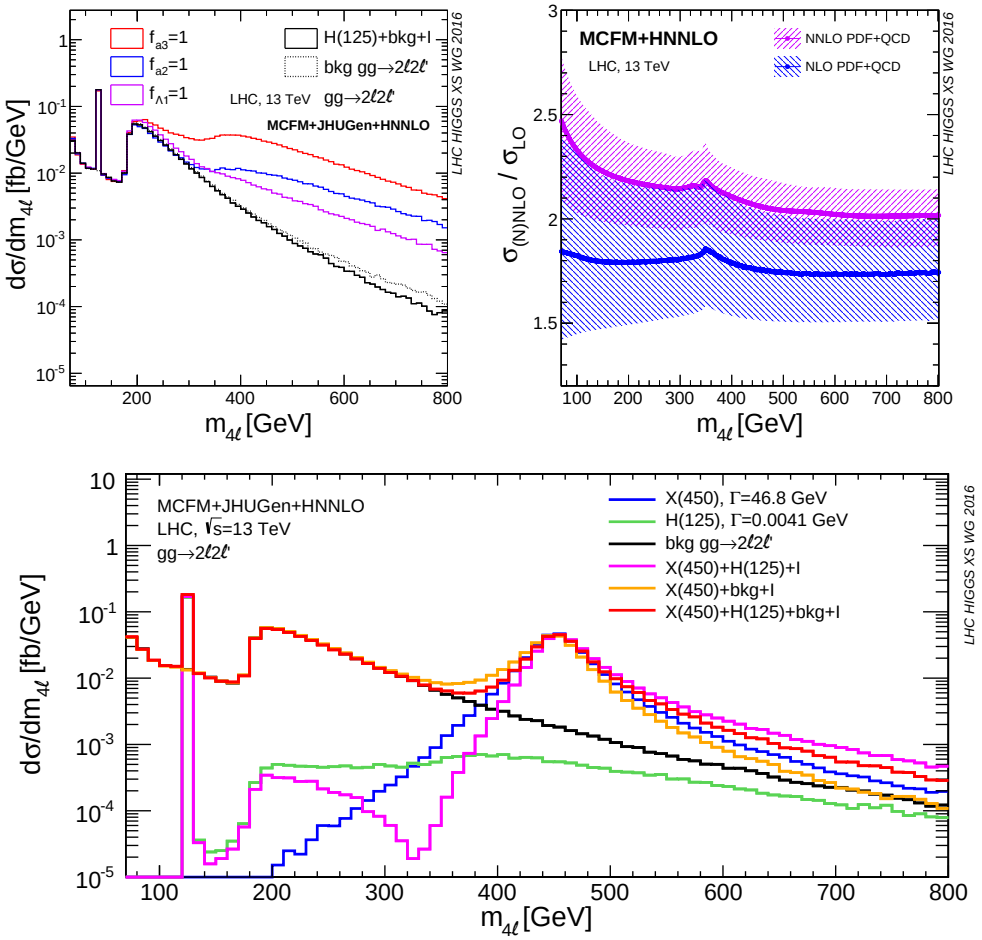

Figure 146: Differential cross section of the process $gg \to ZZ/Z\gamma^*/\gamma^*\gamma^* \to 2\ell 2\ell'$ (where ℓ, $\ell' = e$, μ, or τ) as a function of invariant mass $m_{4\ell}$ generated with the MCFM+JHUGen framework, including the NNLO in QCD weights calculated with MCFM+HNNLO. The NNLO and NLO weights (k-factors) as a function of $m_{4\ell}$ are shown on the top-right plot. The top-left plot shows several scenarios of $H(125)$ anomalous couplings to two weak vector bosons with enhancement in the off-shell region with the a_3, a_2, and Λ_1 terms, as colored histograms, as well as the a_1 term (SM), as the solid black histogram, from Eq. (I.8.5) in decreasing order of enhancement at high mass. The bottom plot shows distributions in the presence of a hypothetical $X(450)$ resonance with several components either isolated or combined. In all cases interference (I) of all contributing amplitudes is included.

I.8.3.7.2 Interference contributions to gluon-initiated heavy Higgs production in the 2HDM

In this section we discuss the loop-induced processes $gg \to ZZ$ and $gg \to VV(\to e^+e^-\mu^+\mu^-/e^+e^-\nu_l\bar{\nu}_l)$ at LO QCD in the context of a CP-conserving Two-Higgs-Doublet-Model (2HDM). In particular, we study the effect of the interference between light and heavy Higgs bosons, and with the background. The 2HDM contains two Higgs doublets, which we name H_1 and H_2. The models can be classified into type I and type II, if we demand no tree-level flavor-changing neutral currents and CP conservation. By convention [481], the up-type quarks couple to H_2. In models of type I, the down-type quarks also couple to H_2, while in type II models, they couple to H_1. The coupling to the leptons can either be through H_1 or H_2, but as our studies are not sensitive to the coupling of the Higgs bosons to leptons, we do not need a further type distinction. The two Higgs doublets form one CP-odd field A and two CP-even Higgs fields h and H due to CP conservation, as well as two charged Higgs bosons $H^\pm$. The 2HDM can be described in different basis representations. We make use of the "physical basis", in which the masses of all physical Higgs bosons, the ratio of the vacuum expectation values $\tan\beta := \tan\beta = v_2/v_1$

Table 95: Relative couplings g_f^ϕ (with respect to the SM coupling) for the two 2HDM types.

Model	g_u^h	g_d^h	g_u^H	g_d^H
Type I	$\cos\alpha/\sin\beta$	$\cos\alpha/\sin\beta$	$\sin\alpha/\sin\beta$	$\sin\alpha/\sin\beta$
Type II	$\cos\alpha/\sin\beta$	$-\sin\alpha/\cos\beta$	$\sin\alpha/\sin\beta$	$\cos\alpha/\cos\beta$

and the Higgs mixing angle in the CP-even sector α, or alternatively $s_{\beta-\alpha} := \sin(\beta-\alpha)$, are taken as input parameters. We choose $\beta-\alpha$ in between $-\pi/2 \le \beta-\alpha \le \pi/2$, such that $-1 \le s_{\beta-\alpha} \le 1$ and $0 \le c_{\beta-\alpha} \le 1$. Our scenarios are thus specified by the two angles α and β, which completely determine the relative couplings (with respect to the couplings of a SM Higgs boson) of the light and the heavy Higgs boson to quarks and the heavy gauge bosons. They are provided in Eq.(I.8.8) and Table 95 (together with Eq.(I.8.9) for a decomposition in terms of $\beta-\alpha$ and β). Moreover, our analysis is sensitive to m_h and m_H, whereas it is rather insensitive to the mass of the pseudoscalar m_A and the heavy charged Higgs boson mass $m_{H^\pm}$, as long as they are heavy enough not to open decay modes of the heavy Higgs H into them and as long as the decay mode $H \to hh$ is sub-dominant. The strengths of the Higgs boson couplings to the gauge bosons $V \in \{W, Z\}$ are given by

$$g_V^h = \sin(\beta-\alpha) =: s_{\beta-\alpha}, \qquad g_V^H = \cos(\beta-\alpha) =: c_{\beta-\alpha} \quad . \tag{I.8.8}$$

The pseudoscalar has no lowest-order couplings to a pair of gauge bosons. It can in principle contribute to the considered processes with four fermions in the final state. Because of the suppression of the Yukawa couplings to leptons, however, these contributions are very small, and thus diagrams involving the pseudoscalar are not of relevance for our discussion. In case of $|s_{\beta-\alpha}| = 1$ the light Higgs boson h couples to the gauge bosons with same strength as the SM Higgs boson. In contrast the coupling of the heavy Higgs boson g_V^H vanishes according to the sum rule $(g_V^h)^2 + (g_V^H)^2 = 1$. Of large relevance for our discussion are the relative couplings of the heavy Higgs boson to bottom-quarks and top-quarks, which are given by

$$\begin{aligned} g_t^H &= \frac{\sin\alpha}{\sin\beta} = -s_{\beta-\alpha}\frac{1}{\tan\beta} + c_{\beta-\alpha}, \\ \text{Type I: } g_b^H &= \frac{\sin\alpha}{\sin\beta} = -s_{\beta-\alpha}\frac{1}{\tan\beta} + c_{\beta-\alpha}, \quad \text{Type II: } g_b^H = \frac{\cos\alpha}{\cos\beta} = s_{\beta-\alpha}\tan\beta + c_{\beta-\alpha} \quad . \end{aligned} \tag{I.8.9}$$

I.8.3.7.2.1 Details of the calculation

We make use of GoSam [223, 224] to discuss the processes $gg \to e^+e^-\mu^+\mu^-$ and $e^+e^-\nu_l\bar{\nu}_l$ (including all three neutrino flavors). For a study of the relevance of interference contributions we also consider the process $gg \to ZZ$, which we generated with the help of `FeynArts` [552] and `FormCalc` [553] and linked to `LoopTools` [553] for the calculation of the employed one-loop Feynman diagrams. We added its amplitudes to a modified version [288] of `vh@nnlo` [287]. It allows to be linked to `2HDMC` [554] which we need for the calculation of the Higgs boson widths Γ_h and Γ_H. In the case of the four lepton final state we have to sum over all possible intermediate configurations leading to the given final state. This particularly means that depending on the sub-process, also intermediate W-bosons as well as non-resonant contributions and photon exchange have to be taken into account. For the numerical integration over the four particle phase space we have combined the GoSam amplitudes with the integration routines provided by `MadEvent` [555, 556].

It is well-known that the calculation of processes including internal Higgs bosons, in particular if one includes higher orders, needs a gauge invariant formulation of the Higgs boson propagator. Since we are working at LO QCD only, a simplistic Breit-Wigner propagator is sufficient for all our purposes. We

Table 96: 2HDM scenarios considered in our analysis.

Scenario	2HDM type	$\tan\beta$	$s_{\beta-\alpha}$	m_H	Γ_H
S1	II	2	-0.995	200 GeV	0.0277 GeV
S2	II	1	0.990	400 GeV	3.605 GeV
S3	I	5	0.950	400 GeV	2.541 GeV
S4	II	20	0.990	400 GeV	5.120 GeV

checked our modified `vh@nnlo` and our GoSam implementations against each other for $gg \to ZZ$ at the amplitude level and reproduced parts of the results presented in Ref. [521] for the four leptonic final state within the numerical uncertainties.
We consider four benchmark scenarios to cover different aspects of a heavy Higgs boson in the phenomenology of a 2HDM, given in Table 96. All scenarios include a light Higgs boson with mass $m_h = 125\,\text{GeV}$. We keep the couplings of the light Higgs close to the ones of the SM Higgs by a proper choice of $\tan\beta$ and $s_{\beta-\alpha}$. The masses (and widths) of quarks and gauge bosons are set to $m_t = 172.3\,\text{GeV}, m_b(m_b) = 4.16\,\text{GeV}, m_Z = 91.1876\,\text{GeV}, m_W = 80.398\,\text{GeV}, \Gamma_Z = 2.4952\,\text{GeV}, \Gamma_W = 2.085\,\text{GeV}$.

Our studies presented here are carried out for the LHC with a centre-of-mass energy of $\sqrt{s} = 13\,\text{TeV}$. The role of interference effects is a bit less pronounced at $7/8$ TeV compared to 13 TeV. We make use of `CT10nnlo` [525] as PDF set for the gluon luminosities. Since our calculations are purely performed at LO the renormalization scale dependence enters through the strong coupling α_s only, which we take from the employed PDF set. We choose the renormalization and factorization scale to be dynamical, namely half of the invariant mass of the gauge boson system $\mu_R = \mu_F = m_{VV}/2$, i.e. $\mu_R = \mu_F = m_{4l}/2$ in case of the four leptonic final states. It is known to have a small effect on the cross section [497, 557], which we numerically confirm for the processes under consideration. In case of the four lepton or the two lepton and two neutrino final states, we additionally cut on the transverse momentum and the pseudorapidity of each lepton l, $p_T^l > 10\,\text{GeV}$ and $|\eta_l| < 2.7$, the R-separation between individual leptons $R^{ll'} > 0.1$ as well as $m_{ll} > 5\,\text{GeV}$, where ll is an oppositely charged same-flavour dilepton pair. For the neutrinos we ask for a total missing transverse momentum of $E_T^{\text{miss}} > 70\,\text{GeV}$. The cuts are inspired by the recent ATLAS analysis carried out in Ref. [558]. One of the most important observables is certainly the invariant mass distribution of the four leptons as the two Higgs bosons manifest themselves in Breit-Wigner peaks in this distribution. For the process $gg \to e^+e^-\mu^+\mu^-$ this observable m_{4l} is also experimentally easily accessible due to two electrons and two muons in the final state. In the cases with neutrinos in the final state the situation is more involved. The invariant mass is no longer an observable that is experimentally accessible but only a transverse component can be measured. If one is interested in a heavy Higgs boson that will decay into the four leptons via two intermediate electroweak gauge bosons a sensible choice is to consider the transverse mass of the underlying two boson system. In our case the two boson system can be ZZ as well as WW. We therefore define a general transverse mass via [559]

$$m_{VV,T}^2 = \left(E_{T,ll} + E_{T,\nu\nu}\right)^2 - \left|\vec{p}_{T,ll} + \vec{p}_{T,\nu\nu}\right|^2 , \tag{I.8.10}$$

with

$$E_{T,ll} = \sqrt{p_{ll}^2 + \left|\vec{p}_{T,ll}\right|^2} , \quad \text{and} \quad E_T^{\text{miss}} = E_{T,\nu\nu} = \left|\vec{p}_{T,\nu\nu}\right| . \tag{I.8.11}$$

I.8.3.7.2.2 Discussion of four fermionic final states

We exemplify the results for the four fermionic final state by discussing the results of scenario S1. Figure 147 shows the invariant mass distribution of the four leptons for $gg \to e^+e^-\mu^+\mu^-$ and the transverse

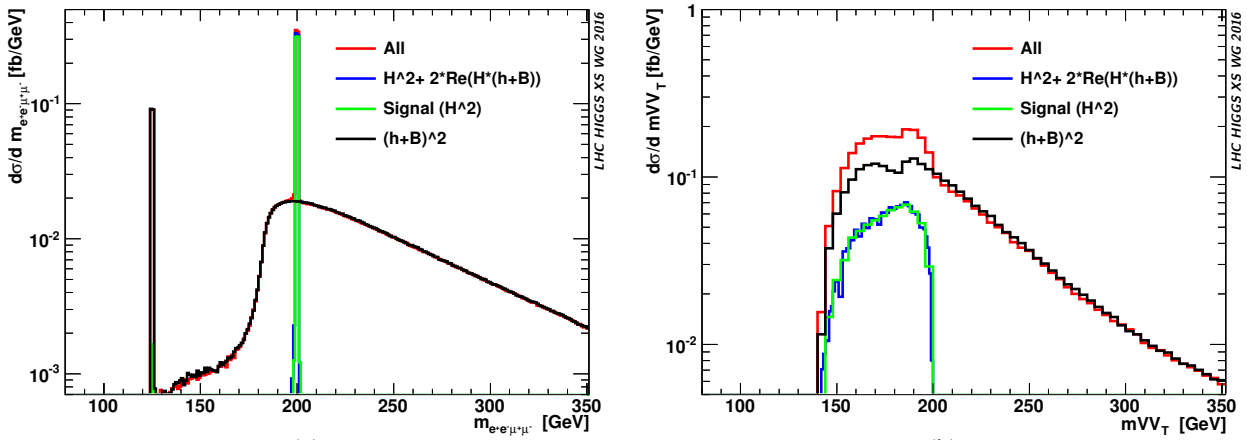

(a) (b)

Figure 147: (a) Invariant mass distribution for $gg \to e^+e^-\mu^+\mu^-$ and (b) transverse mass distribution for $gg \to e^+e^-\nu_l\bar{\nu}_l$ for scenario S1 at $\sqrt{s} = 13\,\text{TeV}$.

mass distribution using the definition in Eq.(I.8.10) for the processes involving final state neutrinos. We distinguish four different contributions. In red, denoted with 'All', we plot all contributions that lead to the given final state in the considered scenario. In green, we only plot the contribution from the heavy Higgs boson, whereas in blue we also add the interference of the heavy Higgs boson with the background and the light Higgs boson. The contribution $|h+B|^2$, plotted in black, contains besides the contributions without any Higgs also contributions of the light Higgs as well as the interference contributions of the light Higgs boson with non-Higgs diagrams.
In the invariant mass plot of $gg \to e^+e^-\mu^+\mu^-$, see Figure 147 (a), the two Higgs boson peaks at $m_{4l} = 125$ and 200 GeV can be clearly seen. Due to the very small width of the heavy Higgs boson there is no distortion of the Breit-Wigner shape visible, and also the impact of the interference contribution to the total height of the peak is rather small. The transverse mass distribution for $gg \to e^+e^-\nu_l\bar{\nu}_l$ shows a quite different pattern. First of all there is no peak from the light Higgs boson. The reason for this are the different cuts compared to the process without neutrinos. The requirement of $E_T^{\text{miss}} > 70\,\text{GeV}$ excludes this region of phase space. Due to the fact that the four momenta of the neutrinos are experimentally not accessible one sets $E_{T,\nu\nu} = \left|\vec{p}_{T,\nu\nu}\right|$, which ignores the invariant mass of the neutrino system. This removes the sharp peak of the heavy Higgs boson, which is visible in the invariant mass distribution of the muon process. Instead of a distinguished peak one obtains a broad distribution. But also here the contribution of the interference remains small. A second difference compared to the muon process is the occurrence of a small dip at around $m_{VV,T} = 180\,\text{GeV}$ in both signal and background. This specific shape is due to the fact that the total contribution to the process with neutrino final state consists of the sum of two different sub-processes, namely the one with the electron neutrino and the ones with muon- and tau neutrino in the final state. Whereas the first sub-process also has contributions from intermediate W-bosons, this is not the case for the latter sub-processes. The two sub-processes therefore show a different kinematical behavior and the sum of the two contributions leads to the given distribution.
For a more detailed discussion of the other scenarios and different observables we refer to Ref. [560].

I.8.3.7.2.3 Relevance of interference contributions

The interference contributions of the heavy Higgs boson with the light Higgs boson and the background are significantly enhanced in two cases: Naturally small couplings involved in the signal process increase the mentioned interferences. This is either of relevance in the decoupling limit of the 2HDM where $s_{\beta-\alpha} \to 1$ and thus the coupling of the heavy Higgs boson to gauge bosons vanishes or through a small

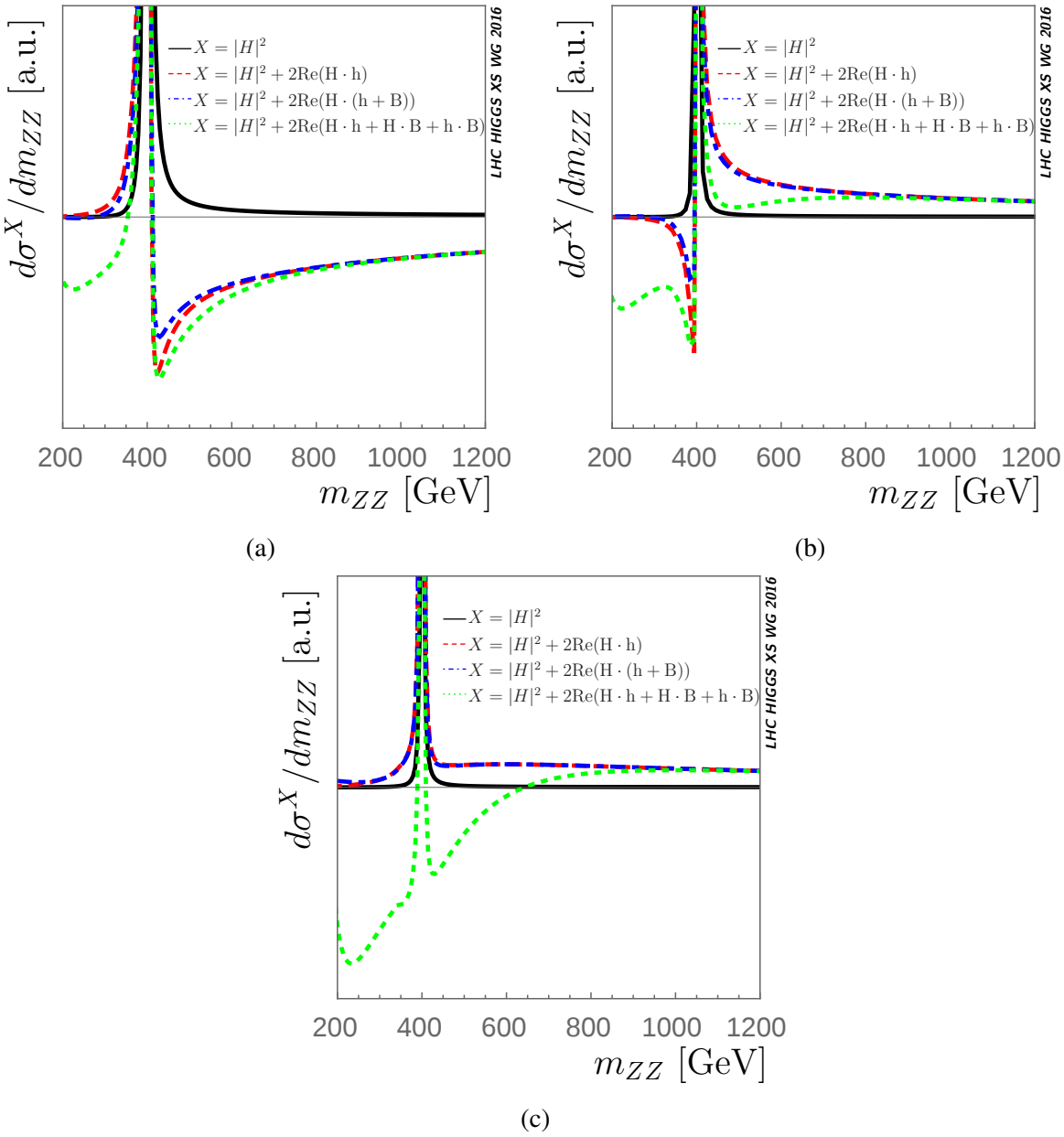

Figure 148: Partonic cross sections $d\sigma^X/dm_{ZZ}$ for $gg \to ZZ$ in arbitrary units as a function of the invariant mass m_{ZZ} in GeV for scenario (a) S2, (b) S3 and (c) S4 (black: $X = |H|^2$; red, dashed: $X = |H|^2 + 2\mathrm{Re}(H \cdot h)$; blue, dot-dashed: $X = |H|^2 + 2\mathrm{Re}(H \cdot h) + 2\mathrm{Re}(H \cdot B)$; green, dotted: $X = |H|^2 + 2\mathrm{Re}(H \cdot h) + 2\mathrm{Re}(H \cdot B) + 2\mathrm{Re}(h \cdot B)$).

coupling of the heavy Higgs boson to top- and/or bottom-quarks. According to Eq. (2) the top-quark coupling vanishes for a specific value of $s_{\beta-\alpha}$ for fixed $\tan\beta$. In a 2HDM type I the bottom-quark coupling vanishes for the same value, such that the cross section $\sigma(gg \to H \to VV)$ gets zero, whereas in a 2HDM type II the cross section is minimal. Moreover the interferences are found to be large for an enhanced bottom-quark Yukawa coupling, i.e. large $\tan\beta$. Again, for further details we refer to Ref. [560]. Interferences in the mentioned two cases can help to lift the signal cross section by more than a factor of 2 and thus enhance the sensitivity of heavy Higgs boson searches.

I.8.3.7.2.4 Interferences at high invariant masses

So far we focused on the interference effects between the heavy Higgs and the background as well as the heavy Higgs and the light Higgs in the vicinity of the heavy Higgs resonance, since the interference between the light Higgs boson and the background can be considered constant in this region. However, at high invariant masses of the diboson system the interplay between all three contributions h and H and the background B is of relevance, to a certain extent related to the unitarization of the cross section. In Figure 148 we plot the differential cross section $gg \to ZZ$ as a function of the invariant mass of the diboson system m_{ZZ} up to high masses beyond the heavy Higgs resonance. We exemplify the discussion for the three scenarios S2, S3 and S4. The differences between the colored curves display the importance of the different interference terms. Since the figures are obtained for the partonic cross section and we are interested in the relative effects of the interferences among each other, we do not display units for $d\sigma/dm_{ZZ}$. At high invariant masses the interference between the heavy Higgs boson and the background is negligible, in contrast to the interference of the light Higgs and the heavy Higgs boson, which remains large and can have either sign. Moreover the smoothly falling interference of the light Higgs boson and the background comes into the game within a certain window of invariant masses below 1 TeV. Figure 148 depicts different cases, where the interference $h \cdot H$ is either negative similar to the interference $h \cdot B$ or leads to a positive contribution to the differential cross section in a region $m_{ZZ} \in [450\,\text{GeV}, 1000\,\text{GeV}]$. The latter case is true for scenarios S3 or S4, where a sign change of the total depicted contribution leads to a dip and a subsequent "peak"-like structure when added to the background. This structure also appears in the total four particle final state, where the gluon luminosities further suppress the cross section at high invariant masses. Thus all interferences need to be taken into account in order to correctly describe the cross section at high invariant masses.

I.8.4 $gg \to VV$ at NLO QCD

I.8.4.1 The status of theoretical predictions

A good theoretical control of the off-shell region requires the knowledge of higher order QCD correction for both the signal $pp \to H \to 4l$ and the SM background $pp \to 4l$ processes. At high invariant masses, the signal $gg \to H \to 4l$ and the background $gg \to 4l$ processes individually grow with energy, eventually leading to unitarity violations. In the SM, a strong destructive interference between signal and background restores unitarity in the high energy regime, and its proper modeling is important for reliable predictions in the off-shell tail. At invariant masses larger than the top threshold $m_{4l} > 2m_t$ the effect of virtual top quarks running in the loops is non negligible and must be taken into account.

The state of the art for theoretical predictions of signal, background and interference is very different. For an exhaustive description of the signal cross section we refer the reader to the relevant sections of this report. As far as perturbative QCD is concerned, the signal is known through NLO with exact quark mass dependence [95, 132]. NNLO corrections are known as an expansion around the $m_t \to \infty$ limit [96, 98, 561], matched to the exact high-energy limit [230] to avoid a spurious growth at high energies [100, 102]. Very recently, the N^{3}LO corrections became available [92] in the infinite top mass approximation. They turned out to be moderate, with a best stability of the perturbative expansion reached for central scale $\mu = M_{\rm H}/2$. So far, results are known as an expansion around threshold, which is expected to reproduce the exact result to better than a percent.

We now briefly discuss the status of theoretical description of the background. In the SM, four-lepton production is dominated by quark fusion processes $q\bar{q} \to VV \to 4l$. Recently, NNLO QCD corrections were computed for both the ZZ [562] and the WW [563] processes, leading to a theoretical uncertainty coming from scale variation of a few percent. In these prediction, the formally NNLO gluon fusion channel $gg \to 4l$ enters for the first time, i.e. effectively as a LO process. At the LHC, it is enhanced by the large gluon flux and corresponds to roughly 60%(35%) of the total NNLO corrections to the $ZZ(WW)$ process. Despite being sub-dominant for $pp \to 4l$ production, the $gg \to 4l$ sub-channel

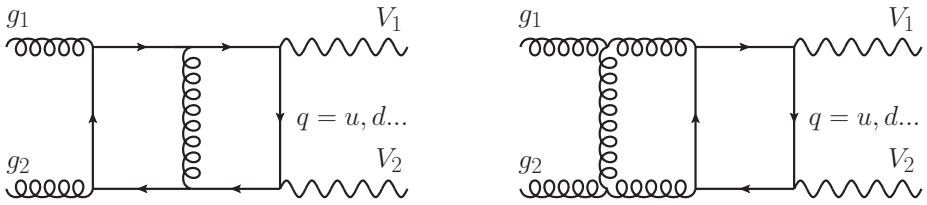

Figure 149: Representative two-loop diagrams for the $gg \to 4l$ process. Leptonic decays of the vector bosons is assumed.

Figure 150: Representative double (left) and single (right) resonant one-loop diagrams for the $gg \to 4l + g$ process.

is of great importance for off-shell studies. First of all, as we already mentioned there is a strong negative interference between $gg \to 4l$ and $gg \to H \to 4l$. Second, the gluon fusion SM background is harder to separate from the Higgs signal.

Computing NLO corrections to $gg \to 4l$ is highly non trivial as it involves the knowledge of complicated two-loop amplitudes with both external and internal massive particles. Parton shower studies based on merged $gg \to 4l + 0, 1$ jet have been performed for example in [347]. Very recently, NLO QCD corrections for $gg \to VV \to 4l$ process were computed in the case of massless quark running in the loop [523, 564]. This approximation is expected to hold very well below threshold, $m_{4l} < 2m_t \sim 300$ GeV. As in the Higgs case, finite top quark effects are known as an expansion in $1/m_t$ [533]. Going beyond that would require computing two-loop amplitudes which are currently beyond our technological reach, so the exact result is not expected in the near future.

I.8.4.2 Brief description of the NLO computation for $gg \to 4l$

I.8.4.2.1 Massless quark contribution

In this section, we briefly report the main details of the $gg \to VV \to 4l$ NLO QCD computations [523, 564]. Despite being NLO calculations, they pose significant technical challenges. First, complicated two-loop amplitude are required, see Figure 149 for a representative sample. These amplitudes were recently computed in [565, 566]. They include decay of the vector bosons and account for full off-shell effects. For the results in [523, 564], the public C++ implementation of Ref. [566] was used. To ensure the result is stable, the code code compares numerical evaluations obtained with different (double, quadruple and, if required, arbitrary) precision settings until the desired accuracy is obtained. For a typical phase space point, the evaluation of all two-loop amplitudes requires about two seconds.

Second, one-loop real emission amplitudes are required, see Figure 150. Despite being only one-loop amplitudes, they must be evaluated in degenerate soft/collinear kinematics, so they must be numerically stable. For the computations in [523, 564], these amplitudes were computed using a mixture of numerical [567] and analytical [568] unitarity. As a cross-check, the obtained amplitudes were compared against OpenLoops [243] for several different kinematic points. Possible numerical instabilities are

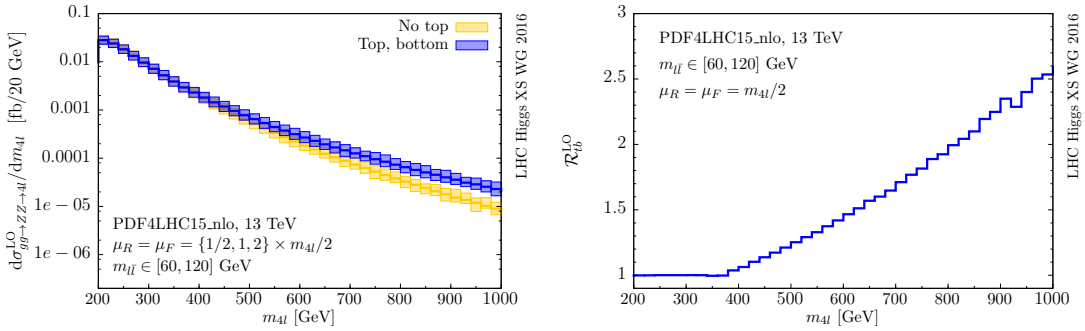

Figure 151: Top quark mass contribution to $gg \to ZZ \to 4l$ at LO. Left: comparison between the exact result (blue) and the approximation where the top quark contribution is omitted and the bottom quark is considered massless (see [523] for details). Right: ratio between the exact and approximate results for the central scale $\mu = m_{4l}/2$. See text for details.

cured by increasing the precision of the computation. The typical evaluation time for a phase space point, summed over color and helicities, is about 0.1 seconds. Also in this case, full decay of the vector bosons into leptons/neutrinos and off-shell effects are understood. Note that the latter involve single-resonant diagrams, see Figure 150(right). Arbitrary cuts on the final state leptons/neutrinos (and additional jet) are possible. In the computations [523, 564], interference between WW and ZZ mediated processes for $2l2\nu$ final states are neglected. They are expected to be irrelevant in the experimental fiducial regions. Full $ZZ/\gamma\gamma$ interference effects are included.

In [523, 564], contributions coming from $qb \to VVq$ mediated by closed fermion loops were not included. This is because at $\mathcal{O}(\alpha_s^3)$ there are several other contributions to the qg channel other than one-loop squared amplitudes, which in principle are not sub-dominant. Neglecting these channels is fully justified in the large gluon approximation of [523, 564]. Residual factorization scale uncertainties are expected to give an estimate of the impact of neglected channels.

In the ZZ computation [523], the top quark contribution is neglected and the bottom quark is considered massless (see [523] for more details). This approximation is expected to work at the 1% level for the total $gg \to ZZ$ cross-section, but it is not reliable in the high invariant mass regime. To quantify this, in Figure 151 we compare at LO the full massive computation with the approximation [523]. From the figure it is clear that below the top threshold the approximation [523] is essentially exact, while above the top quark contribution becomes rapidly important. The relative size of the top quark contribution is quantified in the right panel of Figure 151, where

$$\mathcal{R}^{\rm LO}_{tb}(m_{4l}) \equiv \left. \frac{{\rm d}\sigma^{\rm LO}_{t,b}/{\rm d}m_{4l}}{{\rm d}\sigma^{\rm LO}_{{\rm no}-t}/{\rm d}m_{4l}} \right|_{\mu_r=\mu_f=m_{4l}/2} . \tag{I.8.12}$$

For the WW case, in the calculation [564] both the top and the bottom quark contributions are omitted. At LO, top/bottom contributions account for $\mathcal{O}(10\%)$ of the total $gg \to WW$ cross section.

I.8.4.2.2 Finite top quark effects

The effect of finite top quark mass in $gg \to ZZ$ at NLO was investigated in [533]. Similar to what is done in the Higgs case, the authors performed the computation as an expansion in the $m_t \to \infty$ limit. The first two non trivial terms in the expansion were kept, which allowed for a reliable description of the top quark contribution up to invariant masses of order $m_{4l} \sim 300$ GeV. In this computation, only the total $gg \to ZZ$ cross-section was considered, although this should be enough to have a rough estimate of the size of the mass effects. The result on the NLO corrections, compared to the signal case, are shown in Figure 152. For these results, the Higgs signal is computed in the $m_t \to \infty$ limit as well. Also,

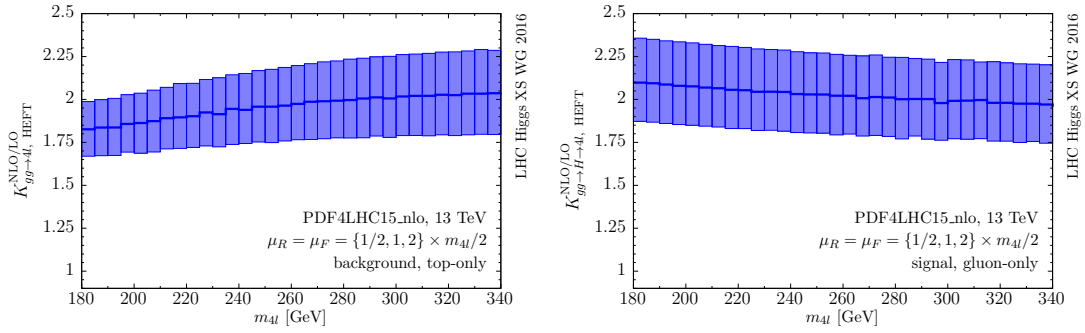

Figure 152: $K-$factors for signal and background, in the heavy top expansion. Both LO and NLO contributions are computed with NLO PDFs and α_s. See text for details.

compared to the K-factor defined in [533], here we used NLO PDFs and α_s evolution for both the LO and the NLO contributions. The band represent scale variation uncertainty, obtained from a factor of two variation around $\mu_0 = m_{4l}/2$.

Close to the ZZ threshold, the background $1/m_t$ expansion is expected to be accurate within $\mathcal{O}(20\%)$ [533]. Signal and $K-$factors are of the same order of magnitude, in agreement with what expected from soft gluon approximations [569]. Below the top threshold, the precision on the approximation [533] can be systematically improved by computing more terms in the $1/m_t$ expansion. Above the top threshold $m_{4l} \sim 300$ GeV, the expansion [533] alone is no longer reliable. Since the full computation is not available, the expansion could be improved along two directions. In principle, it could be matched against the exact high energy behavior. While this does not pose any conceptual challenge, the computation of the high energy limit is technically more involved than in the Higgs case and it is presently unknown. A second option would be to rescale by the exact LO and hence consider and expansion for the $K-$factor, for which the $1/m_t$ expansion should be better behaved.

I.8.4.3 Results and recommendation for the $gg\ (\to H) \to ZZ$ interference K-factor

As explained in the previous section, exact predictions valid up to high ~ 1 TeV invariant masses are only known at NLO for the $gg \to H \to 4l$ signal and LO for the $gg \to 4l$ background. However, several indications point towards sizable higher order corrections, both for signal and background. In this section we study this issue and present a possible practical recommendation for the signal, background and interference $K-$factors.

We start by describing the setup used for the results presented in this section. LO and NLO results are both obtained with NLO PDFs and α_s. In principle, one could envision using LO PDFs (and α_s) for the LO results, and this would in general lead to smaller corrections, with reduced shape dependence. However, since PDFs fits are still dominated by DIS data, the LO gluon distribution is almost entirely determined by DGLAP evolution. The large LO gluon flux hence is artificially driven by the large NLO DIS $K-$factor and it is not reliable. Until LO gluon PDFs are obtained by fitting hadronic data, using the NLO gluon distribution is preferable, see the PDFs section of this report for more details. NNLO PDFs could be used as well, since the $gg \to 4l$ process enters at NNLO in the $q\bar{q} \to 4l$ computation. However, here we are mostly interested in interference effects, so for consistency with the Higgs case we use NLO PDFs for NLO signal, $gg \to 4l$ background and interference.

Regarding the scale choice, it is well known that for Higgs production an optimal choice would be $\mu \sim M_{\rm H}/2$ [96]. Theoretically, it is justified both by all-order analysis of the Hgg form factor and by the fact that the average $p_\perp$ of the Higgs boson is $\sim M_{\rm H}/2$. Empirically, a much better convergence is observed with this scale choice, as well as a reduced impact of resummation effects [89]. For off-shell studies, this translates into choosing as a central scale half of the virtuality of the Higgs boson, i.e.

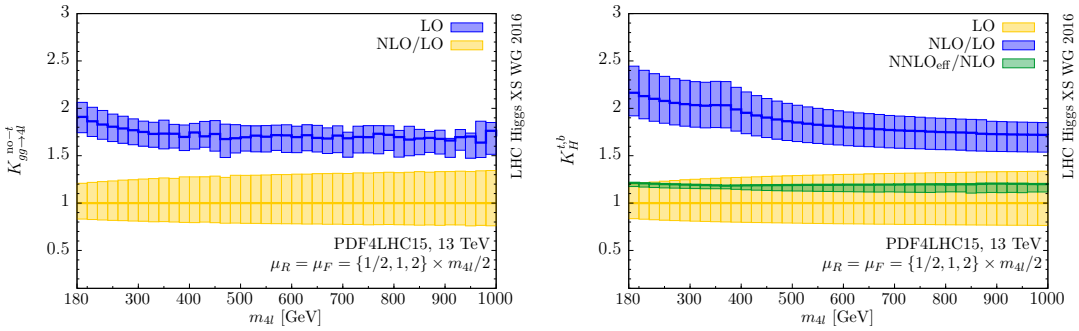

Figure 153: Left: NLO K-factor for $gg \to 4l$ background, massless quark contribution. Right: K-factor for $gg \to H \to 4l$ signal. NLO with full mass dependence, NNLO in the HEFT approximation. See text for details.

$\mu = m_{4l}/2$. Since most of the above consideration are only based on the color flow of the process, they also apply for the background and interference scale choice. Incidentally, we note that this was also the preferred choice for the NNLO $pp \to WW/ZZ$ computations [562, 563].

In the region $m_{4l} < 2m_t$, precise results exist for both the signal and the background. In more detail, NNLO results for the signal can be obtained from [100, 102]. For the background, NLO contributions from massless quarks can be obtained using [523][I.52] while top quark contributions can be obtained from [533]. In principle, these results could be used to obtain a NLO prediction for the interference. However, this calculation has not been performed yet. Given the similarity of signal and background $K-$factors, until a better computation is available the interference $K-$ factor can be obtained as the geometric average of the signal and background $K-$ factors. Scale variation uncertainties should account for missing higher order in the perturbative expansion. Alternatively, we note that even with our scale choice the signal still exhibits a non negligible NNLO $K-$factor, and it is not unreasonable to expect a similar $K-$factor also for the background [569]. One may then apply the signal NNLO $K-$factor to the background as well, and take the difference between NNLO and NLO as a conservative estimate of perturbative uncertainties.

In the high invariant mass region $m_{4l} > 2m_t$, it is not possible at this stage to provide a full NNLO (NLO) theoretical prediction for the signal (background), since exact heavy quark mass effects at NLO are unknown. In the following, we investigate signal and background $K-$factors in this region making different assumptions for missing top quark contributions. First, we compare in Figure 153 results for signal – with full top and bottom mass dependence through NLO – and background neglecting top quark contributions, as described in the previous sections and in [523]. For reference, we also show the effect of NNLO QCD corrections (computed with NNLO PDFs and α_s, and in the heavy-top approximation). This figure shows that signal and background K-factors are similar throughout the whole invariant mass spectrum considered here.

To quantify the effect of the missing top quark contribution in the background, we study two extreme approaches. First, we assume that the $K-$factor for massive and massless contributions is identical. Given their similarity in the low-mass region, we believe this assumptions to be reasonable. This leads to the K-factor shown in Figure 153 (see also Eq. I.8.12)

$$K_{gg\to 4l} = \frac{\mathrm{d}\sigma_{t,b}^{\mathrm{LO}}/\mathrm{d}m_{4l} + \mathcal{R}_{t,b}^{\mathrm{LO}}\,\mathrm{d}\Delta\sigma_{\mathrm{no}-t}^{\mathrm{NLO}}/\mathrm{d}m_{4l}}{\mathrm{d}\sigma_{t,b}^{\mathrm{LO}}/\mathrm{d}m_{4l}} = \frac{\mathrm{d}\sigma_{\mathrm{no}-t}^{\mathrm{LO}}/\mathrm{d}m_{4l} + \mathrm{d}\Delta\sigma_{\mathrm{no}-t}^{\mathrm{NLO}}/\mathrm{d}m_{4l}}{\mathrm{d}\sigma_{\mathrm{no}-t}^{\mathrm{LO}}/\mathrm{d}m_{4l}} = K_{gg\to 4l}^{\mathrm{no}-t}. \tag{I.8.13}$$

Second, we use full mass dependence in the LO contribution and only add NLO corrections for massless quarks[I.53]

[I.52] A numerical code for background predictions should be made public soon.

[I.53] Note that this second approach is rather unrealistic, as it assumes no interference between LO massive amplitudes and

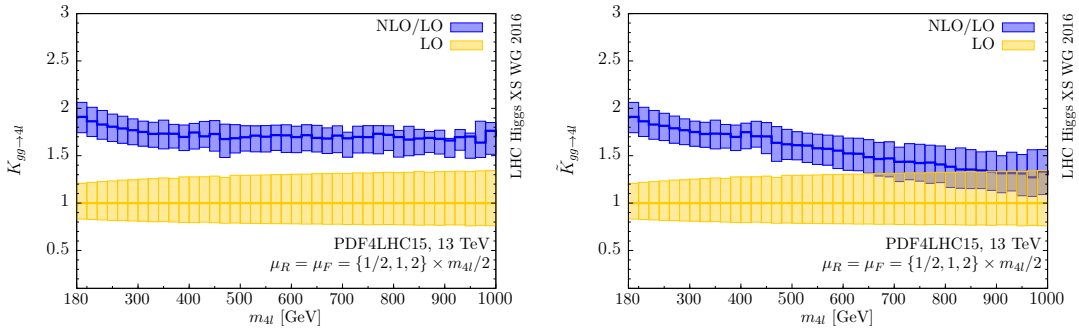

Figure 154: Comparison of different ways of treating quark mass effects at higher orders. Left: assume identical correction to massive and massless contributions. Right: assume zero corrections for massive contributions. See text for details.

$$\tilde{K}_{gg\to 4l} = \frac{\mathrm{d}\sigma^{\mathrm{LO}}_{t,b}/\mathrm{d}m_{4l} + \mathrm{d}\Delta\sigma^{\mathrm{NLO}}_{\mathrm{no}-t}/\mathrm{d}m_{4l}}{\mathrm{d}\sigma^{\mathrm{LO}}_{t,b}/\mathrm{d}m_{4l}}. \tag{I.8.14}$$

A comparison between K Eq. I.8.13 and $\tilde{K}$ Eq. I.8.14 is shown in Figure 154. Up to invariant masses $m_{4l} \sim 500$ GeV the two results are in good agreement, while they differ significantly at higher mass. The spread of these two results is a way to probe the uncertainty due to unknown mass effects.

Summarizing, for background predictions in the high invariant mass region we suggest to use exact LO multiplied by the massless K-factor Eq. I.8.13. The spread shown in Figure 154 may be used as a way to estimate the uncertainty of this procedure until a better computation becomes available. As for low invariant mass region, the interference K-factor is then determined as geometric mean of signal and background K-factors. Alternatively, given the similarity of signal and background $K-$factors and the size of uncertainties a simpler alternative – until more precise theoretical predictions are available – would be to assume the same K-factor for signal and background, and assign to it a systematic uncertainty which covers the effects described above. Note that both these approaches lead to a smooth interference $K-$factor over the whole m_{4l} spectrum, with an uncertainty increasing at large invariant masses to reflect the effect of unknown top quark mass effects. While this report was finalised, Refs. [570, 571] appeared. The results for the NLO corrections to the signal-background interference presented there support the approach advocated in this section.

I.8.5 $H \to \gamma\gamma$ mode

In this Section we will review the status of the theoretical and experimental treatments of the interference term between the $gg \to H \to \gamma\gamma$ and $gg \to \gamma\gamma$.

The natural width of the Higgs boson is an important physics property that could reveal new physics in case of disagreement between the prediction and the measured values. Direct measurements of the Higgs widths are not possible, as the experimental mass resolution is significantly larger than the expected width. The mass resolution of the $\gamma\gamma$ system is about 1.7 GeV for $m_{\gamma\gamma} = 125$ GeV, 400 times larger than the natural width. Measurements of coupling strengths paired with limits on the invisible branching fraction indirectly constrain the width to close to its SM value [572], but this strategy cannot take into account unobserved (but not truly invisible) decay modes.

A new method as introduced by Dixon, Li, and Martin [505, 506], allows to extract an indirect limit on the Higgs width using the interference of the $H \to \gamma\gamma$ signal with respect to the continuum diphoton background ($gg \to \gamma\gamma$ box diagrams). This interference has two parts.

NLO massless ones. We consider it here only as a way to estimate possible top quark effects in a conservative way.

1. An imaginary component reduces the total signal yield by $2-3\%$. Because this effect is degenerate with the coupling (signal strength) measurements, it is only measurable using constraints on the production rates from other channels.
2. The real component is odd around the Higgs boson mass and does not change the yield. However, when folded with the experimental resolution, it engenders a negative shift in the apparent mass.

In the SM, this shift was originally estimated using a simplified resolution model to be approximately 80 MeV [506], and for a width 20 times larger than the SM value, the shift was estimated to approximately 400 MeV.

In this section, we will review the latest developments on theoretical calculations, available MC tools, as well as experimental analyses from ATLAS and CMS collaborations.

I.8.5.1 Theory overview

The Higgs boson is dominantly produced by gluon fusion through a top quark loop. Its decay to two photons, $H \to \gamma\gamma$, provides a very clean signature for probing Higgs properties, including its mass. However, there is also a large continuum background to its detection in this channel. It is important to study how much the coherent interference between the Higgs signal and the background could affect distributions in diphoton observables, and possibly use it to constrain Higgs properties.

The interference of the resonant process $ij \to X + H(\to \gamma\gamma)$ with the continuum QCD background $ij \to X + \gamma\gamma$ induced by quark loops can be expressed at the level of the partonic cross section as:

$$\begin{aligned} \delta\hat{\sigma}_{ij\to X+H\to\gamma\gamma} &= -2(\hat{s}-m_H^2)\,\frac{\mathrm{Re}\left(\mathcal{A}_{ij\to X+H}\mathcal{A}_{H\to\gamma\gamma}\mathcal{A}^*_{\mathrm{cont}}\right)}{\left(\hat{s}-m_H^2\right)^2+m_H^2\Gamma_H^2} \\ &\quad -2m_H\Gamma_H\,\frac{\mathrm{Im}\left(\mathcal{A}_{ij\to X+H}\mathcal{A}_{H\to\gamma\gamma}\mathcal{A}^*_{\mathrm{cont}}\right)}{\left(\hat{s}-m_H^2\right)^2+m_H^2\Gamma_H^2}\,, \end{aligned} \tag{I.8.15}$$

where m_H and Γ_H are the Higgs mass and decay width, and $\hat{s}$ is the partonic invariant mass. The interference is written in two parts, proportional to the real and imaginary parts of the Higgs Breit-Wigner propagator respectively, to which will be referred to as the real and imaginary part of the interference from now on.

The real part interference is odd in $\hat{s}$ around the Higgs mass peak, and thus its effect on the total $\gamma\gamma$ rate is subdominant as pointed out in ref. [573, 574]. The imaginary part of the interference, depending on the phase difference between the signal and background amplitudes, could significantly affect the total cross section. However, for the gluon-gluon partonic subprocess, it was found that the loop-induced background continuum amplitude has a quark mass suppression in its imaginary part for the relevant helicity combinations, making it dominantly real, therefore bearing the same phase as the Higgs production and decay amplitudes [574]. As a result, the contribution of the interference to the total cross section in the gluon fusion channel is highly suppressed at leading order (LO). The main contribution of the interference to the total rate comes from the two-loop imaginary part of the continuum amplitude $gg \to \gamma\gamma$, and only amounts to around 3% of the total signal rate [573].

Later, in ref. [505] it was shown that even though the real part of the interference hardly contributes to the total cross section, it has a quantifiable effect on the position of the diphoton invariant mass peak, producing a shift of $\mathcal{O}(100\,\mathrm{MeV})$ towards a lower mass region, once the smearing effect of the detector was taken into account. In ref. [575], the qg and $q\bar{q}$ channels of this process were studied, completing the full $\mathcal{O}(\alpha_S^2)$ computation of the interference effects between the Higgs diphoton signal and the continuum background at the LHC. Note that the extra qg and $q\bar{q}$ channels involve one QCD emission in the final states, but the corresponding background amplitudes start at tree level, and therefore the relevant interference is of the same order as the LO gg channel in which the background amplitude is

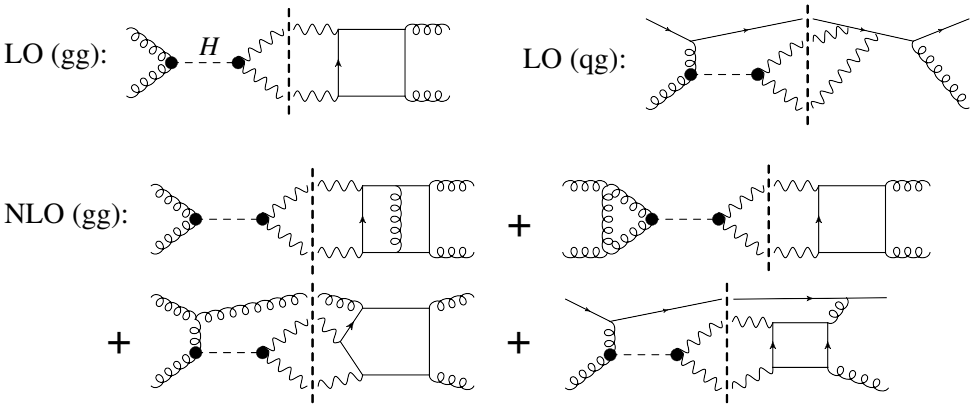

Figure 155: Representative diagrams for interference between the Higgs resonance and the continuum in the diphoton channel. The dashed vertical lines separate the resonant amplitudes from the continuum ones.

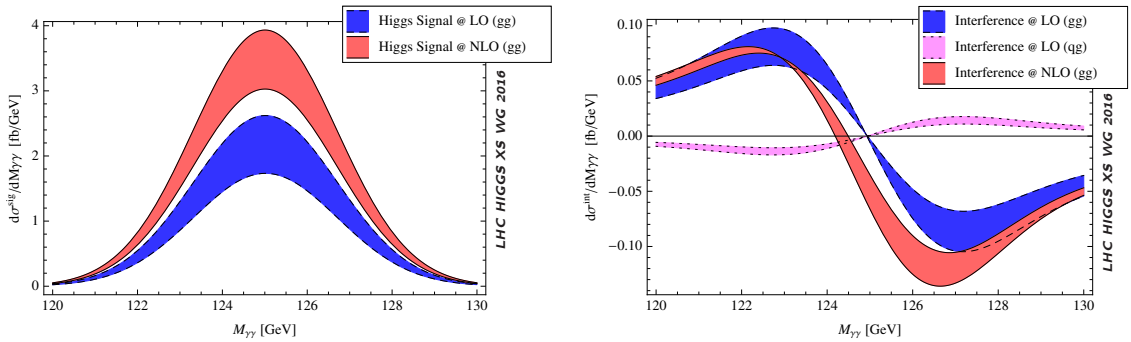

Figure 156: Diphoton invariant mass $M_{\gamma\gamma}$ distribution for pure signal (left panel) and interference term (right panel) after Gaussian smearing.

induced by a quark loop. The extra LO qg interference is depicted by the top right diagram in Figure 155, and the $q\bar{q}$ channel is related by cross symmetry. It was found that the contribution from the $q\bar{q}$ channel is numerically negligible due to the quark PDF suppression.

More recently, the dominant next-to-leading order (NLO) QCD corrections to the interference were calculated in ref. [506], where the dependence of the mass shift on the acceptance cuts was also studied. The left panel of Figure 156 shows the Gaussian-smeared diphoton invariant mass distribution for the pure signal at both LO and NLO in QCD. Standard acceptance cuts were applied to the photon transverse momenta, $p_{T,\gamma}^{\text{hard/soft}} > 40/30$ GeV, and rapidities, $|\eta_\gamma| < 2.5$. In addition, events were discarded when a jet with $p_{T,j} > 3$ GeV was within $\Delta R_{\gamma j} < 0.4$ of a photon. The scale uncertainty bands were obtained by varying $m_H/2 < \mu_F, \mu_R < 2m_H$ independently. For NLO, an additional qg process was included, where the background is induced by a quark loop as shown in the bottom right diagram of Figure 155; this is required as part of NLO gg channel to cancel the quark to gluon splitting in PDF evolution and reduces dependence on the factorization scale μ_F. As a result, the scale uncertainty bands come mostly from varying the renormalization scale μ_R.

The right panel of Figure 156 shows the corresponding Gaussian-smeared interference contributions. Each band is labelled according to Figure 155. The destructive interference from the imaginary part shows up at two-loop order in the gluon channel in the zero mass limit of light quarks [573]. It produces the offset of the NLO gg curve from zero at $M_{\gamma\gamma} = 125$ GeV.

Figure 157 shows the study of the mass shift dependence on a lower cut on the Higgs transverse momentum $p_T > p_{T,H}$. This strong dependence could potentially be observed experimentally, completely within the $\gamma\gamma$ channel, without having to compare against a mass measurement using the only

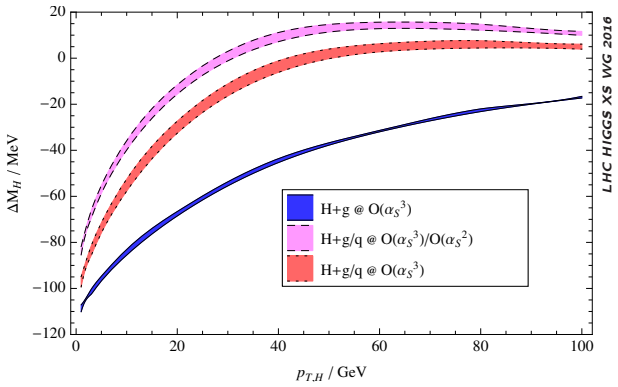

Figure 157: Apparent mass shift for the SM Higgs boson versus the lower cut on the Higgs transverse momentum, $p_T > p_{T,H}$.

other high-precision channel, ZZ^*[I.54]. Using only $\gamma\gamma$ events might lead to reduced experimental systematics associated with the absolute photon energy scale. The $p_{T,H}$ dependence of the mass shift was first studied in ref. [576]. The dotted red band includes, in addition, the continuum process $qg \to \gamma\gamma q$ at one loop via a light quark loop, a part of the full $\mathcal{O}(\alpha_s^3)$ correction as explained above. This new contribution partially cancels against the tree-level qg channel, leading to a larger negative Higgs mass shift. The scale variation of the mass shift at finite $p_{T,H}$ is very small, because it is essentially a LO analysis; the scale variation largely cancels in the ratio between interference and signal that enters the mass shift.

Due to large logarithms, the small $p_{T,H}$ portion of Figure 157 is less reliable than the large $p_{T,H}$ portion. In using the $p_{T,H}$ dependence of the mass shift to constrain the Higgs width, the theoretical accuracy will benefit from using a wide first bin in p_T. One could take the difference between apparent Higgs masses for $\gamma\gamma$ events in two bins, those having p_T above and below, say, 40 GeV.

The Higgs width in the SM is $\Gamma_{H,\mathrm{SM}} = 4.07$ MeV, far too narrow to observe directly at the LHC. In global analyses of various Higgs decay channels [577–579], it is impossible to decouple the Higgs width from the couplings in experimental measurements without a further assumption, because the Higgs signal strength is always given by the product of squared couplings for Higgs production and for decay, divided by the Higgs total width Γ_H. Typically, the further assumption is that the Higgs coupling to electroweak vector bosons does not exceed the SM value. However, as was also pointed out in ref. [506], the apparent mass shift could be used to bound the value of the Higgs width. This is because the interference effect has different dependence on the Higgs width, allowing Γ_H to be constrained independently of assumptions about couplings or new decay modes in a lineshape model. Such a measurement would complement more direct measurements of the Higgs width at future colliders such as the ILC [580, 581] or a muon collider [582, 583], but could be accomplished much earlier.

Using $\mu_{\gamma\gamma}$ to denote the ratio of the experimental signal strength in $gg \to H \to \gamma\gamma$ to the SM prediction ($\sigma/\sigma^{\mathrm{SM}}$), the following equation can be set up,

$$\frac{c_{g\gamma}^2 S}{m_H \Gamma_H} + c_{g\gamma} I = \left(\frac{S}{m_H \Gamma_{H,\mathrm{SM}}} + I \right) \mu_{\gamma\gamma} \,, \tag{I.8.16}$$

where $c_{g\gamma} = c_g c_\gamma$ is the rescaling factor to be solved to preserve the signal yield when the Higgs width is varied. Once the relation between the $c_{g\gamma}$ and the Higgs width Γ_H is obtained, it can be used to determine the size of the apparent mass shift as a function of Γ_H. Neglecting the interference contribution I to the total rate, and assuming $\mu_{\gamma\gamma} = 1$, the mass shift was found to be proportional to the square root of the Higgs width, $\delta m_H \propto \sqrt{\Gamma_H/\Gamma_{H,\mathrm{SM}}}$, given that the width is much less than the detector resolution.

[I.54] The mass shift for ZZ^* is much smaller than for $\gamma\gamma$, as can be inferred from Figure 17 of ref. [495], because $H \to ZZ^*$ is a tree-level decay, while the continuum background $gg \to ZZ^*$ arises at one loop, the same order as $gg \to \gamma\gamma$.

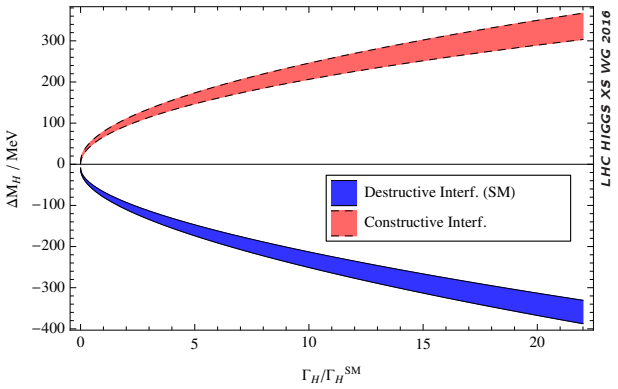

Figure 158: Higgs mass shift as a function of the Higgs width. The coupling $c_{g\gamma}$ has been adjusted to maintain a constant signal strength, in this case $\mu_{\gamma\gamma} = 1$.

Figure 158 plots the mass shift with $\mu_{\gamma\gamma} = 1$ and a smearing Gaussian width of 1.7 GeV. It is indeed proportional to $\sqrt{\Gamma_H}$ up to small corrections. If new physics somehow reverses the sign of the Higgs diphoton amplitude, the interference I would be constructive and the mass shift would become positive.

In ref. [584] it was proposed to use another $\gamma\gamma$ sample to determine the Higgs resonance peak, in which the two photons were produced in association with two jets. Although this process is relatively rare, so is the background, making it possible to obtain reasonable statistical uncertainties on the position of the mass peak in this channel despite the lower number of events. The production of a Higgs in association with two jets is characteristic of the Vector Boson Fusion (VBF) production mechanism. While, in general terms, VBF is subdominant with respect to GF, it has a very different kinematical signature and can be selected through an appropriate choice of the experimental cuts. From a theoretical point of view, the VBF production mechanism has the additional advantage that perturbative corrections are much smaller than for GF (see e.g. ref. [259]). The effect of the signal-background interference for both the GF and VBF production mechanisms were studied, and the relevant diagrams are given in Figure 159. There are two kinds of backgrounds amplitudes, each of QCD and EW origin. It turns out that the interferences between GF signal and EW background or VBF signal and QCD background are highly suppressed by QCD color factors, and therefore only the remaining combinations are shown in the first two diagrams of Figure 159. In addition, the interference with loop-induced QCD background, as given in the third diagram of Figure 159, was also considered, since it is enhanced by large gluonic luminosity at the LHC.

In Figure 160 the values of the apparent mass shift δm_H obtained for different cuts on the difference in pseudorapidities between the jets $|\Delta\eta_{jj}|$ are shown. The contributions from VBF and GF are presented separately, as well as the total shift. At the bottom of the plot, the total integrated signal is shown, also separated into VBF and GF contributions for the same cuts. For this plot no cut in $p_{T,H}$ was applied, and only events with the invariant mass of the dijet system $M_{jj} > 400$ GeV were considered. When no cut in $|\Delta\eta_{jj}|$ is applied, the shift in the Higgs invariant mass peak position produced by these two main production mechanisms is of the same magnitude, but of opposite sign; hence one observes a partial cancellation between them, with a net shift of around -6 MeV. As the value of $|\Delta\eta_{jj}|_{\text{min}}$ is increased, VBF becomes the dominant contribution, and GF becomes negligible, leading to a shift of around 20 MeV toward lower masses.

Next, the dependence of the mass shift on $p_{T,H}^{\text{min}}$ was studied. In Figure 161 the mass shift and the signal cross section for a range of $p_{T,H}^{\text{min}}$ between 0 GeV and 160 GeV is presented. The curves are labelled in the same way as in Figure 160. Once again, both production mechanisms contribute to the shift in invariant mass with opposite signs. For this plot, additional cuts in $M_{jj} > 400$ GeV and $|\Delta\eta_{jj}| > 2.8$ were applied, enhancing in this way the VBF contributions. However, at higher $p_{T,H}^{\text{min}}$, GF

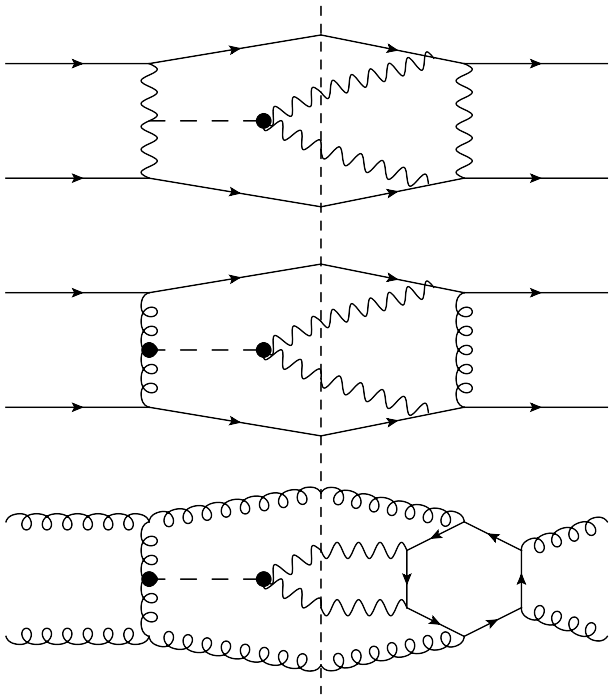

Figure 159: Examples of the Feynman diagrams computed for the calculation. The vertical dotted line separates signal from background. Above, the VBF signal and EW background con- tributions; in the middle the GF signal with tree level QCD mediated background; below, gluon-initiated signal, with the corresponding loop-induced LO background.

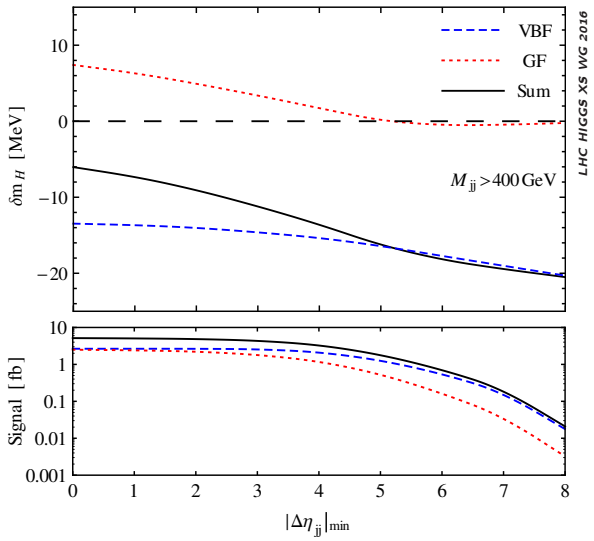

Figure 160: Top: Plot of mass shift δm_H for different values of $|\Delta\eta_{jj}|_{\min}$. The dashed blue line represents the contribution from the VBF mechanism alone, the dotted red line shows GF only, and the solid black line displays the total shift of the Higgs invariant mass peak. Bottom: Total integrated signal cross section, also separated into VBF and GF contributions for the same cuts. No cut on $p_{T,H}^{\min}$ was applied, and an additional cut was set of $M_{jj} > 400$GeV.

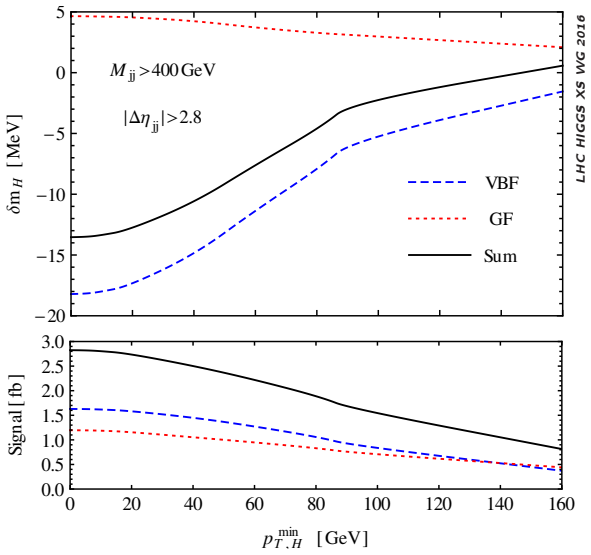

Figure 161: Top: Plot of mass shift δm_H for different values of $p_{T,H}^{\rm min}$ for VBF, GF and total contributions. The curves are labelled as in Figure 160. Bottom: Total integrated signal, also separated into VBF and GF contributions for the same cuts. The following additional cuts were applied: $M_{jj} > 400$ GeV and $|\Delta\eta_{jj}| > 2.8$.

becomes as important as VBF.

As has already been mentioned, the shift in the Higgs invariant mass peak in $pp \to H(\to \gamma\gamma) + 2\,\text{jets} + X$ is considerably smaller than in the inclusive channel $pp \to H(\to \gamma\gamma) + X$. For appropriate cuts it can be almost zero. This makes it useful as a reference mass for experimental measurement of the mass difference,

$$\Delta m_H^{\gamma\gamma} \equiv \delta m_H^{\gamma\gamma,\,\text{incl}} - \delta m_H^{\gamma\gamma,\,\text{VBF}}\,, \tag{I.8.17}$$

where $\delta m_H^{\gamma\gamma,\,\text{incl}}$ is the mass shift in the inclusive channel, as computed at NLO in ref. [506], and $\delta m_H^{\gamma\gamma,\,\text{VBF}}$ is the quantity computed in ref. [584]. In computing $\delta m_H^{\gamma\gamma,\,\text{VBF}}$ for use in eq. (I.8.17) the basic photon and jet p_T and η cuts were imposed, and also $M_{jj} > 400$ GeV, but no additional cuts on $p_{T,H}$ or $\Delta\eta_{jj}$ were applied. This choice of cuts results in a small reference mass shift and a relatively large rate with which to measure it.

The lineshape model of ref. [506], as introduced earlier for the $gg \to \gamma\gamma$ inclusive process, was used in ref. [584] to compute the mass shift for the VBF process. It is in a way relatively independent of the new physics that may increase Γ_H from the SM value. The couplings of the Higgs boson to other SM particles must be modified if the Higgs width is varied, in order to be consistent with the Higgs signal strength measurements already made by the LHC, and prevent the total cross section from suffering large variations. Here, the deviation from SM coupling is described by a rescaling factor $c_{V\gamma} = c_V c_\gamma$, similar to $c_{g\gamma}$ in the $\gamma\gamma$ inclusive case, which is adjusted for different values of Γ_H to maintain the Higgs signal strength near the SM value.

Figure 162 shows how the observable $\Delta m_H^{\gamma\gamma}$ depends on the value of the Higgs width. The dependence is proportional to $\sqrt{\Gamma_H/\Gamma_{H,\text{SM}}}$ to a very good accuracy, as dictated by the linearity of the produced shift in $c_{g\gamma}$ or $c_{V\gamma}$ (in the range shown). It is dominated by the mass shift for the inclusive sample [506]. As was stated before, the main theoretical assumption was that the couplings of the Higgs rescale by real factors, and the same rescaling for the Higgs coupling to gluons as for its coupling to vector boson pairs was assumed; this assumption could easily be relaxed, to the degree allowed by

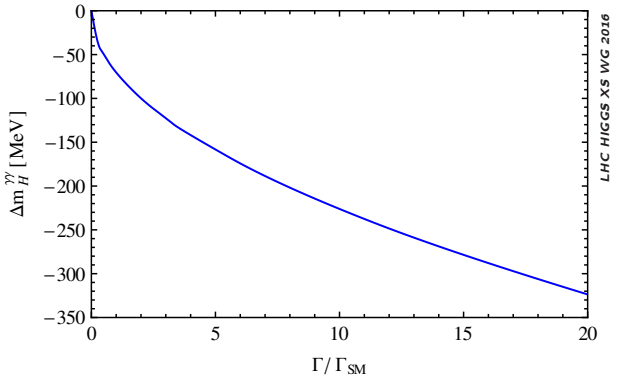

Figure 162: Plot of measurable mass shift $\Delta m_H^{\gamma\gamma}$ defined in eq. (I.8.17), as a function of $\Gamma_H/\Gamma_{H,\mathrm{SM}}$.

current measurements of the relative yields in different channels. The strong dependence the shift shows on the Higgs width might allow LHC experiments to measure or bound the width.

I.8.5.2 Monte Carlo interference implementations

An overview of the Monte Carlo tools available to describe the Higgs lineshape and the signal-background interference is presented in this Section. A first study using these tools is also presented.

I.8.5.2.1 Available Tools: Sherpa 2.2.0 with DIRE parton shower

The calculations of [506, 584] have been implemented in Sherpa 2.2.0. Parton showers have been used for more than three decades to predict the dynamics of multi-particle final states in collider experiments [585, 586]. Recently, a new model was proposed [587], which combines the careful treatment of collinear configurations in parton showers with the correct resummation of soft logarithms in color dipole cascades [588–591]. Following the basic ideas of the dipole formalism, the ordering variable is chosen as the transverse momentum in the soft limit. The evolution equations are based on the parton picture. Color-coherence is implemented by partial fractioning the soft eikonal following the approach in [245], and matching each term to the double logarithmically enhanced part of the DGLAP splitting functions. Enforcing the correct collinear anomalous dimensions then determines all splitting kernels to leading order.

I.8.5.2.2 Exercise with DIRE parton shower

This sensitivity study follows the basic search strategy exploited in the past by both the CMS and ATLAS experiments for what concerns the $H \to \gamma\gamma$ search [63, 592]. The study is performed only at generator level assuming only gluon fusion production mode (GGH). The parton shower model assumed is the one described in section I.8.5.2.1. Two isolated photons fulfilling loose identification criteria are selected and required to be within the the detector acceptance of $|\eta| < 2.5$ and the leading (subleading) photon must have $p_{T1} > 40$ GeV and $p_{T2} > 30$ GeV. The diphoton invariant mass distribution is constructed from these photons and required to be in the $[110 - 150]$ GeV energy range. Figures 163 and 164 show the transverse momentum distributions obtained for the two photons after the selection.

Figures 165 and 166 show the transverse momentum and the pure invariant mass of the diphoton system assuming no interference effect. Finally Figures 167 and 168 show the diphoton mass shapes for only the interference term and for the signal+interference cross–section. Interference effect is considered between the $H \to \gamma\gamma$ resonant process and the non resonant diphoton production. A convolution of the pure cross–section shape with a gaussian model can be applied to simulate the effects of the limited resolution of the detector in the photon energy measurement. Different values for the energy resolution

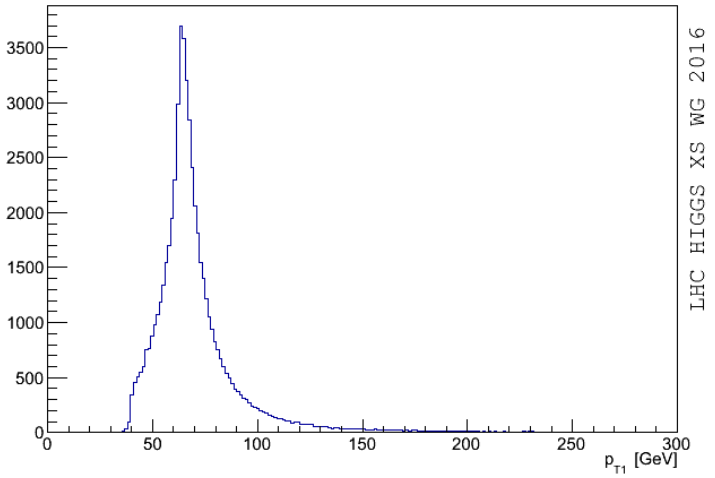

Figure 163: Transverse momentum distribution of the leading photon of the $H \to \gamma\gamma$ process produced via gluon fusion.

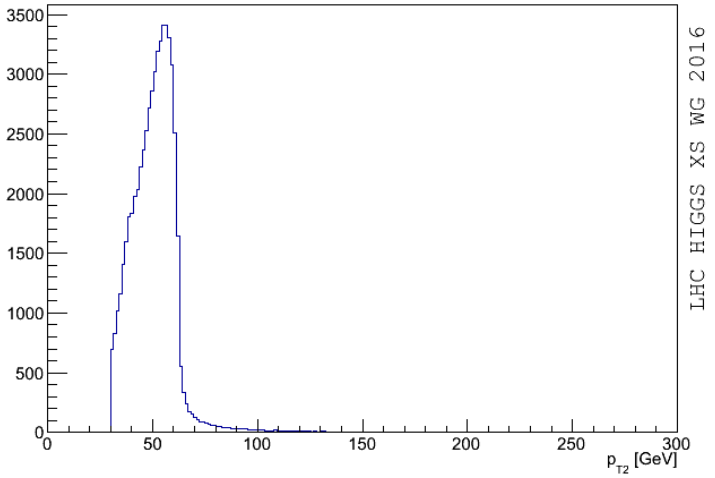

Figure 164: Transverse momentum distribution of the subleading photon of the $H \to \gamma\gamma$ process produced via gluon fusion.

(the σ of the gaussian function) can be assumed to fold the generator shape. Figure 169 shows the effect of the resolution smearing on the interference term assuming resolution values in the range [1.2-2.2] GeV. A realistic energy resolution value of 1.7 GeV is eventually assumed before comparing the shapes of the pure signal term and of the signal + interference terms in order to evaluate the relative shift introduced by the interference term itself. Figures 170 and 171 show this effect. In this case the shift is evaluated by fitting the two distributions with a gaussian function and taking the difference of the fitted mean values of the two models. The inclusive shift obtained is equal to $\Delta m = -89$ MeV. The trend of this shift varying the assumption on the value of the energy resolution is also shown in Figure 172. The uncertainties associated to the shifts come only from the statistical propagation of the errors on the fit parameters. As outlined in section I.8.5.1 the effect of the shift depends strongly upon the minimum threshold applied on the transverse momentum of the diphoton system. Figure 173 reproduces the results shown in section I.8.5.1 showing that the greater the requirement on the minimum value of the diphoton momentum, the smaller the shift in the mass peak position. Additional studies are ongoing in order to

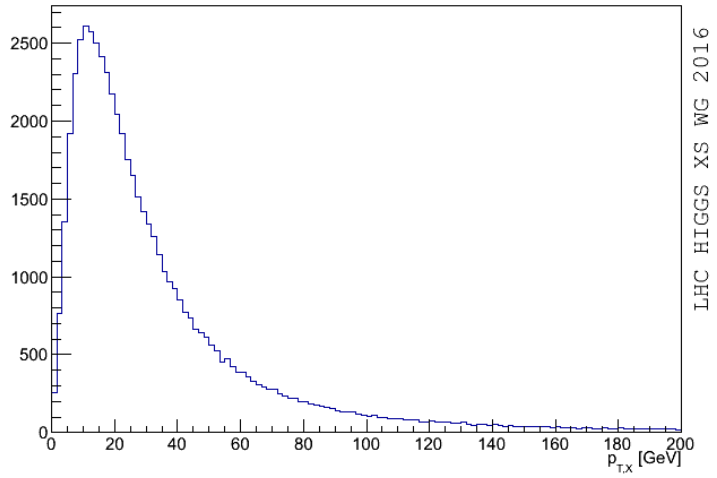

Figure 165: Diphoton transverse momentum distribution for pure $H \to \gamma\gamma$ signal produced via gluon fusion.

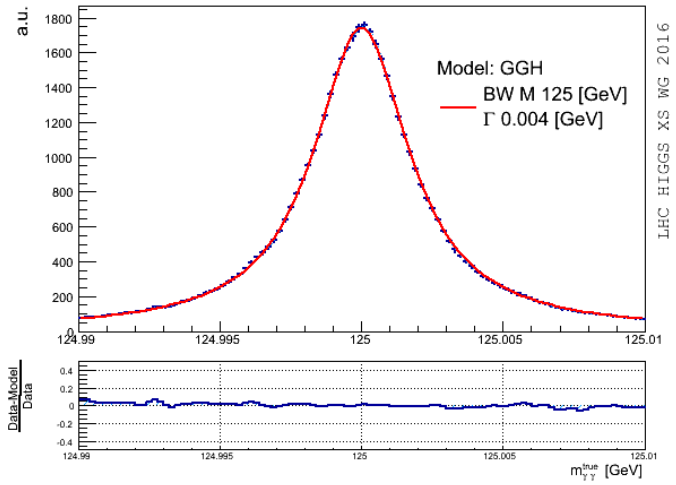

Figure 166: Diphoton invariant mass distribution for pure $H \to \gamma\gamma$ signal produced via gluon fusion.

evaluate the dependence of the shift upon the natural width of the Higgs.

I.8.5.3 Studies from ATLAS

This sections documents the studies by the ATLAS collaboration [I.55].

I.8.5.3.1 Interference impact on the Higgs boson mass

A recent study has been conducted by ATLAS [593] to give a realistic estimate of the impact of the interference term on the Higgs mass measured in the $h \to \gamma\gamma$ channel [594]. Sherpa 2.0 is used to generate the $gg \to H \to \gamma\gamma$ signal samples as well as samples corresponding to the interference between this signal and its irreducible background, which is achieved using weigthed events. The invariant mass spectrum of the di-photon system produced by these samples may be seen in Figure 174 for a specific category used in the ATLAS mass measurement. This generation has been done for a Higgs mass of $m_H = 125$ GeV

[I.55] Contact: C. Becot, F. Bernlochner, L. Fayard, S. Yuen

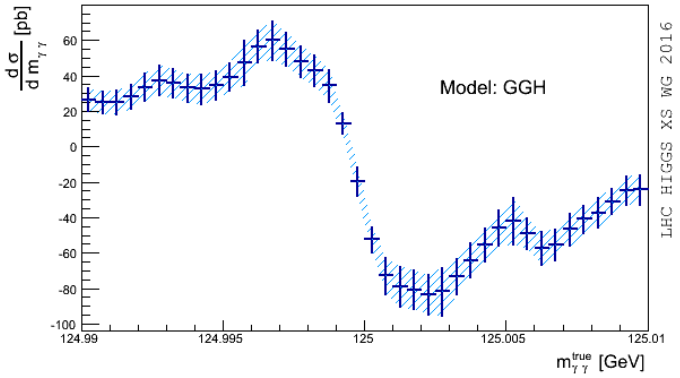

Figure 167: Pure interference term of the diphoton production cross–section.

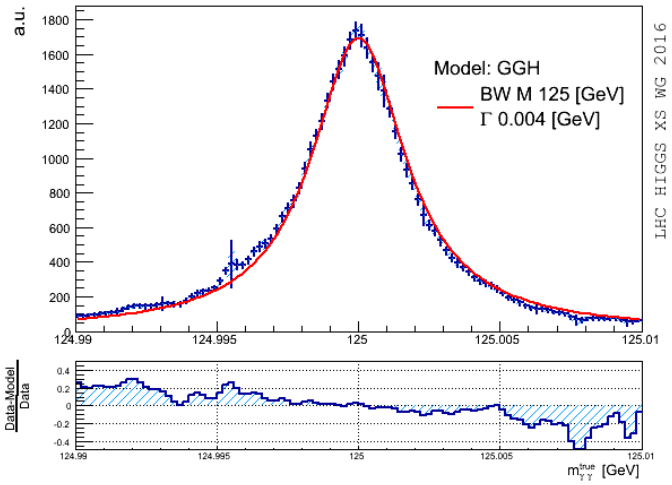

Figure 168: Total cross–section (signal+interference terms) distribution of the diphoton production. Signal refers to the $H \to \gamma\gamma$ process produced via gluon fusion.

and a Higgs width of $\Gamma_H = 4$ MeV. The NLO computation implemented in Sherpa 2 is matched to the CSS parton shower [351], which accounts for additional QCD radiations in the initial state. In order to give the best description of the interference and signal p_T spectra the behaviour of the shower has been tuned so that the Higgs signal p_T distribution generated by Sherpa matches the one generated by HRes 2.0 [219] as well as possible. This has been done by modifying the shower parameter CSS_IS_AS_FAC which modifies the energy at which the strong coupling constant is evaluated during the parton-shower evolution. The best agreement between the two distributions is obtained for CSS_IS_AS_FAC = 1.5. This tuning is also applied for the generation of the interference term. After generation, the di-photon mass is smeared according to the signal model derived in [594] which is dominated by a Crystal-Ball component. In order to reproduce the experimental efficiencies, the Monte-Carlo weights are folded by multiplicative weights that have the values of these efficiencies.

The background is determined from a fit to data, as is usually done is the construction of the 'Asimov' dataset [595] and is therefore not subject to consideration on the physics modelling. In order

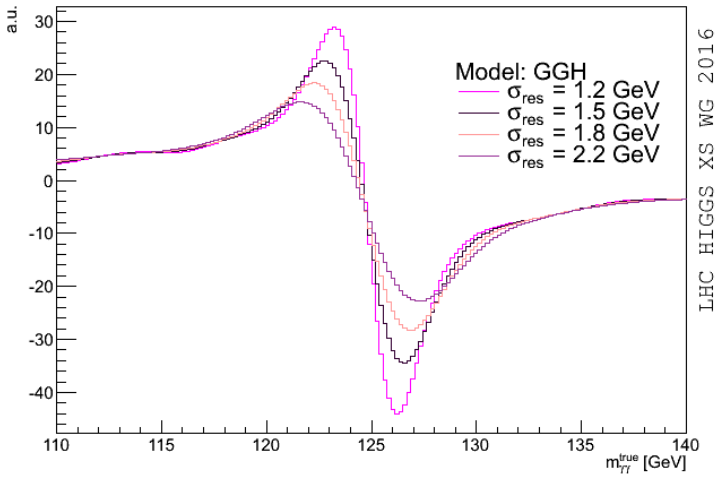

Figure 169: Interference cross–section term smeared assuming different values for the energy resolution in the range [1.2-2.2] GeV.

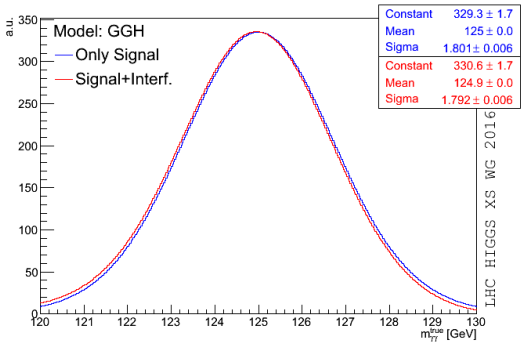

Figure 170: Pure signal and signal + interference shapes after applying a gaussian energy smearing of 1.7 GeV to simulate detector resolution effects. Red distribution corresponds to the pure $H \to \gamma\gamma$ process while the blue distribution includes the interference effect. Cross–section distributions are fitted with a gaussian function. Results of the fit are shown on the plot with the corresponding colors.

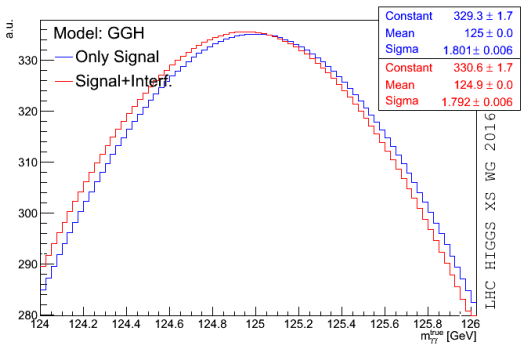

Figure 171: This figure shows the same results of Figure 170 with a zoom around the peak region, applied to better visualize the shift introduced by the interference effect. The inclusive shift obtained is equal to $\Delta m = -89$ MeV.

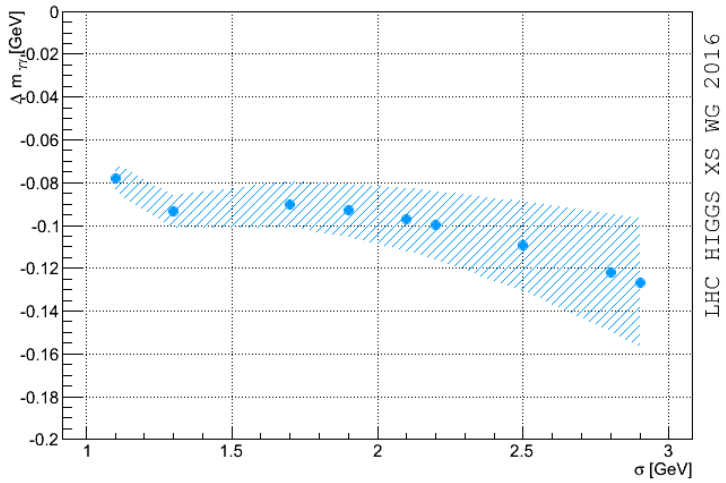

Figure 172: Shift in the mass peak position as a function of the energy mass resolution assumed. The smearing resolution being fixed, both the signal only and the signal+interference cross–section distributions are fitted with a gaussian function. The smearing is evaluated by the difference of the mean values for the two gaussian functions. The uncertainties associated with the shifts comes only from the statistical propagation of the errors on the fit parameters.

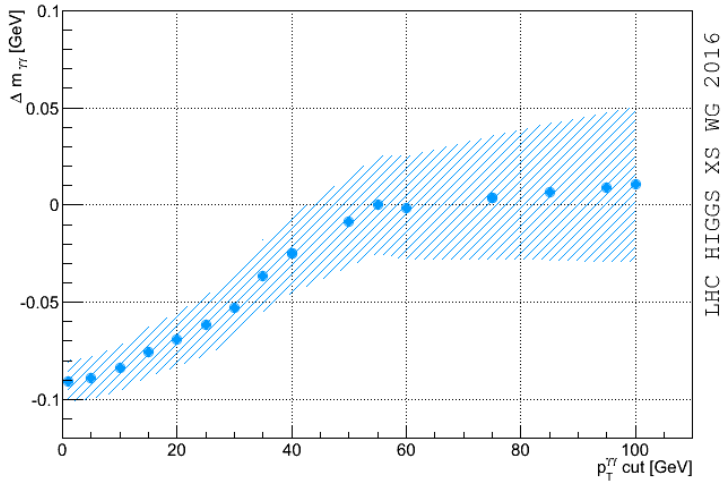

Figure 173: Shift in the mass peak position as a function of the minimum requirement on the diphoton transverse momentum. The smearing resolution being fixed, both the signal only and the signal+interference cross–section distributions are fitted with a gaussian function. The smearing is evaluated by the difference of the mean values for the two gaussian functions. The uncertainties associated to the shifts comes only from the statistical propagation of the errors on the fit parameters.

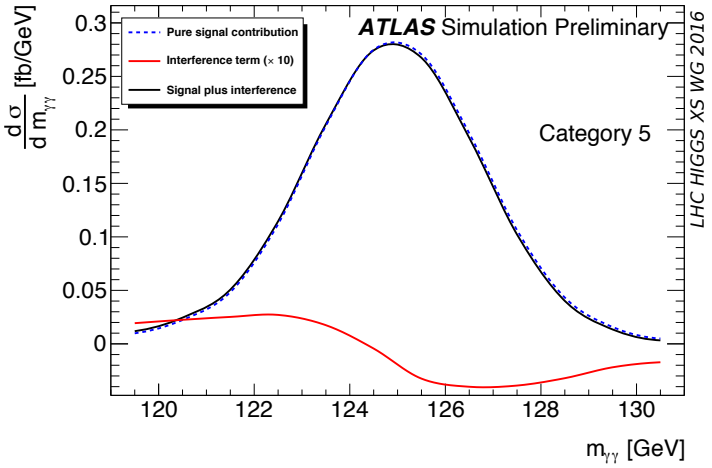

Figure 174: Mass distribution generated by the signal and interference term, as well as their sum, for a specific category of the ATLAS mass measurement (category no. 5). For illustrative purpose the magnitude of the interference-only term has been multiplied by 10.

to improve the analysis performances the mass measurement is carried out in event categories that are afterwards combined [594], and the actual shape used for this fit of the background depends on the actual category of events and are the same than those used in [594]. The additional production mechanisms with associated objects (vector-boson fusion, Higgsstrahlung and $t\bar{t}H$) are added by a re-scaling of the cross-section of the signal samples. As they have kinematical properties that differ from the main gluon-fusion production mechanism (and especially a different p_T spectrum), the templates determined in each category are rescaled separately using the fraction of gluon-fusion events of this particular category.

Two 'Asimov' datasets are then determined: one that contains only the signal and background templates, and another one that contains the same contributions plus the interference template. Each of these datasets contains one template for each of the ten categories used in [594]. The best-estimate of the Higgs mass is obtained separately on each of these datasets with a maximum-likelihood fit that uses the statistical model derived in [594], which is based on the signal and background models described above. The Higgs mass shift is then estimated as the signed difference between the two dataset $\Delta m_H = m_H^{S+B+I} - m_H^{S+B}$ and has been estimated to be of $\Delta m_H = -35$ MeV.

In order to assess that the Monte-Carlo samples are sufficiently large to give a negligible statistical uncertainty on Δm_H, four equivalent signal and interference samples have been generated with different random seeds. The mass shift has been determined separately on each of these, giving a variance of less than 1 MeV. The imperfect closure of the estimate of the mass on the signal-plus-background only sample has been added as a systematic uncertainty. The choice the actual background shape used has also been considered and added as an uncertainty. Both of these systematic uncertainties are at the level of 3 MeV.

Theoretical uncertainties have been estimated by varying the signal and background K-factors as well as the QCD scales involved in this problem. For the main result the signal K-factor K_S was set to $K_S = 1.45$, which effectively rescales the signal prediction from Sherpa to the NNLO+NNLL signal cross-section. This factor has been varied by ± 0.1, which accounts for PDF and α_S uncertainties. Ideally the background K-factor K_B would rescale the background cross-section to the same order than the signal (NNLO), however no computation of the $gg \to \gamma\gamma$ background have been performed beyond NLO so far. A conservative uncertainty on k_B has been assessed by varying it from 1 to K_S, using $K_B = K_S$ as a central value. These two factors modify the interference template by rescaling it by a factor $\sqrt{K_S K_B}$. At the end the uncertainty due to the K-factors has been taken has the biggest enveloppe of all

these variations and gave an error of the mass-shift of ± 7 MeV. The three QCD scales (renormalization, factorization and resummation) have been varied, first separately then all at the same time. In spite of having a sizeable impact on the p_T spectrum, the resummation scale has almost no impact on the overall mass-shift estimated from the combined fit to ten categories, as most of the statistical power of this measurement is carried out by low p_T categories on which this scale does not have a big impact. The renormalization and factorization scales are varied by a factor 2, the central value being set to $m_{\gamma\gamma}$. Although the factorization scale has the dominant effect, the scale uncertainty is estimated as the variation that gives the biggest effect, which happens when the three scales are varied at once and gives an uncertainty of ± 5 MeV on the mass-shift.

All these four uncertainties are summed quadratically, which gives an estimate of the mass-shift of $\Delta m_H = -35 \pm 9$ MeV. This is valid only for the mass measurement carried out by ATLAS in the $h \to \gamma\gamma$ channel.

An illustration of the dependence of this shift on the analysis details is provided in [593], where an equivalent number is provided for an 'inclusive' analysis where the events are not split into categories. In this case the shift is estimated to be of $\Delta m_H = -49$ MeV, which is sizeably larger than in the actual measurement combining the ten different categories because of the different resolution. Moreover as the associated production components do not suffer from such large interference effects, their relative weights in the different categories may also give big variations of the actual mass-shift. For instance, it was estimated in [593] that for the inclusive fit and with the associated production removed the mass-shift would be of $\Delta m_H = -54$ MeV. It was also noted in [506] that the mass-shift had a linear dependence on the invariant mass resolution of the detector.

I.8.5.3.2 The choice of $gg \to (H) \to \gamma\gamma$ k-factors

As the most precise computation of the $gg \to \gamma\gamma$ continuum background has been done at NLO [596], the interference term is also limited to a NLO precision. However the signal $gg \to H \to \gamma\gamma$ is known up to NNLO with threshold resummation up to NNLL [219], while the computation provided in Sherpa 2 is only done at NLO. The increase of cross-section due to higher-order effects is usually implemented, for the signal, as a multiplicative k-factor K_S that rescales the cross-section of the signal Monte-Carlo. In this particular case this factor is of $K_S = 1.45$. If the impact of higher orders on the background cross-section was known the same approach could be carried out, using a factor K_B. As these two factors correspond to the impact of additional diagrams in the signal and background amplitudes, they also have an impact on the interference term whose cross-section will then scale as $\sqrt{K_S K_B}$.

Although an exact value for K_B cannot yet be determined, it is possible to determine an interval within which it should be. The dominating contribution to the Higgs signal is carried by a loop of top-quarks while for the continuum $gg \to \gamma\gamma$ background it comes from a loop of light quarks. At NLO, it was noticed in [596] that this implied larger short-distance renormalization effects for the signal calculation than for the background, which gave a LO to NLO K-factor larger by $\approx 20\%$ for the signal than for the background. Although no higher-order computations exist for the background yet, it is expected that the same analysis will hold for the NLO to NNLO K-factor, and hence a reasonable interval within which K_B should be is $[1,\ K_S]$.